UiO : University of Oslo

Mattia Mina

Cosmology at small scales: ultra-light dark matter and baryon cycles in galaxies

Thesis submitted for the degree of Philosophiae Doctor

Institute of Theoretical Astrophysics
Faculty of Mathematics and Natural Sciences

2020

Series of dissertations submitted to the
Faculty of Mathematics and Natural Sciences, University of Oslo
No. 2312

ISSN 1501-7710

Cover: Hanne Baadsgaard Utigard.
Print production: Reprosentralen, University of Oslo.

To all my beloved

Preface

This thesis is submitted in partial fulfilment of the requirements for the degree of *Philosophiae Doctor* at the University of Oslo. The research presented here was conducted at the Institute of Theoretical Astrophysics (ITA), at the University of Oslo, under the supervision of professor David F. Mota and associate professor Hans A. Winther. This thesis represents an effort to contribute to the development of the scientific knowledge related to the history of the Universe. The introductory chapters serve the purpose of placing the work I have done during the last four years in a broader context, in order to make my research better understandable and to set the academic publications accompanying this thesis in a broader perspective.

In Chapter 1, I will introduce the recent advances in the field of modern cosmology, which contributed to the development of the standard model of cosmology, the ΛCDM model. I will briefly describe the history of the Universe and I will point to the problems and the open questions within the currently accepted theory describing the evolution of the Universe. I will introduce the theory of general relativity and I will describe how tiny perturbations from a smooth, homogeneous and isotropic Universe have evolved into the cosmic web and into the wide collection of structures we can observe today in the sky.

In Chapter 2, I will focus on one of the most puzzling mysteries concerning the Universe as known today: the dark matter. I will describe in detail the cosmological and astrophysical probes used to study the effects of dark matter on the visible component of the Universe, and I will explain the evidences pointing to the existence of such an elusive form of matter. I will explain why the ΛCDM model does not provide an accurate description of the Universe at small scales, I will introduce the small-scale challenges that the standard model of cosmology is facing today, and I will discuss possible solutions within the dark sector and the baryonic physics.

In Chapter 3, I will introduce the numerical tools needed to model the structure formation process and, in general, I will describe the common techniques employed in cosmological N-body simulations. I will also explain how the baryonic physics is modelled in hydrodynamic simulations and how relevant astrophysical phenomena are implemented in sub-grid models.

In Chapter 4, I will summarise the main investigation points of my research and I will briefly discuss the opportunities that current and future experiments will provide to promote our understanding of the mysterious nature of dark matter and, in general, of the Universe.

Acknowledgements

I wish to thank many people who have a special meaning for me. First, I want to thank my supervisors David F. Mota and Hans A. Winther, who taught me how to freely develop my scientific thoughts. They encouraged me at every step of my Ph.D. and they left me the freedom to work in a way I really enjoyed. Together, we worked on highly engaging and stimulating projects. I also want to thank Sijing Shen, not only as a collaborator in one of my Ph.D. projects, but also as a friend and as an example of seriousness and dedication. Furthermore I would like to thank other scientists and friends I have met in Norway. I am sorry if I am forgetting someone, but here is the list in no particular order: Robert H., Robert W., Marie, Max and Rahel, Lluis and Nina, Clara, Ainar and Marianne, Ranajoy, Bridget, Ata, Monica, and Harald. With many of them I have shared interesting ideas and stimulating conversations about physics, astrophysics and cosmology, and with all of them I have shared my wonderful experience in Oslo.

I wish to thank my all long-time friends and the *ciuk pist* companions, sharing their life and happiness with me. In particular, I wish to thank Carlo, Paolo and Maurizio, who have been my best fiends since I was a child.

I wish to thank my parents who, with many sacrifices, have given me the opportunity to study and to embark on this wonderful journey of personal growth, and my whole family who, for better or worse, have always supported me. They have always encouraged me to dream big and look ahead, they have taught me healthy values and moral principles, and they have been true inspiration during my entire life.

Last but not least, a special thank to my beloved Viviana, who has always supported and even endured me, every day of my life since I met her. She has helped me fully understand that the Universe is such a wonderful place!

Mattia Mina
Oslo, October 2020

List of Papers

Paper I

Mattia Mina, David F. Mota and Hans A. Winther. "SCALAR: an AMR code to simulate axion-like dark matter models". Submitted for publication in *Astronomy & Astrophysics*. arXiv: 1906.12160.

Paper II

Mattia Mina, David F. Mota and Hans A. Winther. "Solitons in the dark: non-linear structure formation with fuzzy dark matter". Submitted for publication in *Astronomy & Astrophysics*. arXiv: 2007.04119.

Paper III

Mattia Mina, Sijing Shen and Benjamin W. Keller. "The baryon cycle of the Seven Dwarfs with superbubble feedback". Submitted for publication in *Astronomy & Astrophysics*.

Contents

List of Figures

List of Tables

Chapter 1

Introduction

Throughout this thesis, I work in natural units, where, $c = \hbar = k_{\rm B} = 1$. In addition, I use a "mostly positive" metric signature $(-,+,+,+)$.

1.1 Introduction

Astronomy is, in its broadest sense, the study of any object and physical phenomena originating outside the Earth. From the motion of small celestial bodies, such as comets, planets and stars, to the formation of bigger objects far away from our own planet, such as galaxies and cluster of galaxies, from exotic objects, like black holes and neutron stars, to gravitational waves: these are only some of the research topics included in modern astronomy. Nowadays, astronomy is mostly associated to observations, driving the theoretical understanding in two related research fields: cosmology and astrophysics. Cosmology studies the origin and the evolution of the Universe as a whole, from the Big Bang to the present day, together with the formation and the dynamics of large-scale structures we can observe today in the sky. Astrophysics, instead, aims to develop the theoretical understanding of the formation of medium and small structures. It applies the laws of physics to describe the birth, life and eventually death of planets, stars, black holes and galaxies.

Astronomy is perhaps one of the most exciting research fields. With the passion and the desire to discover and explore the unknown, astronomy has a long and glorious history, dating back to ancient societies, such as the mayans, the babylonians, the greeks, and the astronomers of the renaissance. We believe that we understand how the Universe was born and how it has evolved into what it is today, but the Universe is a mysterious place and we are only starting now to unveil its darkest secrets. As for many astronomers, the beautiful sky at night offered me motivation and inspiration for my studies.

1.2 Modern cosmology

Modern cosmology gets its theoretical foundations from the theory of general relativity (GR), published by A. Einstein (Einstein, 1917). Until the beginning of the $20^{\rm th}$ century, gravity was a force and the corresponding gravitational interaction was universally described by Newton law of gravitation, so far successful when describing the motion of planets around the Sun. With the advent of GR, gravity was no longer considered a force, but rather the result of the space-time curvature induced by the presence of a distribution of mass and energy. The dynamics of space-time is described by Einstein field equations in terms of its energy and mass content, and its curvature results in what we

perceive as a gravitational force. A stable solution of the Einstein field equations was derived by Einstein, introducing a cosmological constant Λ in order to describe a static Universe. Later on, A. Friedman showed that stable solutions to the Einstein field equations also exist in the case of an expanding model of the Universe (Friedmann, 1922; Friedmann, 1924).

Modern cosmology relies on a set of empirical facts resulting from fundamental discoveries made across the 20^{th} century. The cosmological principle states that, when observed on large scales, the Universe is homogeneous and isotropic. According to the Copernican principle, which asserts that our location is not special, if we observe a nearly isotropic Universe, then the Universe must look isotropic from any location point and, thus, it is necessarily homogeneous.

In 1929, E. Hubble found that all observed galaxies are receding from the Milky Way. He showed that the radial velocity of galaxies surrounding the Milky Way is proportional to their distance from us, thus discovering that the Universe is expanding. In Hubble (1929), he formulated the Hubble law:

$$v = H_0 \times d \ , \tag{1.1}$$

relating the recessional velocity v of a galaxy and its distance d from the Milky Way to the Hubble constant H_0, which corresponds to the present day expansion rate of the Universe. Reversing the cosmic expansion back in time leads to a moment in the past where the Universe was in a much denser state, than it is today. Assuming the Universe had enough time, its distant past would be considered as a physical singularity, later called Big Bang. The time needed to evolve from a singularity into a Universe with the present day expansion rate of H_0 can be estimated by inverting the Hubble law:

$$t_0 \equiv H_0^{-1} = \frac{d}{v} \sim 13.7 \text{ Gyr} \ , \tag{1.2}$$

providing in this way a first approximation of the age of the Universe.

In the 1930s, J. Oort found that the motion of stars in the Milky Way suggested the presence of a conspicuous excess of mass in the galaxy compared to previous estimates (Oort, 1932). Roughly at the same time, while studying velocity dispersions of galaxies within the COMA cluster, F. Zwicky discovered that also galaxy clusters contain more matter than it can be seen (Zwicky, 1937), and he postulated the existence of a new form of non-baryonic matter, known today as dark matter, which does not interact via electromagnetic interaction, but only by means of gravity. Later studies of galaxy rotation curves (Rubin and Ford, 1970) and velocity dispersions of galaxies within clusters (Faber and Jackson, 1976) confirmed that the missing matter cannot be of baryonic nature.

In the 1940s and 1950s, many astronomers speculated that the hot and dense primordial plasma should be observable in the form of a smooth background radiation with a black-body spectrum. The cosmic microwave background (CMB) was discovered by accident in 1965, when the radio astronomers A. Penzias and R. Wilson found a mysterious and persistent background noise in their signal, while testing new antennas (Penzias and Wilson, 1965). This was the first major

discovery that had been theoretically predicted in advance, and it provided further evidence in favour of the Big Bang model.

The Cosmic Background Explorer (COBE) satellite (Bennett et al., 1996; Mather et al., 1990; Smoot et al., 1992) revealed the presence of tiny anisotropies in the CMB, a direct signature of primordial fluctuations that grew into the structures we observe today in the Universe. In particular, Bennett et al. (1996) established the existence of a nearly scale-invariant spectrum of primordial fluctuations. With the results of the Wilkinson Microwave Anisotropy Probe (WMAP) satellite (Bennett et al., 2003; Hinshaw et al., 2009; Jarosik et al., 2007; Jarosik et al., 2011), previous findings have been confirmed and constrained to greater accuracy.

In 1997, studies of supernovae (SNe) revealed that the Universe is not only expanding, but expanding at an accelerated rate (Perlmutter et al., 1999; Riess et al., 1998). Since gravity is attractive, it would be natural to expect that the expansion is slowing down, rather than accelerating. Therefore, a new form of unknown energy was included in the description of the Universe and, today, it is called dark energy (Copeland, Sami, and Tsujikawa, 2006).

The era of precision cosmology officially started with the last major CMB experiment in 2009, when the Planck satellite was launched. Results from the Planck mission constrained current cosmological models to an unpercentage accuracy (Planck Collaboration et al., 2014; Planck Collaboration et al., 2016; Planck Collaboration et al., 2018).

In 2016, the gravitational waves predicted by GR were observed for the first time (Abbott et al., 2016a; Abbott et al., 2016b), providing new ways to test the fundamental knowledge about the Universe.

Nowadays, the ΛCDM model is the currently accepted model to describe the physics governing the evolution of the Universe. It is a phenomenological model and, as a consequence, the history of the Universe is described by a series of events which have, in the majority of cases, direct observational consequences. In its minimal form, the ΛCDM model parametrises the evolution of the Universe in terms of six independent parameters only: physical baryon and dark matter densities, the age of the Universe, scalar spectral index, curvature fluctuation amplitude and reionisation optical depth (Tab. 1.1).

1.3 History of the Universe

The ΛCDM model works by extrapolating the current state of the Universe back in time, tuned with observations. By reversing the current expansion history, we can infer that the Universe was in a hot and dense state earlier in time, where matter and radiation were tightly interacting, and matter was in the form of a primordial plasma. However, this approach is limited by the poor number of early times probes and by the current understanding of fundamental physics: as we travel further back in time, we reach large energies that cannot be probed by particle accelerators and where the laws of physics break down. The earliest

Description	Symbol	Value
Physical baryon density	$\Omega_{\rm b}h^2$	0.02230 ± 0.00014
Physical dark matter density	$\Omega_{\rm dm}h^2$	0.1188 ± 0.0010
Age of the Universe	t_0	$(13.799 \pm 0.021) \times 10^9$ years
Scalar spectral index	$n_{\rm s}$	0.9667 ± 0.0040
Curvature fluctuation amplitude	$\Delta^2_{\rm R}$	$2.441^{+0.088}_{-0.092} \times 10^{-9}$
Reionisation optical depth	τ	0.066 ± 0.012

Table 1.1: List of the six independent parameters parametrising the ΛCDM model (Planck Collaboration et al., 2016).

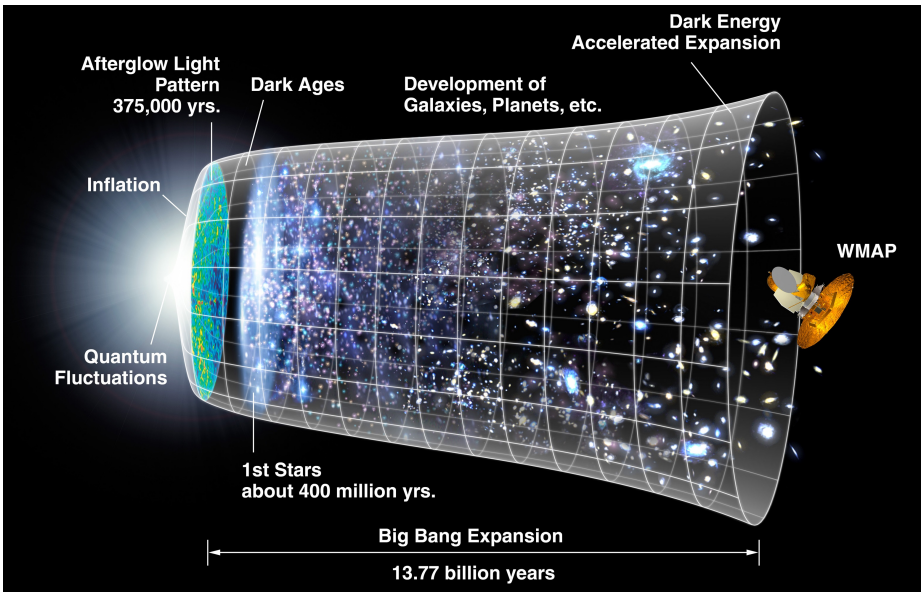

Figure 1.1: Timeline of the history of the Universe, from the Big Bang to the present. Credit: NASA/WMAP Science Team (Timeline of the Universe).

moment in time we can extrapolate is called Big Bang and it represents the starting point of a journey in the cosmological history of the Universe.

Early Universe From our understanding of fundamental physics, it is possible to assume that initially the Universe was in a state called quark-gluon plasma. When the Universe reaches temperatures of ~ 200 MeV, the quark-gluon plasma transition takes place: quark and gluons become confined in baryons and mesons,

marking the starting point when the evolution of the Universe is understood in great detail. At this point, the primordial plasma consists of many particle species held in thermal equilibrium. Once the interaction rate of a given particle species exceeds the expansion rate of the Universe, the corresponding species decouples from the primordial plasma, a process known as "freeze out", evolving on its own from this moment on. When the Universe is ~ 1 second old, its temperature reaches a value of ~ 0.5 MeV and only electrons, protons and neutrons are left in the primordial plasma, while all other species have already decoupled.

Nucleosynthesis Between 3 and 5 minutes after the Big Bang, the Universe reaches a temperature of ~ 0.05 MeV and nuclear reactions become unbalanced, leading to the formation of the first nuclei. At this point, protons and neutrons bind together, forming the first nuclei of hydrogen and helium at the beginning, and heavier nuclei later on.

Matter-radiation equality Initially, the Universe is in its radiation dominated epoch, when the expansion of the Universe is dominated by all the species which are in a relativistic regime, such as photons and neutrinos. At roughy $\sim 60,000$ years after the Big Bang, the energy density of matter and radiation contribute in the same way to the expansion and, at this point, the Universe enters the matter dominated epoch.

Recombination Roughly $380,000$ years after the Universe was born, electrons and protons bind together, forming neutral atoms. The Universe becomes transparent and the remaining photons are now free to travel across the space-time almost without any interaction. This process is also known as photon decoupling, corresponding to the moment when the CMB radiation is released.

Structure formation The Universe enters the phase of structure formation. Tiny fluctuations in the density field grow until the present day, collapsing under the effect of gravity and forming the structures we can observe today in the sky.

The different phases of the Universe are not completely separated, but blend together in a complex way, forming what we call today the standard model of cosmology, or ΛCDM model.

1.4 Open questions

Even if it seems we know a lot about the Universe, in reality we know very little. What we can directly observe today consists of baryonic matter and photons, which are only a tiny fraction of the entire matter-energy budget of the Universe. In fact, from the last parameter estimation provided by the Planck mission, ordinary matter makes only $\sim 5\%$ of the entire matter-energy budget of the

Universe, while $\sim 25\%$ is in a mysterious form of matter known as dark matter and $\sim 70\%$ is in an even more mysterious form of energy known as dark energy.

The fine-tuning problem The cosmological constant was introduced to explain the late-time accelerated expansion of the Universe, as an attempt to model the dark energy contribution to the Universe. The cosmological constant Λ has a very specific value, measured by the Planck mission as $\Lambda = 1.1056 \times 10^{-52}$ m^{-2}. The presence of such a constant is not forbidden in Einstein field equations, but there is no fundamental reason for such a low value. Initially, the cosmological constant was attributed to the vacuum energy. In particle physics, the expected vacuum energy depends upon the chosen energy scale cutoff, but in any case it would be orders of magnitude off the measured value of the cosmological constant. Without a fine-tuning of the known laws of physics, there exists nowadays no good explanation for the value of the cosmological constant.

Initial conditions The question of how tiny deviations from homogeneity have originated relies on what happened prior to the Big Bang. One of the common suggestions is that the Universe went through an inflationary phase, quickly expanding by a factor of at least 10^{25}, and resulting in almost perfectly smooth Universe with small perturbations generated by a magnification of quantum fluctuations of a hypothetical inflaton field, responsible for the inflationary phase.

The matter and anti-matter asymmetry Apparently, there is no fundamental reason why the Universe, at the present day, contains mostly matter rather than anti-matter. The standard model of particle physics allows creation of particles and anti-particles pairs from vacuum fluctuations. A primordial asymmetry between the matter and anti-matter field needs to be invoked in order to evolve into the present day observed asymmetry. However, no known physical mechanism can lead to such a difference, and the matter and anti-matter asymmetry still has to be explained.

The Hubble tension After the Hubble constant was inferred by the CMB radiation measurements, it was also inferred by mapping velocities of objects with known distances from the Earth, such as Type Ia SNe. Even if this technique is limited by the low redshift of these objects, the inferred Hubble constant is significantly higher than the value inferred by the best fit to CMB data. This difference can be due to systematic errors when measuring either the CMB or the SNe, but if the tension is confirmed later on, this will strongly point in the direction of new physics.

The dark sector The origin of dark matter and dark energy is still one of the most puzzling mysteries related to the Universe. On one hand, it is an established fact that the standard model of particle physics is incomplete, and the nature of dark matter and dark energy could be discovered by extending the known fundamental physics. Nowadays, a lot of effort is spent in looking for

new physics in experiments with particle accelerators, trying to produce and/or detect dark matter particles. In particular, several hypothetical dark matter candidates have been suggested over the past few decades, each leaving its own signature on the observed Universe. On the other hand, on cosmological scales, gravity could behave in a different way than expected. The GR theory is well tested only at some spatial scales and several alternative theories of gravity have been proposed to explain dark matter and/or dark energy contributions to the evolution of the Universe. Nowadays, many models describing a wide range of observations are available, however the true nature of these dark components remains unknown, and one of the important roles of astronomical observations is to constrain alternative dark matter models and theories of gravity.

1.5 General Relativity

In general, the dynamics of a system can be mathematically described in terms of an action. Two physical states of the same system are connected by the path which minimises the action. By means of the principle of least action the governing equations, describing the behaviour of the system, can be derived. In GR, the whole Universe can be described by the Einstein–Hilbert action:

$$S_{\rm EH} = \int d^4x\sqrt{-g}\left[\frac{1}{16\pi G}(R-2\Lambda)+\mathcal{L}_M\right] , \tag{1.3}$$

which includes all the matter fields within $\mathcal{L}_M$ and the cosmological constant Λ. The variation of the action with respect to the metric tensor $g_{\mu\nu}$ leads to the Einstein field equations:

$$R_{\mu\nu} - \frac{1}{2}g_{\mu\nu}\mathcal{R} + \Lambda g_{\mu\nu} = 8\pi G T_{\mu\nu} . \tag{1.4}$$

The Ricci tensor $R_{\mu\nu}$ provides a measure of the curvature of a Riemann manifold. It is defined by the contraction of two indices of the Riemann tensor, which reads:

$$R^{\mu}{}_{\nu\rho\sigma} = \frac{\partial\Gamma^{\mu}_{\nu\sigma}}{\partial x^{\rho}} - \frac{\partial\Gamma^{\mu}_{\nu\rho}}{\partial x^{\sigma}} + \Gamma^{\mu}_{\eta\rho}\Gamma^{\eta}_{\nu\sigma} - \Gamma^{\mu}_{\eta\sigma}\Gamma^{\eta}_{\nu\rho} . \tag{1.5}$$

The Christoffel symbols $\Gamma^{\mu}_{\alpha\beta}$ are defined as:

$$\Gamma^{\mu}_{\alpha\beta} = \frac{1}{2}g^{\mu\rho}\left(\frac{\partial g_{\beta\rho}}{\partial x^{\alpha}} + \frac{\partial g_{\alpha\rho}}{\partial x^{\beta}} - \frac{\partial g_{\alpha\beta}}{\partial x^{\rho}}\right) , \tag{1.6}$$

and they determine the free fall motion of bodies through the geodesic equation:

$$\frac{d^2x^{\mu}}{d\tau^2} + \Gamma^{\mu}_{\alpha\beta}\frac{dx^{\alpha}}{d\tau}\frac{dx^{\beta}}{d\tau} = 0 . \tag{1.7}$$

The infinitesimal interval of proper time is given by:

$$d\tau^2 = -g_{\mu\nu}dx^{\mu}dx^{\nu} . \tag{1.8}$$

Finally, the Ricci tensor is given by:

$$R_{\mu\nu} = R^{\alpha}{}_{\mu\alpha\nu} \ . \tag{1.9}$$

The Ricci scalar, instead, is defined as the contraction of the two indices of the Ricci tensor:

$$\mathcal{R} = R^{\mu}{}_{\mu} \ . \tag{1.10}$$

On the right hand side of Eq. (1.4), $T_{\mu\nu}$ is the stress-energy tensor and it describes the flux of matter and energy through space-time, generalising the stress-energy tensor of Newtonian mechanics. For a perfect fluid in the comoving coordinate system, the stress-energy tensor is given by:

$$T_{\mu\nu} = (\rho + p)u^{\mu}u^{\nu} - pg^{\mu\nu} \ , \tag{1.11}$$

where the density ρ_i and the pressure p_i of a generic fluid component are linked by the equation of state $p_i = w_i\rho_i$, and $u^{\mu} = dx^{\mu}/d\tau$ is the four-velocity of the fluid.

The Einstein field equations, Eq. (1.4), are a set of ten independent, coupled and non-linear equations for the metric tensor $g_{\mu\nu}$, describing how the space-time curves depending upon its matter and energy content.

1.6 Background evolution

The ΛCDM model is based on the fundamental assumption that, when observed on large scales, the Universe appears homogeneous and isotropic. This leads to another fundamental assumption: there is a particular frame in which the matter and energy content of the Universe can be approximated, on large scales, by a perfect fluid. In this comoving reference frame, the geometry of the Universe can be described by the Friedmann–Robertson–Walker (FRW) metric tensor, characterised by the following line element expressed in polar coordinates:

$$ds^2 = -dt^2 + a^2\left[\frac{dr^2}{1-kr^2} + r^2\left(d\theta^2 + \sin^2\theta d\phi^2\right)\right] \ . \tag{1.12}$$

The Hubble rate of expansion is related to the scale factor a by means of $H = d\ln a/da$:

$$H = \frac{d\ln a}{dt} \ . \tag{1.13}$$

The term k in Eq. (1.12) accounts for the curvature of the Universe:

$$k = \begin{cases} -1, & \text{open Universe} \\ 0, & \text{flat Universe} \\ +1, & \text{close Universe} \end{cases} \tag{1.14}$$

Thus, neglecting tiny fluctuations in the primordial plasma, the Einstein field equations can be simplified in a system of two equations, known as the Friedmann equations, describing the expansion history of the Universe. The Friedmann equations can be analytically solved to compute the expansion rate, as well as the relative abundances of different constituents of the Universe. In a spatially flat Universe ($k = 0$), the Friedmann equations are given by:

$$H^2 = \frac{8\pi G}{3}\rho \ , \tag{1.15}$$

$$\frac{1}{a}\frac{d^2a}{dt^2} = -\frac{4\pi G}{3}\left(\rho + 3p\right) \ . \tag{1.16}$$

The matter and energy content of the Universe is expressed in terms of:

- photons and any relativistic particle species, described by an equation of state with $w_r = 1/3$;
- non-relativistic matter, including baryons and dark matter, with $w_m = 0$;
- cosmological constant, with $w_\Lambda = -1$.

Different contributions to the matter and energy content of the Universe dominate the expansion of the Universe at different times. Their energy density can also be normalised by the critical density of the Universe and expressed, for a generic component, as:

$$\Omega_i = \frac{\rho_i}{\rho_c} \ , \tag{1.17}$$

where ρ_c is defined as:

$$\rho_c = \frac{3H^2}{8\pi G} \ . \tag{1.18}$$

1.7 The perturbed Universe

Prior to the structure formation phase, the Universe was almost perfectly homogeneous, with the exceptions of tiny deviations from the mean cosmic density. During the structure formation phase, these small density fluctuations evolved until they formed the vast amount of structures we can observe today: an intricate network of filaments, sheets and voids, called cosmic web.

In principle, the evolution of density perturbations is fully described by the perturbed Einstein equations. However, in order to gain an insight on how density perturbations evolve, it is possible to focus on matter fluctuations only, on scales well within the horizon, and in epochs where the Universe is in its matter dominated phase. In this case, the Newtonian approximation is well justified, and the evolution of tiny perturbations in a perfect fluid can be described by means of a set of hydrodynamic equations.

Small density perturbations reflect in tiny deviations from the FRW metric, used to describe the background cosmology and the expansion history of the Universe. Thus, in order to account for tiny inhomogeneities, the metric tensor can be written as:

$$g_{\mu\nu} = \bar{g}_{\mu\nu} + \delta g_{\mu\nu} \ , \tag{1.19}$$

where $\bar{g}_{\mu\nu}$ denotes the background metric tensor. In the Newtonian gauge, the perturbed FRW metric is described by the line element:

$$ds^2 = -\left(1 + 2\Psi\right) dt^2 + a^2 \left(1 - 2\Phi\right) dx^i dx^i \ , \tag{1.20}$$

where, in the absence of anisotropic stress, Φ and Ψ are the same and they represent the Newtonian gravitational potential. The system of hydrodynamic equations for an ideal, non-relativistic and self-gravitating fluid, in a comoving reference frame, is given by:

$$\frac{\partial \rho}{\partial t} + 3H\rho + a^{-1}\nabla \cdot (\rho \mathbf{v}) = 0 \ , \tag{1.21}$$

$$\frac{\partial \mathbf{v}}{\partial t} + H\mathbf{v} + a^{-1} \left(\mathbf{v} \cdot \nabla\right) \mathbf{v} = -a^{-1} \left(\nabla\Phi + \frac{\nabla p}{\rho}\right) \ . \tag{1.22}$$

Perturbations in the density field are often quantified in terms of density contrast:

$$\delta = \frac{\rho - \bar{\rho}}{\bar{\rho}} \ , \tag{1.23}$$

where $\bar{\rho}$ denotes the background density. In addition, only small perturbations of density, pressure, and velocity around their mean values are considered:

$$\rho = \bar{\rho} + \delta\rho \ , \tag{1.24}$$

$$p = \bar{p} + \delta p \ , \tag{1.25}$$

$$\mathbf{v} = \bar{\mathbf{v}} + \delta\mathbf{v} \ . \tag{1.26}$$

First, the background value of velocity perturbations corresponds to the Hubble flow, while the perturbation $\delta v = u$ corresponds to the peculiar velocity. Second, perturbations in pressure are related to those in density by $\delta p = c_{\rm s}^2 \delta\rho$, where $c_{\rm s}$ denotes the sound speed. Taking these considerations into account, the above system of equations can be linearised and expressed as:

$$\frac{\partial \delta}{\partial t} + a^{-1}\nabla \cdot \mathbf{u} = 0 \ , \tag{1.27}$$

$$\frac{\partial \mathbf{u}}{\partial t} + H\mathbf{u} = a^{-1} \left(\nabla\Phi + c_{\rm s}^2 \nabla\delta\right) \ . \tag{1.28}$$

These equations are in comoving units and they can be combined with the Poisson equation:

$$\nabla^2\Phi = 4\pi G\bar{\rho}a^2\delta \ , \tag{1.29}$$

into a single second-order differential equation, known as the Jeans equation, describing the gravitational collapse of density perturbations. When in the linear regime, different Fourier modes in the perturbed density field decouple, and the linear equations can be analytically solved. Thus, expanding the density field in Fourier modes:

$$\delta(\mathbf{x}, t) = \sum_k \delta_k(t) e^{-i\mathbf{k}\cdot\mathbf{x}} \ , \tag{1.30}$$

the Jeans equation in Fourier space is given by:

$$\frac{\partial^2 \delta_k}{\partial t^2} + 2H\frac{\partial \delta_k}{\partial t} + \left[\frac{c_\mathrm{s}^2 k^2}{a^2} - 4\pi G\bar{\rho}\right]\delta_k = 0 \ . \tag{1.31}$$

The Jeans wavenumber is defined as:

$$k_J = \left(\frac{4\pi G a^2 \bar{\rho}}{c_\mathrm{s}^2}\right)^{1/2} \ . \tag{1.32}$$

Only perturbations below the Jeans scale, corresponding to $\lambda_J = 2\pi/k_J$, can effectively grow, while for perturbations above the Jeans scale Eq. (1.31) describes a stationary wave which, in turn, does not grow. Considering the special case of a density perturbation collapsing during the matter dominated epoch, Eq. (1.31) has two solutions: a growing mode evolving as $\delta_k \propto a$, and a decaying mode evolving as $\delta_k \propto a^{-2/3}$. The Jeans equation describes perturbations of a generic fluid. In the specific case of dark matter density perturbations, the sound speed is zero, and all perturbations within the horizon grow into denser and denser structures.

1.8 Non-linear regime

The linear theory provides a good approximation as long as perturbations are small compared with the corresponding background values. For example, modes entering the horizon at matter-radiation equality have a density contrast of $\delta \sim 10^{-5}$, and the linear theory accurately describes the first stages of the collapse. However, as the Universe evolves, density fluctuations grow in time and, when $\delta \lesssim 1$, the linear theory is no longer a good approximation, as modes enter in the non-linear regime, coupling with each other. The non-linear evolution of the density field is extremely complex and it cannot be studied analytically. Thus, large numerical simulations are needed in order to describe the intricate cosmic web, with dark matter sheets and filaments, together with galaxies, stars and black holes. Numerical cosmology has become today a compelling field of research within astronomy, as it provides the only means to fully describe the process of structure formation and evolution in the non-linear regime.

Chapter 2

Dark Matter, baryons and the Universe at small-scales

2.1 Introduction

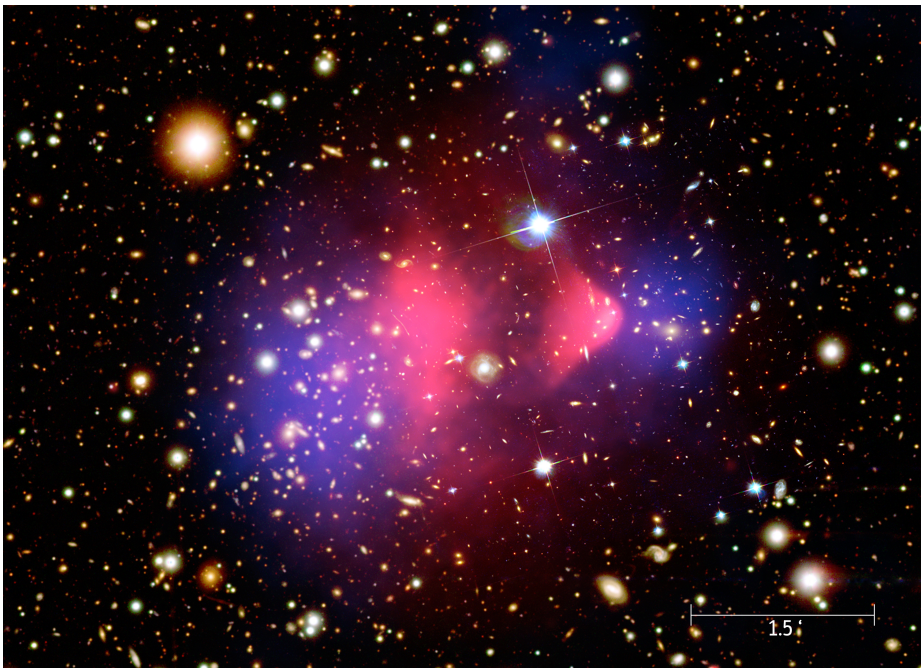

Figure 2.1: Composite image of the bullet cluster, in which the dark matter and the gas components have been wrenched apart due to the collision of two large clusters of galaxies. The pink overlay represents the X-ray emission recorded by the Chandra Telescope of the two colliding clusters, while the blue overlay represents the mass distribution of the clusters calculated by using gravitational lensing techniques. Credit: NASA, CXC, and M. Weiss (Chandra X-ray Observatory).

The nature of dark matter represents one of the most exciting open questions in physics. At the present day, one of the most convincing arguments in favour of dark matter comes from direct measurement of galactic rotation curves (Rubin, Ford, and Thonnard, 1978; Rubin, Ford, and Thonnard, 1980; Rubin et al., 1985). In Newtonian dynamics, for spherically symmetric objects, the circular

velocity v_c is given by:

$$v_c(r) = \sqrt{\frac{GM_{enc}(r)}{r}} \ , \tag{2.1}$$

where M_{enc} is the total mass enclosed within a radial distance r from the center. Therefore, as observed for planets in the Solar System, the circular velocity should drop as $v_c \propto 1/\sqrt{r}$ at large radii. However, the observed rotation curves typically exhibit a nearly constant trend at large distances, implying the existence of an invisible halo with $M_{enc} \propto r$, or equivalently an outer density profile dropping as $\rho \propto r^{-2}$.

Furthermore, the mass of galaxy clusters can also be estimated with X-ray observations of the intracluster medium (ICM), corresponding to their dominant baryonic component. The ICM consists of a hot gaseous halo with temperatures of $T \sim 10^7 - 10^8$ K, which emits X-ray radiation by thermal bremsstrahlung and line emission. From the temperature distribution of the ICM, it is possible to measure the gravitational potential of the galaxy cluster and, thus, to infer its total mass. Since the earliest X-ray observations (Forman et al., 1972; Gursky et al., 1972; Kellogg et al., 1973), it has been concluded that galaxy clusters do not have enough gas to account for their total mass. Recent measurements of the distribution of dark matter in galaxy clusters, coming from the Chandra X-Ray Observatory, strongly suggest that clusters are primarily held together by the gravitational potential of dark matter (Vikhlinin et al., 2006).

Another strong evidence in favour of dark matter comes from gravitational lensing observations, where the light passing near a galaxy cluster is bent by the presence of a mass distribution, as predicted by GR. The light is bent depending on the mass of the cluster, and this offers an alternative method to estimate the mass of the galaxy cluster (Tyson, Valdes, and Wenk, 1990), without relying on observations of its dynamics. Later on, gravitational lensing observations were also used as an alternative way to study dark matter density profiles and mass fractions (Koopmans and Treu, 2003).

At the same time, cosmological observations of CMB anisotropies, combined with measurements of the local Hubble rate calibrated with Cepheid variables (Riess et al., 2009), measurements of light curves of Type Ia SNe (Kessler et al., 2009) and measurements of Baryonic Acoustic Oscillations from large-scale galaxy surveys (Percival et al., 2010), can be used to constraint the present day dark matter density of the Universe.

Even if the rich evidence provided by astronomical observations strongly supports the existence of dark matter, its nature is still unknown. Many extensions of the standard model of particle physics predict the existence of new particles which can naturally be potential dark matter candidates. Sterile neutrinos, supersymmetric neutralinos and gravitinos, axions, and Kaluza-Klein excitations in theories with extra dimensions are only some of the commonly studied dark matter candidates (see e.g. Bergström, 2009; Bertone, Hooper, and Silk, 2005; Steffen, 2009).

From the theoretical point of view, there are several criteria related to the fundamental properties of a viable potential dark matter candidate, that must be

fulfilled in order to account for this mysterious form of matter (Taoso, Bertone, and Masiero, 2008). First, new physical theories concerning the origin of dark matter should become relevant at higher energy scales than those probed today by particle colliders. These energy scales may have been accessed in early moments of the evolution of the Universe. Dark matter particles could have been produced then by thermal production, or as a non-thermal relic, but either way it must have been produced in similar quantities to the observed dark matter abundance. A potential dark matter candidate must be effectively dark. Electromagnetic interactions with photons must be weaker than those of any other charged particle. In addition, dark matter must not couple with neutral baryonic matter. Strong constraints on such interaction strengths are obtained by requiring that dark matter does not couple with photons or baryons during the recombination epoch, otherwise the CMB acoustic peaks would be washed away. A significant coupling with baryons would allow dark matter to radiate away its energy, thus affecting the structure formation process. Furthermore, dark matter particles must be of non-baryonic nature. This is required by Big Bang nucleosynthesis (BBN) predictions, which are extremely sensitive to the baryon-to-photon ratio. Moreover, when it has decoupled from the primordial plasma and the Universe has entered its matter dominated epoch, dark matter gravitationally collapses into small-scale structures. For this reason, dark matter particles are required to have small and non-relativistic velocities, already at the time of decoupling. Otherwise, the dark matter temperature would be too high, and small-scale perturbations would be washed away because of the high dark matter free-streaming length. These considerations depend upon the dark matter phenomenology driving the decoupling process, and the mass of dark matter particles. Finally, dark matter particles must be stable over cosmological time scales.

Many extensions of the standard model of particle physics predict the existence of new weakly interactive massive particles (WIMPs), coupled with the weak gauge boson. Nowadays, WIMPs are still one of the most likely dark matter candidates, as they naturally satisfy most of cosmological and astrophysical requirements, and they offer the possibility of being detected in particle experiments. WIMPs are often assumed to be thermally produced in the early Universe, with typical weak-scale masses of the order of $m_{\mathrm{WIMP}} \sim 100$ Gev. Such particles were held in thermal and chemical equilibrium with the primordial plasma by annihilation processes to standard model particles and antiparticles. Considering the generic species χ as a WIMP candidate, with a generic mass m_χ, the species is in equilibrium in the early Universe, at temperatures $T \gg m_\chi$. Assuming that also standard model particles are, at that time, in equilibrium with the primordial plasma, the evolution of the WIMP number density n_χ follows the Boltzmann equation:

$$\frac{dn_\chi}{dt} + 3Hn_\chi = -\langle\sigma v\rangle \left[n_\chi^2 - \bar{n}_\chi^2\right] \ , \tag{2.2}$$

where $\bar{n}_\chi$ is the WIMP equilibrium number density, and $\langle\sigma v\rangle$ corresponds to its thermally averaged annihilation cross section. At sufficiently high

temperatures, the interaction rate $\Gamma_\chi = n_\chi \langle \sigma v \rangle$ exceeds the Hubble rate and WIMP annihilation processes are totally balanced by the WIMP creation inverse processes. Thus, WIMP particles are held in equilibrium with the primordial plasma and, as the right-hand side of Eq. (2.2) is effectively zero, n_χ closely tracks the equilibrium solution. While the Universe is expanding, the WIMP number density drops as the temperature decreases, and the interaction rate Γ_χ falls below the Hubble rate. Annihilation and creation processes of WIMP particles are no longer able to maintain chemical equilibrium, and the WIMP species decouples.The freeze-out temperature is approximately determined by the condition $\Gamma_\chi \sim H$, and as long as the species decouples at temperatures $T < m_\chi$, the hypothetical WIMP candidate freezes-out when already non-relativistic. Thus, at the decoupling temperature $T_{\rm dec}$, the number density n_χ is Boltzmann suppressed:

$$n_\chi(T_{\rm dec}) \sim (m_\chi T_{\rm dec})^{3/2}\, e^{-m_\chi/T_{\rm dec}} \ , \tag{2.3}$$

and the WIMP velocity $v \sim (T_{\rm dec}/m_\chi)^{1/2}$ is small. Assuming that the WIMP freeze-out takes place in the radiation dominated epoch, the further evolution of the number density of the species χ simply follows the expansion of the Universe, and the corresponding WIMP relic density can be estimated as:

$$\Omega_\chi h^2 \sim 0.1 \left(\frac{3 \times 10^{-26}\ {\rm cm}^3/{\rm s}}{\langle \sigma v \rangle} \right) \ . \tag{2.4}$$

A simple order of magnitude estimate shows that a weak-scale annihilation cross section naturally provides a WIMP relic abundance that reproduces the observed dark matter one. This striking coincidence is often referred to as the "WIMP miracle", and it explains the reason why WIMPs have gained a lot of popularity as dark matter candidates.

2.2 Cosmological small-scale probes

Nowadays, the ΛCDM model is constantly under revision, as technological development promotes more and more sophisticated astronomical observations. In general, numerical simulations are very powerful tools. Due to the non-linear nature of gravity, structure formation and evolution can be fully studied only by means of cosmological and hydrodynamic simulations. The results of numerical simulations give access to a vast amount of information that can be translated into observables, and directly compared with astronomical data.

Power spectrum Within the context of cosmological structure formation, the most important statistics is the two-point correlation function of the density field, which provides general information about how matter clusters at different scales, and it is defined as:

$$\xi\left(\mathbf{x}, \mathbf{x}'\right) = \left\langle \delta\left(\mathbf{x}\right) \delta\left(\mathbf{x}'\right) \right\rangle \ , \tag{2.5}$$

where $\langle \ldots \rangle$ denotes the ensemble average or expectation value. Under the assumption of homogeneity and isotropy, the two-point correlation function can be expressed as an average over all directions, without losing any information. In this case, the two-point correlation function can only depend on $r = |\mathbf{x} - \mathbf{x}'|$ and $\xi(r) \equiv \xi(\mathbf{x}, \mathbf{x}')$. Then, given a matter clump in a random location of the Universe, the two-point correlation function describes the probability of finding another clump at a given distance. In Fourier space, the two-point correlation function can be expressed as:

$$\langle \delta(\mathbf{k}) \, \delta^*(\mathbf{k}') \rangle = (2\pi)^3 \, \delta_D(\mathbf{k} - \mathbf{k}') \, P(k) \ , \tag{2.6}$$

where $\delta_D(\mathbf{x})$ denotes the 3D Dirac delta function and $P(k)$ denotes the matter power spectrum. Thus, the matter power spectrum $P(k)$ corresponds to the Fourier transform of the two-point correlation function:

$$P(k) = \int d^3 \ x\xi(\mathbf{x}) e^{-i\mathbf{k}\cdot\mathbf{x}} \ , \tag{2.7}$$

or in its dimensionless form:

$$\Delta^2(k) = \frac{k^3 P(k)}{2\pi^2} \ . \tag{2.8}$$

Above galactic scales, the predicted ΛCDM matter power spectrum is well constrained by cosmological observations. Up to galactic scales, any alternative dark matter model must predict a power spectrum within the given constraints, while deviations are allowed below galactic scales.

Structural properties Since the end of inflation, small initial over-densities in the primordial plasma have grown forming stars, galaxies, and cluster of galaxies we can observe today in the sky. To define what a structure is, cosmologists often use the virial theorem, which relates the total kinetic energy of a self-gravitating object to its gravitational potential energy:

$$E_{\rm pot} + 2E_{\rm kin} = 0 \ . \tag{2.9}$$

When the gravitational potential energy $E_{\rm pot}$ balances the total kinetic energy $E_{\rm kin}$ according to Eq. (2.9), the collapsed structure has reached a quasi-equilibrium configuration and it is said to be in virial equilibrium.

The virial theorem is often used to link observable properties of galaxies to other fundamental, but non observable properties. For example, the mean velocity of stars can be directly measured, as well as the half-light radius, which provides a crude estimate of the size of a galaxy. Thus, the mass of a galaxy can be approximated as:

$$M_{\rm gal} = \frac{\langle v^2 \rangle \, R_{\rm gal}}{G} \ , \tag{2.10}$$

where $\langle v^2 \rangle$ is the mean velocity of its stellar component, considering both rotation and velocity dispersion, $R_{\rm gal}$ is the effective radius, corresponding to the size of the galaxy, and G is the Newton gravitational constant.

For dark matter halos, though, the virial mass is often defined as the spherical region where the mean density is approximately $\Delta_{\rm vir} \sim 200$ times the critical density of the Universe at a given redshift. Thus, the virial mass $M_{\rm vir}$ of a dark matter halo can be computed according to:

$$M_{\rm vir} = \frac{4\pi R_{\rm vir}^3}{3} \Delta_{\rm vir} \rho_c \ , \tag{2.11}$$

where the critical density of the Universe is given by $\rho_c = 3H^2/(8\pi G)$. It is common practice to define the virial velocity as the circular velocity of the halo at the virial radius:

$$V_{\rm vir}^2 = \frac{GM_{\rm vir}}{R_{\rm vir}} \ . \tag{2.12}$$

Thus, it is possible to relate the evolution of virial mass and radius of a given dark matter halo in terms of its virial velocity:

$$M_{\rm vir} = \frac{V_{\rm vir}^3}{HG\sqrt{\Delta_{\rm vir}}} \ , \tag{2.13}$$

$$R_{\rm vir} = \frac{V_{\rm vir}}{H\sqrt{\Delta_{\rm vir}}} \ . \tag{2.14}$$

These two expressions are at the foundation of the hierarchical model of structure formation: small dark matter halos form first, and eventually merge later into bigger halos, whereas late-forming dark matter halos are larger and more massive. In general, the structures observed today in the Universe span a wide range of masses and dimensions: from the largest observed structures like galaxy clusters with $M_{\rm vir} \sim 10^{15}\ M_\odot$, to galaxies similar to the Milky Way with $M_{\rm vir} \sim 10^{12}\ M_\odot$, to the smallest dwarf galaxies found in the local volume with $M_{\rm vir} \sim 10^{9}\ M_\odot$.

Since the advent of the first cosmological simulations, the collapse of cold dark matter (CDM) halos has been intensively studied. As numerical techniques and computational capabilities have significantly improved over the last decades, theoretical studies of structure formation have provided a series of robust predictions for the ΛCDM model. The existence of a large number of low-mass halos and the presence of a universal dark matter density profile are among the most important ones, and they are at the origin of the small-scale challenges the standard model of cosmology is currently facing.

Dark matter only cosmological simulations show that the internal structure of CDM halos follows a nearly universal density profile, characterised by cuspy r^{-1} inner profile, transitioning to a steep r^{-3} outer profile. Thus, each dark matter density profile can be characterised by the Navarro–Frenk–White (NFW) functional form:

$$\rho_{\rm NFW}(r) = \rho_0 \left[\frac{r}{R_{\rm s}} \left(1 + \frac{r}{R_{\rm s}} \right)^2 \right]^{-1} \ , \tag{2.15}$$

where ρ_0 corresponds to the central density of the dark halo. The characteristic scale R_s, instead, describes the cross-over between the r^{-1} behaviour at small radii and the r^{-3} behaviour at larger radii, and it is related to the virial radius by the concentration parameter $c_\mathrm{NFW} = R_\mathrm{vir}/R_\mathrm{s}$ In the hierarchical picture of structure formation, low-mass structures collapsed when the average density of the Universe was higher than at the present day, and therefore have higher concentrations than more massive halos formed later.

Rotation curves As early observations of stellar kinematics in galaxies provided the first evidence of dark matter, rotation curves are a powerful probe of the dynamics of dark matter on small scales. In the ΛCDM model, the structure of the halo is universally described by the NFW profile. Thus, from Eq. (2.1), it is possible to compute the circular velocity profile of a given halo assuming a density profile described by Eq. (2.15). The corresponding rotation curves exhibit a peak in circular velocity at radial distances which depends upon the virial radius of the halo and its concentration:

$$R_\mathrm{max} = \frac{\alpha}{c_\mathrm{NFW}} R_\mathrm{vir} \ , \tag{2.16}$$

with $\alpha \sim 2.16$. In addition, for CDM halos the ratio between the maximum circular velocity V_max and the virial velocity decreases as the concentration increases, and increases as the virial mass of the halo decreases.

Halo mass function In theoretical studies of structure formation, the clustering of dark matter is often quantified by counting the number of dark matter halos that form in cosmological simulations. The number density of dark matter halos falling in a given mass range, at a given redshift, is encoded in the so-called halo mass function (HMF). Empirically, for the case of the ΛCDM model, the HMF is:

$$\frac{dn(M,z)}{dM} \propto M^\alpha \ , \tag{2.17}$$

where $\alpha \sim -1.9$ for masses below $M_\mathrm{vir} < 10^{10}$. Thus, in terms of abundance of dark matter structures, the ΛCDM model predicts the formation of a large number of low-mass halos, which are observed to form in numerical simulations, even within other virialised structures. The minimum predicted halo mass strongly depends on the underlying physics of the dark matter model considered as CDM candidate. For example, assuming the standard WIMP paradigm, the suppression mass scale is set by first collisional damping at kinetic decoupling, and then by free-streaming (e.g. Bertschinger, 2006; Hofmann, Schwarz, and Stöcker, 2001). In case of typical WIMP candidates with masses around ~ 100 GeV, the growth of cosmological perturbation is erased below $M \sim 10^{-6}\ M_\odot$, corresponding to the Earth mass (Green, Hofmann, and Schwarz, 2004). For this reason, in dark matter only cosmological simulations, CDM is found to clump at all resolved mass scales.

2.3 Small-scale challenges of CDM

Numerical simulations of structure formation have shown how the large-scale structure of the Universe is quite well captured by the ΛCDM model. However, when performing pure dark matter simulations, the evolution of structure on galactic scales is in tension with current astronomical observations. As a consequence, a series of discrepancies have emerged between the ΛCDM model and the observed Universe, thus challenging our understanding of the small-scale cosmology.

The core-cusp discrepancy In ΛCDM simulations (Dubinski and Carlberg, 1991; Navarro, Frenk, and White, 1996), dark halos follow a $\rho \propto r^{-\gamma}$, with a typical log-slope of $\gamma \sim 0.8$–1.4 in the innermost region. The dynamics of low surface brightness (LSB) galaxies and late-forming dwarf galaxies is expected to be heavily dominated by their host dark matter halo, thus providing a good laboratory to study dark halo structures in detail. Indeed, by measuring rotation curves, it is possible to infer the dark matter mass distribution within the halo with great accuracy. Many independent measurements of rotation curves suggested a preferred isothermal profile, characterised by a nearly flat core in the center, with typical log-slope of $\gamma \sim 0$–0.5. Measurements of dwarf galaxies in the local volume from the THINGS (Walter et al., 2008) and the LITTLE THINGS (Hunter et al., 2012) galaxy surveys found similar results, where the inner log-slope was $\gamma = 0.29 \pm 0.07$, rather than the typical $\gamma = -1$ of ΛCDM halos.

Often the baryonic content of the Universe is not included in cosmological simulations and the core-cusp problem can have its origin in the dark matter only character of early numerical simulations. However, the properties of galaxies are strongly affected by baryonic physics and modern hydrodynamic simulations include the baryonic content of the Universe in the form of gas, together with a variety of astrophysical processes relevant in the structure formation context. Several independent studies have shown how baryonic feedback can significantly alter the properties of dark matter halos, generating feedback-induced cores in the innermost region of dark matter density profiles (Adams et al., 2014; Agnello and Evans, 2012; Amorisco and Evans, 2011; Battaglia et al., 2008; Flores and Primack, 1994; Moore, 1994; Oh et al., 2015; Walker and Peñarrubia, 2011).

Missing satellites Numerical simulations of dark halos of similar size to the one hosting the Milky Way have shown how dark matter halos form at all resolved masses, thus producing a large number of substructures and leading to a diverging halo mass function towards the low-mass end. Furthermore, many simulated subhalos of such dark matter halos are, in principle, large enough to support molecular cooling and host a visible galaxy. At the present day, the number of observed Milky Way satellites is ~ 50, at least one or two orders of magnitude less than expected from cosmological simulations. Even if future observations are expected to discover new ultra-faint dwarf galaxies, it is unlikely

that the count will match theoretical ΛCDM predictions. The halo mass function predicted by the ΛCDM model counts one order of magnitude more subhalos than observed in the Mikly Way.

Another possibility is that low-mass dark matter halos are just extremely poor in baryon content and so they are impossible to detect. Modern hydrodynamic simulations have also shown that galaxy formation is heavily quenched in systems below $M_{\rm vir} \sim 10^9\ M_\odot$, where photoionizing heating induced by the cosmic ultraviolet (UV) background suppresses accretion of gas, thus solving the mismatch in the count of visible satellites of halos similar to the one of the Milky Way (Garrison-Kimmel et al., 2014; Griffen et al., 2016; Kuhlen, Madau, and Silk, 2009; Springel et al., 2008; Stadel et al., 2009).

Too-big-to-fail While attempting to solve the missing satellite problem by introducing a mass threshold below which halos are just dark, matching the biggest simulated halos with the most massive Milky Way satellites causes another problem (Boylan-Kolchin, Bullock, and Kaplinghat, 2011; Boylan-Kolchin, Bullock, and Kaplinghat, 2012). In this way, the biggest simulated halos are simply too massive to host observed satellite galaxies, while the ones that could potentially host observed satellite galaxies are not the most massive ones. On the other hand, if simulated subhalos are matched by observed galaxies, bigger simulated halos are too big to have failed at forming stars.

Such a discrepancy was originally introduced for Milky Way satellites, but also the Andromeda galaxy was subsequently found to suffer from the too big to fail problem, together with field galaxies in the Local Group. In general, the observed galaxies in the low redshift Universe, with stellar mass in the range $10^5 < M_* < 10^8\ M_\odot$, have inferred central masses that are roughly half of what expected from ΛCDM simulations.

Scaling relations Even if we can observe today a wide diversity of galaxies, a series of scaling relations tightly connect the dynamical and baryonic properties of galaxies, even in dark matter dominated systems. These scaling relations hold for many different types of galaxies and one of the most famous scaling relations is the baryonic Tully–Fisher relation (BTFR), which links the total baryonic mass $M_{\rm b}$ of a galaxy with its asymptotic circular velocity $V_{\rm asym}$ as:

$$V_{\rm asym}^4 = a_0 G M_{\rm b}\ , \tag{2.18}$$

where a_0 is the critical acceleration, measured by astronomical observations. Eq. (2.18), is an extension of the well known Tully–Fisher relation, where $V_{\rm asym}$ is related to the luminosity, which in turn traces the total stellar mass of a galaxy. However, cosmological simulations of the ΛCDM model are not able to reproduce the observed BTFR, but they predict a $V_{\rm asym}^3 \propto M_{\rm b}$ scaling instead. When modelling baryonic physics in hydrodynamic simulations, several studies have been able to qualitatively reproduce the BTFR, but the scatter is still larger than expected.

In addition, the search for dark matter in collider and laboratory experiments have been so far unsuccessful. Thus, alternative dark matter models have been specifically developed in order to solve, or at least alleviate, the small-scale crisis the ΛCDM is currently facing. As baryonic physics has been suggested as a tentative solution to small-scale problems, the need of cosmologically motivated alternative dark matter models is still under debate. However, the data on the satellites of the Milky Way can pose strong constraints on new dark matter candidates, in particular those predicting a small-scale cutoff in the primordial power spectrum. If the predicted cutoff is too sharp, then the number of low-mass halos forming would be too small to account for the observed number of Milky Way satellites.

2.4 Ultra-light Dark Matter

Ultra-light dark matter (ULDM) denotes a class of models where dark matter is composed of ultra-light bosons, forming a Bose-Einstein condensate (BEC) on astronomically relevant scales. Models of ULDM were introduced as an alternative to the classical CDM paradigm to address the small-scale challenges affecting the ΛCDM model. The general idea is that ULDM behaves in a very similar way to CDM on large scales, recovering the remarkable success of the standard model of cosmology when describing the large-scale properties of the observed Universe, while on galactic scales ULDM forms a BEC manifesting the quantum nature of particles, affecting the properties of dark matter structures.

Today, ultra-light axions (Abbott and Sikivie, 1983; Dine and Fischler, 1983; Preskill, Wise, and Wilczek, 1983), fuzzy dark matter (Hu, Barkana, and Gruzinov, 2000) and superfluid dark matter (Berezhiani and Khoury, 2015) are just few examples of the wide variety of models encompassed by the ULDM class of models (see e.g. Ferreira, 2020; Hui et al., 2017; Marsh, 2016, for detailed reviews).

2.4.1 Condensation

In the 1920s, S. N. Bose and A. Einstein introduced the idea of the Bose–Einstein condensation, a phenomenon that occurs in particular physical conditions. A Bose–Einstein condensate (BEC) is defined as a system where a large fraction of bosons occupies the minimum energy state, or ground state, and it is typically achieved at extremely low temperatures. When the Bose–Einstein condensation occurs, the high occupation number of the ground state leads to a macroscopic manifestation of quantum mechanics, where the system of particles collectively behaves as a macroscopic fluid. The collection of bosons forming a BEC follows the Bose–Einstein statistics:

$$\bar{n}_i = g_i \left(e^{(\epsilon_i - \mu)/T} - 1 \right) \ , \tag{2.19}$$

which provides the occupancy number $\bar{n}_i$ of a given energy state ϵ_i depending on the degeneracy of the energy level g_i, the chemical potential μ and the

temperature T of the fluid. The critical temperature, expressed as:

$$T_{\mathrm{c}} = \left(\frac{2\pi}{m_{\mathrm{B}}}\right)\left(\frac{n}{\zeta(3/2)}\right) , \tag{2.20}$$

defines the temperature below which most of the particles occupy the lowest energy state and, as a consequence, condensation occurs. In Eq. (2.20), n represents the number density of particles, m_{B} denotes the mass of the boson, and $\zeta(3/2) \sim 2.612$ is the Riemann zeta function. The Bose–Einstein condensation is a consequence of the wave-like nature of particles at low temperatures, where the de Broglie wavelength of multiple bosons overlaps, as it exceeds the mean inter-particle separation. The de Broglie wavelength associated to a massive particle is defined as:

$$\lambda_{\mathrm{dB}} = \frac{1}{m_{\mathrm{B}} v} , \tag{2.21}$$

and it determines the coherence length of the fluid.

2.4.2 Field description

Several different theoretical models have been introduced to describe systems of many identical bosons, where a large fraction occupies the minimum energy state. Often it is useful to associate the Bose-Einstein condensation with the phenomenon of spontaneous breaking of a continuous symmetry, rather than with a phase transition occurring when a large occupation number of the ground level is achieved. In general, the system of bosons is described by a many-particle wave-function. The free choice of the global phase of the many-particle wave-function leads to a global $U(1)$ symmetry, which is responsible for the conservation of the total number of particles in the system.

When describing this type of systems, where the phenomenon of spontaneous symmetry breaking is present, the field theory description provides an extremely useful tool, where the many-body wave-function is effectively represented by a classical field. In this case, spontaneous symmetry breaking occurs when a stable state of the system, i.e. the condensate, is not symmetric under a global $U(1)$ symmetry transformation. The Goldstone theorem establishes the existence of spin-zero massless particles emerging when the global $U(1)$ symmetry is spontaneously broken. These particles are called Goldstone bosons and they eventually acquire a small mass in the presence of non-perturbative physical effects. Ultra-light dark matter models consider a generic Goldstone boson as a potential dark matter candidate. In this case, a hypothetical $U(1)$ symmetry is spontaneously broken relatively early in the history of the Universe, and the emerging ultra-light scalar boson accounts for the cosmic dark matter budget.

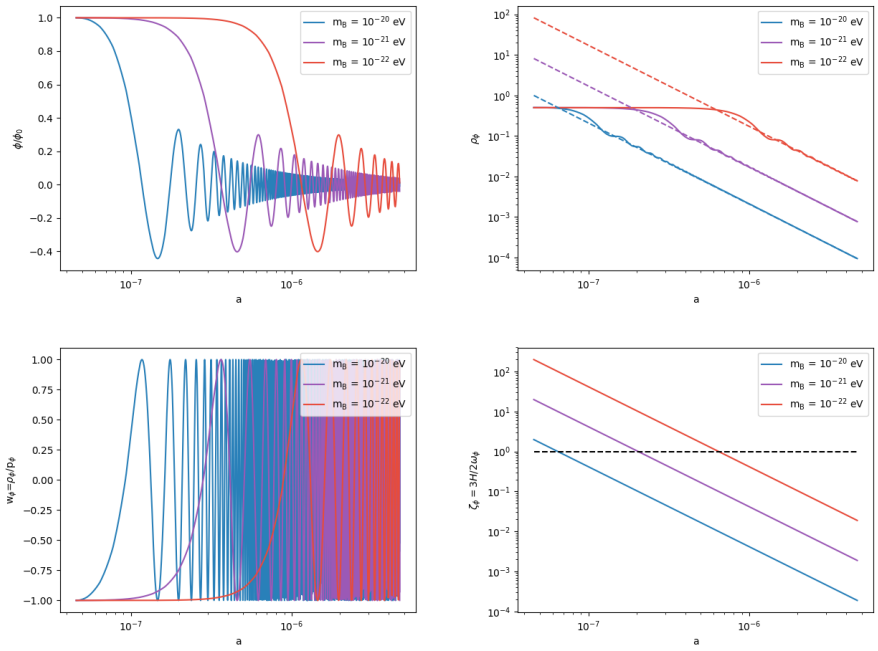

Figure 2.2: Toy model for the background evolution of a light scalar field in a cosmological context. The values reported for different physical quantities have no connection with a physically motivated ULDM model. The different panels represent the evolution as a function of the scale factor of the field normalised to its initial value, its energy density and its equation of state, and the damping ratio.

2.4.3 A scalar field in cosmology

In General Relativity, the action of a minimally coupled real scalar field is given by:

$$S_\phi = \int \mathrm{d}^4\mathrm{x}\sqrt{-\mathrm{g}}\left[-\frac{1}{2}\mathrm{g}^{\mu\nu}\partial_\mu\phi\partial_\nu\phi - \mathrm{V}(\phi)\right] \ , \tag{2.22}$$

valid only once symmetry is broken and non-perturbative physics becomes relevant. The equation of motion of the scalar field can be obtained by varying the action with respect to the scalar field and, for the case of ULDM, it is in the form of a Klein–Gordon equation:

$$\frac{1}{\sqrt{-g}}\partial_\mu\left[\sqrt{-g}\ g^{\mu\nu}\partial_\nu\right]\phi - \frac{\partial V}{\partial\phi} = 0 \ . \tag{2.23}$$

The energy-momentum tensor, instead, can be obtained by varying the action with respect to the metric tensor:

$$T^{\mu}_{\ \nu} = g^{\mu\alpha}\partial_{\alpha}\phi\partial_{\nu}\phi - \frac{\delta^{\mu}_{\ \nu}}{2}\left[g^{\alpha\beta}\partial_{\alpha}\phi\partial_{\beta}\phi + 2V(\phi)\right] \ . \tag{2.24}$$

By expanding the potential in Taylor series and considering only the leading term, i.e. the mass term, the dynamics of the field can be studied in a model independent way. Assuming a homogeneous and isotropic Universe, it is possible to study the background evolution of the field. In particular, by considering the non-zero element of the FRW metric tensor, the equation of motion reduces to:

$$\frac{d^2\phi}{dt^2} + 3H\frac{d\phi}{dt} + m_{\rm B}^2\phi = 0 \ , \tag{2.25}$$

which corresponds to a harmonic oscillator with a time dependent friction term provided by the Hubble rate. The natural frequency ω_ϕ of the system corresponds to the mass of the scalar field, and its damping ratio is given by:

$$\zeta = \frac{3H}{2\omega_\phi} \ . \tag{2.26}$$

The background evolution of the dark matter density field is characterised by two distinct regimes. Initially, the Hubble friction dominates over the mass term and, as $\zeta \gg 1$, the system is described by an over-dumped harmonic oscillator where the field does not evolve. As a consequence, the equation of state is characterised by $w_\phi = -1$ and the field behaves as a dark energy contribution. The condition $\zeta = 1$ marks a cross-over between the over-dumped and the under-dumped regime. As the ϕ starts to displace from its initial value, the field oscillates with a natural frequency ω_0 and the density evolves as a^{-3}, following the behaviour of any non-relativistic component. When the Universe is radiation or matter dominated, the scale factor evolves as $a \propto t^p$ and the exact solution of the equation of motion, Eq. (2.25), is given by:

$$\phi = a^{-3/2}(t/t_i)^{1/2}\left[C_1 J_n(m_{\rm B}t) + C_2 Y_n(m_{\rm B}t)\right] \ , \tag{2.27}$$

where $n = (3p-1)/2$, t_i corresponds to the initial time, and J_n and Y_n are Bessel functions of first and second kind, respectively. As long as the oscillation phase starts prior to the matter-radiation equality, the scalar field can be effectively used to describe the dark matter component of the Universe.

2.4.4 Linear theory

Small density perturbations in the dark matter fluid grow until they form the structure we can observe in the sky today. The linear perturbation theory provides a good approximation when describing the evolution of small over-densities in the dark matter fluid, but typical galaxies correspond to present day over-densities of $\delta \gtrsim \mathcal{O}(10^5)$. Except in extreme conditions, the gravitational

potential is very small and it is possible to consider the Newtonian limit. In addition, the focus is on the formation and evolution of structures and, as the de Broglie wavelength of the scalar field is much smaller than the particle horizon at matter-radiation equality, the non-relativistic limit is fully justified. Rapid temporal oscillations of the scalar field do not contribute significantly to the evolution of the gravitational potential while the field collapses. Thus, it is possible to consider the Wentzel–Kramers–Brillouin (WKB) approximation in the form:

$$\phi = \left(m_{\rm B}\sqrt{2}\right)^{-1} \left(\psi e^{-im_{\rm B}t} + \psi^* e^{im_{\rm B}t}\right) \ . \tag{2.28}$$

By expressing ϕ in terms of a complex scalar field, high oscillation frequencies of the order of the natural frequency $\omega_0 = m_{\rm B}$ are explicitly filtered out. Thus, the equation of motion of the field reduces to:

$$i\left(\frac{\partial\psi}{\partial t} + \frac{3}{2}H\psi\right) + \left(\frac{1}{2m_{\rm B}^2 a^2}\nabla^2 + m_{\rm B}\Phi\right)\psi = 0 \ , \tag{2.29}$$

which corresponds to a non-linear Schrödinger equation, generalised for the case of an expanding Universe. The expression of the complex scalar field ψ in polar coordinates:

$$\psi = \sqrt{\frac{\rho}{m_{\rm B}}}e^{i\theta} \ , \tag{2.30}$$

gives the opportunity of describing the dynamics of the field in terms of macroscopic quantities:

$$\rho = m_{\rm B}\left|\psi\right|^2 \ , \tag{2.31}$$

$$\mathbf{v} = \frac{1}{m_{\rm B}}\nabla\theta \ . \tag{2.32}$$

The non-linear Schrödinger equation can be recast into a system of hydrodynamics-like equations, known as the Madelung formulation of quantum mechanics:

$$\frac{\partial\rho}{\partial t} + 3H\rho + a^{-1}\nabla\cdot(\rho\mathbf{v}) = 0 \ , \tag{2.33}$$

$$\frac{\partial\mathbf{v}}{\partial t} + H\mathbf{v} + a^{-1}\left(\mathbf{v}\cdot\nabla\right)\mathbf{v} = \frac{1}{am_{\rm B}}\nabla\left(\Phi + Q\right) \ . \tag{2.34}$$

While the first equation takes the same form of the classical continuity equation, the second equation recalls the CDM momentum equation, with the addition of a potential term Q, known as the quantum potential:

$$Q = -\frac{1}{2m_{\rm B}a^2}\frac{\nabla^2\sqrt{\rho}}{\sqrt{\rho}} \ . \tag{2.35}$$

The corresponding quantum pressure ∇Q is a direct manifestation of the quantum nature of the scalar field and it reflects a certain stiffness exerted by the scalar field, resisting compression during gravitational collapse.

The Madelung equations are the starting point for the linear theory. In the presence of small perturbations, Eq. (2.33) and Eq. (2.34) can be linearised and, neglecting higher order contributions, they can be expressed in terms of the over-density δ as:

$$\frac{\partial \delta}{\partial t} + 3H\rho + a^{-1}\nabla \cdot (\rho \mathbf{v}) = 0 \ , \tag{2.36}$$

$$\frac{\partial \mathbf{v}}{\partial t} + H\mathbf{v} + a^{-1}\left(\mathbf{v} \cdot \nabla\right)\mathbf{v} = \frac{1}{a m_{\mathrm{B}}} \nabla \left(\Phi + Q\right) \ . \tag{2.37}$$

These two equations can be combined into the Jeans equation, describing the evolution of a single mode perturbation in Fourier space:

$$\frac{d^2 \delta_k}{dt^2} + 2H\frac{d\delta_k}{dt} + \left[\frac{k^4}{4m_{\mathrm{B}}^2 a^4} - 4\pi G\bar{\rho}\right]\delta_k = 0 \ . \tag{2.38}$$

As in the case of CDM, the solution of Jeans equation includes a growing mode evolving as $\delta_k \propto a$, and a decaying mode evolving as $\delta_k \propto a^{-3/2}$. The presence of an effective speed of sound, however, limits the growth of perturbations to the modes below the corresponding Jeans wavenumber. Above the Jeans wavenumber, the ULDM evolution differs from the CDM one, as the quantum pressure prevents the collapse of modes with $k > k_{\mathrm{J}}$. Eq. (1.32) also applies in this case, but the effective sound speed is now given by:

$$c_{\mathrm{s}}^2 = \frac{k^2}{4m_{\mathrm{B}}^2 a^2} \ , \tag{2.39}$$

for modes well within the horizon. Thus, the Jeans scale evolves in time as well, as indicated by the dependence of the sound speed on the scale factor. Specifically, when considering the matter dominated solution of the Friedmann equations, Eq. (2.38) has the following solution:

$$\delta_k = C_1 D_+(k,a) + C_2 D_-(k,a) \ . \tag{2.40}$$

The growing and the decaying modes are respectively given by:

$$D_+(k,a) = \frac{3\sqrt{a}}{\tilde{k}^2}\sin\left(\frac{\tilde{k}^2}{\sqrt{a}}\right) + \left[\frac{3a}{\tilde{k}^4} - 1\right]\cos\left(\frac{\tilde{k}^2}{\sqrt{a}}\right) \ , \tag{2.41}$$

$$D_-(k,a) = \left[\frac{3a}{\tilde{k}^4} - 1\right]\sin\left(\frac{\tilde{k}^2}{\sqrt{a}}\right) - \frac{3\sqrt{a}}{\tilde{k}^2}\cos\left(\frac{\tilde{k}^2}{\sqrt{a}}\right) \ . \tag{2.42}$$

where $\tilde{k} = k/\sqrt{m_{\mathrm{B}} H_0}$.

2.5 Baryonic effects on dark matter

At early times, when still in the linear regime, the gravitational impact of baryons in the dark matter distribution produces the Baryonic Acoustic Oscillations observed in the matter power spectrum. In the non-linear regime, instead, baryons can affect the clustering of dark matter by means of a complex interplay between gravity and many physical processes.

Condensation of baryons into halos: adiabatic gas cooling and mergers
In the classical picture of galaxy formation, perturbations in the baryonic density field grow following the collapse of dark matter into halos. While dark matter collapses forming a virialised structure, the associated gas flows towards the central region of the halo, where galaxies are expected to form. Contrary to the dark matter case, as gas collapses under the effect of gravity, it produces accretion shocks, which heat up the gas to the virial temperature of the halo:

$$T_{\rm vir} \sim 4 \times 10^4 \left(\frac{\mu}{1.12}\right) \left(\frac{M_{\rm vir}}{10^8\ h^{-1}{\rm M}_\odot}\right)^{2/3} \left(\frac{1+z}{10}\right)\ {\rm K}\ , \qquad (2.43)$$

where μ is the mean molecular weight of the gas and $M_{\rm vir}$ corresponds to the virial mass. Before condensing in the very central region of the dark halo and forming stars, the gas needs to cool. If radiative cooling is highly inefficient, the gas forms a hot quasi-hydrostatic halo, which gradually cools and condenses towards the center of the dark halo, in the so-called "hot mode" of accretion. On the other hand, if the cooling time is shorter than the free-fall time, the gas radiatively cools and it accretes directly in the center of the dark halo, in the so-called "cold mode" of accretion.

In general, depending on its temperature, density and metallicity, gas can cool via different mechanisms, such as Bremsstrahlung (free-free emission, $T_{\rm vir} > 10^6$ K), metal-line cooling ($T_{\rm vir} \sim 10^5 - 10^6$ K), atomic cooling (H and He, $T_{\rm vir} \sim 10^4 - 10^5$ K), fine-structure lines ($C_{\rm II}$ and $O_{\rm I}$), molecular, and dust cooling ($T_{\rm vir} \sim\lesssim 10^4$ K). At the same time, heating processes compete in Compton heating, photoionization and photoelectric heating (from black hole accretion, stellar sources, and the metagalactic ionizing background), cosmic ray heating, and shocks (e.g., SN ejecta, outflows, accretion shocks). Typically, in halos with masses below $M_{\rm vir} \sim 10^8$ M$_\odot$, corresponding to virial temperatures of $T_{\rm vir} \sim 10^4$ K, the atomic cooling limit makes cooling quite inefficient. At higher masses, above $M_{\rm vir} \sim 10^{13}$ M$_\odot$, cooling is also suppressed due to the fact that the cooling time exceeds the free-fall time, thus limiting the condensation of gas in the central region of the dark halo. Furthermore, additional gas input can be due to merging processes between galaxies. Nevertheless, the assembly of the central galaxy enhances the gravitational potential in the innermost region of the halo. The dark matter distribution dynamically responds to the new gas configuration, contracting further and increasing its concentration, resulting in a steep cuspy profile in the central region.

Energy injection into halos: UV background photoheating During recombination, electrons and nucleons bind together forming neutral hydrogen. However, the first generation of stars produces a strong UV background radiation, which in turn reionises the gas and heats it up. Thus, photoionisation and photoelectric heating suppress the cooling of gas in galaxies and subsequent star formation, especially in low-mass halos. In general, heating mechanisms are extremely important, as they shift the minimum galaxy formation scale from the atomic cooling limit to present day halo masses of $M_{\rm halo} \sim 10^9$ M$_\odot$. Photoionisation and photoelectric heating are not the only heating mechanisms affecting the clustering of gas in dark halos. In general, shocks produced by SNe explosions and galactic outflows have a severe impact on the dynamical state of gas around galaxies.

The complex interplay between heating and cooling processes results in a complex multi-phase structure of the interstellar medium (ISM) and the circumgalactic medium (CGM), where cold clumps of molecular gas live in a diffuse halo composed of hot ionised gas and warm neutral gas. Together with galactic winds generated by various feedback mechanisms at high redshifts, heating processes contribute to reduce the overall present-day baryonic content found in low-mass halos.

Energy injection into halos: supernova and AGN feedback The dynamics of gas is strongly affected by a series of processes generally called feedback mechanisms. These processes are of fundamental importance, as they regulate star formation within galaxies and they are responsible for the chemical enrichment of both the ISM and the CGM, injecting heavy elements previously synthetised by stars and promoting new cooling channels such as metal-line cooling. Most of the α-elements and Fe are produced by Type II SNe, while C,N and O are primarily injected by AGB stars and their stellar winds.

During its lifetime, each individual star processes and ejects material in the form of stellar winds, injecting momentum into the surrounding medium, driving turbulences in the ISM, and promoting the formation of gas outflows. In the final stage of their evolution, massive stars explode as SNe, ejecting a mass of $M_{\rm ej} \sim 1 - 20$ M$_\odot$, with kinetic energy of 10^{51} ergs. The ejected material travels into the surrounding medium, shock-heating the ISM to temperatures of $T \gg 10^6$ K. The SN remnant is not able to cool efficiently at first, promoting the formation of an adiabatically expanding hot bubble of gas, boosting the momentum of the ejecta. The combined effect of multiple SN explosions, together with stellar winds, sweeps up a vast amount of ambient gas into hot expanding gas bubbles, known as superbubbles.

Stellar feedback affects the evolution of galaxies at all masses, but it is particularly relevant in low-mass halos, where the sudden depletion of gas in the central region of halos strongly perturbs the shallow gravitational potential wells of low-mass halos. Strong galactic outflows can heavily suppress galaxy formation in low-mass halos and they can affect both the inner structure and the abundance of low-mass galaxies.

In addition, in low-mass systems, stellar feedback can also affect the dynamics of dark matter halos. Astronomical observations have shown that dwarf galaxies have bursty star formation histories, characterised by short-lived, violent and repeated bursts of star formation. When gas collapses in the central region of a dark halo, it establishes its dominant contribution to the gravitational potential. Then, suddenly, strong galactic outflows deplete the central region from gas and energy can be transferred to the dark matter component, causing the innermost region of the dark halo to expand. As the system quickly finds a new equilibrium configuration, dark matter particles settle on new orbits at larger radii, thus lowering the central density of the dark halo. When repeated over time, this mechanism leads to large fluctuations of the gravitational potential in the proximity of the center of the dark halo, which efficiently transfers energy to dark matter, heating the central region of the dark halo and transforming the central NFW cusp into a core.

On mass scales larger than dwarf galaxies, similar feedback mechanisms from Active Galactic Nuclei (AGN) are often invoked to explain the relatively low star formation efficiencies. It is commonly thought that every galaxy hosts a supermassive black hole (SMBH) at the center, with masses above $M \gg 10^6\ M_\odot$, which can influence the dynamics of gas and the evolution of galaxies by means of their own feedback mechanisms. In quasar-mode AGN feedback, the radiation emitted by the SMBH and fast winds launched from the accretion disk can drive strong outflows. At low accretion rates, in the radio-mode, highly relativistic jets heat the surrounding gas and they contribute to the star formation quenching in more massive galaxies.

Energy injection into subhalos: tidal effects from baryonic structures
The dynamics of subhalos can be affected by tidal effects induced by the host halo. The presence of a central galaxy can enhance the tidal effects in both subhalos and satellite galaxies. Tidal forces can easily result in the total disruption of subhalos in the proximity of the central galaxy, causing a reduction in the total number of subhalos.

Other physical mechanisms can have an important influence on the evolution of galaxies. For example, magnetic fields and cosmic rays have gained a lot of attention in the field and they have started to be extensively studied along with other physical phenomena. However, to the present knowledge, they do not strongly affect the dark matter distribution, or at least they provide a negligible contribution.

Chapter 3

Numerical simulations of structure formation

3.1 Introduction

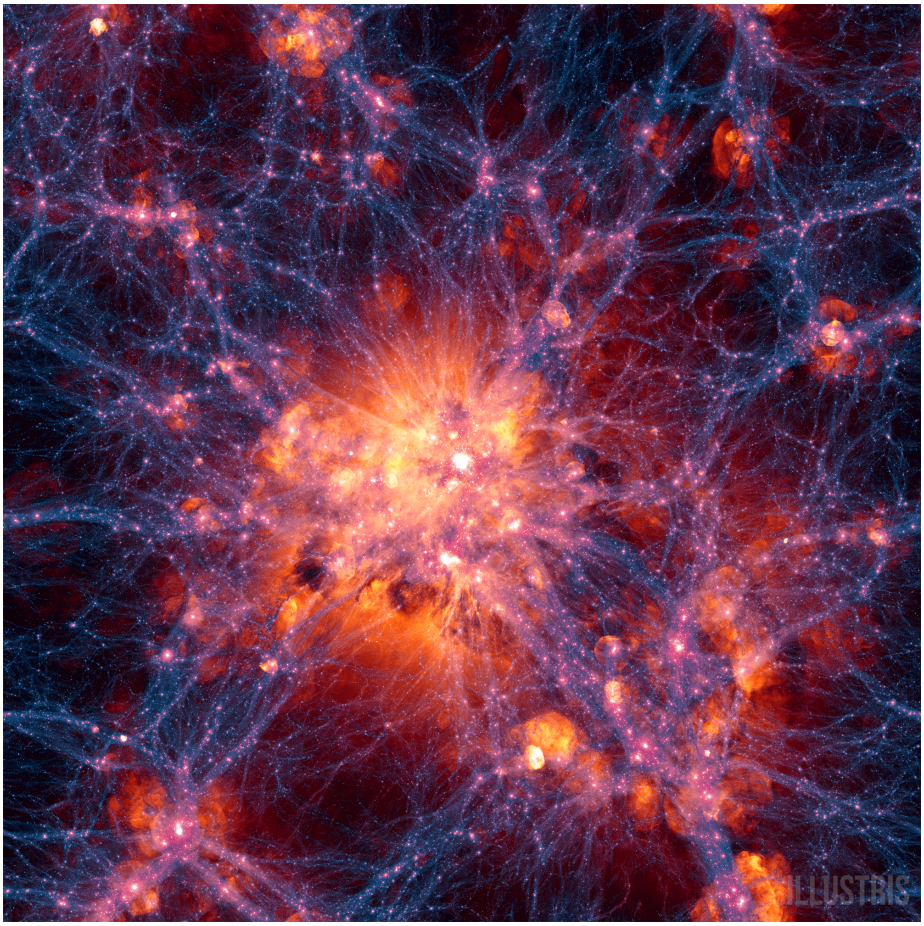

Figure 3.1: Projection of the simulation volume of the Illustris hydrodynamic simulation, showing the dark matter density overlaid with the gas velocity field of the most massive simulated galaxy cluster. Credit: Illustris collaboration (Illustris projects). Licence: Creative Commons Attribution-Share Alike 4.0 International.

Tiny density perturbations in the primordial plasma have grown today into highly over-dense structures. When modelling a ΛCDM Universe, the linear perturbation theory can successfully predict the observed CMB power spectrum and the very large-scale structures of the Universe. However, since gravity is a non-linear phenomenon, the complex dynamics of structures formed in our Universe cannot be fully described by the linear theory. Numerical simulations are required to properly model the evolution of the Universe and, thus, to make clear and trustworthy predictions over a wider range of scales.

One of the very first attempts to model a set of self-gravitating bodies dates back to 1941, when E. Holmberg was studying the dynamics of elliptical galaxies with movable light-bulbs, estimating the gravitational force by measuring the luminosity of each bulb. With the advent of computers, it has become possible to model the dynamics of larger collections of particles and thus, to simulate small portions of the Universe. By discretising time, space and mass in cosmological and hydrodynamical *N*-body simulations, the gravitational field of a given configuration of particles can be computed and used to evolve the system. Nowadays, with supercomputers, it is possible to evolve samples as large as 10^{12} particles. Initially, pure cosmological *N*-body simulations were employed to model a collection of particles only interacting by means of gravity, in order to study the large-scale distribution of dark matter particles on the Universe. Later on, gas physics was included in numerical studies, together with sub-grid models describing small-scale astrophysical phenomena, evolving into hydrodynamical simulations and providing significant insights on the relevant physical processes in galaxy formation. Over the past decades, the numerical techniques employed in simulations have significantly improved, together with computational capabilities, yielding an extraordinary progress in the ability to simulate the formation and evolution of structures in a cosmological context. In general, numerical simulations have been extensively used to study the clustering of dark matter and baryons into dark halos and galaxies, and today they represent a fundamental playground to test alternative models of dark matter.

3.2 Cosmological *N*-body simulations

In cosmological *N*-body simulations, the phase-space of a given density-velocity field is discretised by a set of particles, interacting only by means of gravity. Each particle represents a clump of millions, or even billions, of solar masses, thus reducing a dark matter halo to a collection of few particles. In order to evolve a system of particles describing the dark matter component of the Universe, first it is necessary to compute the gravitational force field for a given configuration of particles. In general, *N*-body codes can implement different strategies to compute the force field:

- Particle mesh (PM): the mass of each particle is interpolated on a fixed resolution grid by using a suitable interpolating function, such as Nearest Grid Point (NGP), Cloud-In-Cell (CIC) or Triangular Shape Cloud (TSC). Once the density field is evaluated on the grid, the gravitational potential

Φ is computed by solving the Poisson equation:

$$\nabla^2\Phi = 4\pi G a^2 \bar{\rho}\delta_{\rm m} \ , \tag{3.1}$$

where $\delta_{\rm m}$ corresponds to the matter over-density and $\bar{\rho}$ denotes the mean matter density of the Universe. The Poisson equation can be solved in Fourier space by using a spectral method, or in real space with standard numerical schemes for elliptic differential equations. Then, the force field $F_{\rm N} = -\nabla\Phi$ is interpolated back at particle positions.

- Particle-particle particle mesh (P3M): this scheme adds a correction term to account for pairs of particles with separation of the order of the grid resolution, or even smaller, improving the force resolution of PM algorithm in the case of highly clustered particles.

- Tree: a hierarchical particle tree is constructed, where each level of the tree specifies the position of the center of mass and the total mass of a region within the simulation box. Force acting on a single particle is then approximated for particles in distant regions by the center of mass estimate of the force.

Modern *N*-body codes often implement different generalisations of the aforementioned strategies.

Once the force field is computed, particles are moved along the geodesics by means of the corresponding *N*-body equation:

$$\ddot{\mathbf{x}} + 2H\dot{\mathbf{x}} = -a^{-2}\nabla\Phi \ , \tag{3.2}$$

where the Hubble rate takes into account the expansion of the Universe and it acts as a viscous force, slowing down the growth of density perturbations. In principle, this is enough to reproduce the complex dynamics of the cosmic web in cosmological *N*-body simulations. Theoretical predictions of the ΛCDM model are in good agreement with the observed statistical properties of the Universe on large scales, but stars and galaxies are made of baryonic matter and thus, it is necessary to include baryonic physics and astrophysical processes in order to model properly the process of structure formation at small scales.

3.3 Hydrodynamic simulations

In hydrodynamic simulations, the evolution of the Universe is described not only in terms of its dark matter content, but also including the baryonic content in the form of gas, thus adding a fundamental piece to the puzzle of structure formation. The gas dynamics is described by using a system of standard hydrodynamic

equations:

$$\frac{\partial \rho}{\partial t} + \nabla \cdot (\rho \mathbf{v}) = 0 \ , \tag{3.3}$$

$$\frac{\partial \mathbf{v}}{\partial t} + (\mathbf{v} \cdot \nabla)\, \mathbf{v} = -\left(\frac{\nabla P}{\rho} + \nabla \Phi \right) \ , \tag{3.4}$$

$$\frac{\partial}{\partial t}\left[\rho \left(\frac{1}{2} v^2 + \mathcal{E} \right) \right] + \nabla \cdot \left[\rho \left(\frac{1}{2} v^2 + \mathcal{E} + \frac{P}{\rho} \right) \mathbf{v} \right] - \rho \mathbf{v} \cdot \nabla \Phi = \mathcal{H} - \mathcal{C} \ , \tag{3.5}$$

which are coupled to the dark matter *N*-body equations by means of the Poisson equation.

Over the years, many different numerical algorithms have been developed in order to solve the system of hydrodynamic equations, which can be generalised into two main families.

The family called Smoothed Particle Hydrodynamics (SPH) is conceptually similar to classical *N*-body codes. In SPH algorithms, a Lagrangian fluid element carries macroscopic thermodynamic variables and it is tracked along with other fluid parcels. While in the case of collisionles dynamics particles interact only by means of gravity, in SPH codes the Lagrangian fluid element exchanges energy and momentum with nearby particles and its motion is also affected by pressure gradients. Macroscopic variables, such as mass and momentum densities, are linked to the discrete mass and velocity of each particle by using a smoothing kernel and the hydrodynamic equations are reformulated in terms of the kernel function.

The other family, instead, follows a Eulerian approach and thermodynamic variables are discretised on a fixed or adaptive grid. Thus, numerical schemes for systems of hyperbolic equations are used to solve Eqs. (3.3)–(3.5). Modern flux conserving algorithms are able to integrate the hydrodynamic equations in an accurate and efficient way, thus ensuring that no energy is numerically dissipated as the system evolves.

Over the year, a wide range of astrophysical phenomena was found to have a great impact on the formation and evolution of structures and without modelling them together with the gas physics, it is not possible to reproduce realistic galaxies. However, processes such as gas cooling and heating, star formation, and SN explosions take place on physical scales which are too small to be resolved in a cosmological context. Therefore, small-scale astrophysical processes must be incorporated within sub-grid models, which are implemented today in any code developed for hydrodynamical simulations of structure formation.

Gas cooling and heating When an over-dense region collapses under the effect of gravity, strong accretion shocks form and heat the surrounding gas, which in turn forms a hot and rarefied gaseous halo. The subsequent evolution of the gas component depends upon how efficiently the gas can cool and radiate away its thermal energy. Thus, radiative cooling and photoionization heating are implemented in the majority of modern codes used in astrophysics and cosmology. In general, cooling and heating processes are included as source terms on the

right hand side of Eq. (3.5), $\mathcal{C}$ and $\mathcal{H}$ respectively. Many cooling and heating mechanisms can be encoded in a single net cooling function, which determines the cooling efficiency depending on temperature, density and metallicity of the gas. For example, the GRACKLE chemistry and cooling library (Smith et al., 2017) has been explicitly developed for numerical simulations in cosmology and astrophysics. With GRACKLE, it is possible to solve the non-equilibrium chemistry of an extended network of primordial species, to solve the radiative cooling and to compute cooling times, taking into account different cooling channels. It also models multiple UV background sources, as well as supporting radiation transfer and arbitrary heating sources.

While it is also possible to employ tabulated cooling rates assuming collisional ionisation equilibrium, modern codes can track the metal enrichment of gas due to stellar feedback. Metal abundances are extremely important for cooling calculations, but the high uncertainties on metal yields in SNe and stellar wind models lower the predictive power of such models.

Star formation Modern hydrodynamic simulations implement roughly the same sub-grid model proposed in the pioneering work of Katz (1992). Following the Schmidt law (Schmidt, 1959):

$$\frac{d\rho_{\rm star}}{dt} = \epsilon_{\rm star} \frac{\rho_{\rm gas}}{t_{\rm ff}} \ , \tag{3.6}$$

a local star formation rate (SFR) is assigned to cold gas, depending on its density and its dynamical state. An alternative prescription was suggested by Dalla Vecchia and Schaye (2008), where the Schmidt law was recast as a function of pressure, rather than density, assuming a self-gravitating disk. Typically, the star formation efficiency $\epsilon_{\rm star}$ is calibrated to match the amplitude of the observed Kennicutt relation (Kennicutt, 1998) between the gas surface density and the star formation rate. Furthermore, stars are observed to form in regions where the ISM is in its cold and dense molecular phase. Since the ISM is observed to become $H_{\rm II}$ dominated at densities of $\sim 1 - 100$ atoms/cm^3, stars in simulations are usually allowed to form only in regions where the local gas density exceeds a given threshold.

In hydrodynamic simulations of structure formation, an entire stellar population is represented by a single star particle, with its own age, metallicity and initial mass function (IMF). Each stellar population evolves on its own and injecting energy, mass and metals into the ISM according to stellar feedback sub-grid recipes.

Stellar feedback In the first attempts to model stellar feedback in hydrodynamic simulations, a given fraction of the energy released by stars was directly deposited in the surrounding gas in the form of thermal energy. However, due to small cooling times, the energy injected into the ISM was quickly radiated away and this strategy was shown to have almost no effects, leading to an overcooling problem.

In modern hydrodynamic simulations, different approaches of sub-grid models have been proposed, ranging from kinetic feedback models where wind mass loading and velocities are predetermined (Dalla Vecchia and Schaye, 2008; Oppenheimer and Davé, 2006; Springel and Hernquist, 2003), to explicit models where radiative cooling is temporary switched off (Agertz, Teyssier, and Moore, 2011; Stinson et al., 2006; Teyssier et al., 2013), to mechanical feedback where the momentum boost during the unresolved adiabatic phase is calibrated through small-scale ISM simulations and injected into the ISM (Hopkins et al., 2014; Kimm and Cen, 2014; Smith, Sijacki, and Shen, 2018).

Among several sub-grid models, the blastwave model, recently suggested by Stinson et al. (2006), injects thermal energy into the surrounding gas and cooling is switched off for a time comparable with the lifetime of a SN-driven blastwave. Adding an "early stellar feedback" to mimic the energy input of young stellar populations, the blastwave model was shown to reproduce realistic galaxy populations. Even if very successful, the blastwave model depends on a number of free parameters which can affect the dynamics of galaxies, especially in the case of a limited resolution.

A novel approach to stellar feedback is the superbubble model, introduced by Keller et al. (2014), where thermal conduction and stochastic evaporation of cold gas are explicitly modelled, together with sub-resolution multi-phase particles to mimic the complex structure of the ISM. While the explicit separation of hot and cold phases automatically solves the overcooling problem, thermal conduction describes the mass flow from the cold shell into the hot gas, determining how much gas is heated by feedback, and the bubble temperature and mass are controlled by the evaporation process, leading to a stellar feedback prescription without addition of free parameters. In this way, the energy input provided by stellar feedback is accurately converted into thermal and kinetic energy, in the hot and cold phases respectively (Keller, Wadsley, and Couchman, 2015; Keller, Wadsley, and Couchman, 2016).

Chapter 4

Summary

Today, the ΛCDM model describes the evolution of the Universe in terms of its matter and energy content. The Universe is now believed to consist mostly of dark matter and dark energy, the true nature of which are still mysterious, and only a subdominant contribution is in the form of standard baryonic matter. From tiny initial perturbations in the density field, dark matter and baryons have collapsed by the effect of gravity, forming the vast distribution of structures we can observe today. Theoretical studies about the structure formation process strongly rely on numerical simulations, as gravity is a highly non-linear phenomenon. Over the past decades, numerical simulations have significantly improved, and today they provide a set of robust predictions for the standard model of cosmology. The observed large-scale properties of the Universe are accurately captured within the ΛCDM model, but small scales remain a great source of uncertainty. Current and future experiments, such as DES (Dark Energy Survey Collaboration et al., 2016), DESI (Levi et al., 2019), Euclid (Amendola et al., 2018), LSST (LSST Science Collaboration et al., 2009), and SKA (Maartens et al., 2015), will provide accurate measurements of the distribution of matter within the Universe and its clustering over a wide range of physical scales. Therefore, robust theoretical predictions are needed to provide an interpretation of new data and to further promote our understanding of the dark sector. This thesis represents an effort to contribute to the development of the scientific knowledge related to poorly understood aspects of our own Universe.

The aim of this work is to study the structure formation process from a small-scale perspective, analysing the origin of the small-scale tensions between current available observations and the ΛCDM model, and possible solutions with both alternative models of dark matter and baryonic physics.

During my Ph.D. studies, I first implemented the numerical algorithms required to simulate the dynamics of ULDM models in the new `SCALAR` (Simulation Code for ultrA Light Axions in `RAMSES`) code. Based on the hydrodynamic and N-body `RAMSES` code, `SCALAR` is designed to solve the non-linear Schrödinger equation coupled with an arbitrary potential, within an adaptive mesh refinement (AMR) framework. Its purpose is to simulate the non-linear gravitational clustering of new models of dark matter involving light scalar fields.

Subsequently, I employed `SCALAR` to study the phenomenology of fuzzy dark matter (FDM) in a cosmological context. The FDM model was first suggested by Hu, Barkana, and Gruzinov (2000) to solve the small-scale problems of the ΛCDM model, and it corresponds to a particular case of ULDM, where the scalar field describing the dark matter component has no self-interactions. Based on the results of the simulation, the FDM model is shown to have clear and distinct

signatures on the structure formation process, which can be directly used to test the model against observations. The capability of the FDM model to suppress the formation of structures below the dwarf mass scale is remarkable, and it can represent a simple solution to the missing satellite and the too-big-to-fail problems. However, the FDM model can potentially be in conflict with the standard hierarchical clustering paradigm if the formation mechanism of dark matter cores is exclusively attributed to the dynamics of such a light scalar field.

In order to study the impact of the baryonic component on the structure formation process, I also analysed the results of a high-resolution hydrodynamic simulation of the ΛCDM model, performed with the GASOLINE2 code, where the stellar feedback is described by the novel superbubble feedback, which includes a sub-resolution treatment of multi-phase gas particles, thermal conduction between cold and hot phases, and a model for stochastic evaporation of cold clouds. The superbubble feedback is shown to better describe the physics behind the stellar feedback process and it is capable to reproduce realistic galaxies. Furthermore, the superbubble feedback is found to promote the formation of large dark matter cores at the center of the simulated halos, potentially solving the cusp-core problem.

The work I have done during my Ph.D. studies can be improved in several ways. First, the `SCALAR` code can be further developed by implementing even more accurate schemes to solve the non-linear Schrödinger equation within an AMR framework. New refinement strategies can also be included to ensure that the resolution required to probe the innermost structure of dark halos is automatically achieved at all redshifts, without tuning the density thresholds of the currently employed refinement scheme. In terms of computational speed, `SCALAR` can be further optimised to reduce the amount of memory needed in cosmological applications. A major improvement would also be to port on GPUs the various solvers employed by `SCALAR`, in order to significantly reduce the computation time required for cosmological simulations. In addition, several numerical strategies have been recently developed to simulate the non-linear structure formation process with different ULDM models. In order to verify the robustness of the various predictions from this kind of simulations, a full benchmark study of the different existing codes should be carried out, especially because a quantitative agreement between different numerical investigations has not been achieved yet.

The natural follow up of the work I am presenting in this thesis would be to simulate the evolution of a FDM Universe including the baryonic content and the relevant small-scale astrophysical phenomena. As for the case of hydrodynamic simulations of the ΛCDM model, baryonic processes can significantly alter the predictions of dark matter only simulations. Moreover, for both numerical simulations with alternative dark matter models and hydrodynamic simulations of the ΛCDM model, larger simulations are required to study larger samples of virialised structures, covering a wider mass range, and to provide a more robust and complete set of predictions, which can be in turn tested against future observations.

In the end, a brief summary of the academic publications accompanying this

thesis is provided.

4.1 The numerics behind ultra-light dark matter models

In order to study the process of structure formation within a Universe where dark matter is in a different form than CDM, the underlying model has to be numerically implemented in modern codes for cosmological and hydrodynamical N-body simulations. The new code SCALAR was developed to solve the dynamics of a generic Bose-Einstein condensate, with the specific purpose of simulating a Universe with ULDM models.

In Paper I, we present the numerical strategy implemented in SCALAR, together with a test suite designed to show the performances of the code, in terms of accuracy and computational speed. The SCALAR code solves the governing equations within an AMR framework, in order to focus computational resources only on regions where the solution exhibits more demanding features. The solution of the non-linear Schrödinger equation is computed by means of a second-order Taylor method. In general, SCALAR can solve the governing equations with high accuracy, conserving both the energy and the mass of the scalar field. A higher level of accuracy is guaranteed when the associated continuity equation is solved on top of the non-linear Schrödinger equation. In some cases, the long term stability of the solution of the non-linear Schrödinger equation can only be achieved by including an artificial viscosity term, which numerically dumps the spurious high-frequency oscillations due to the propagation of numerical errors. Furthermore, we present a small cosmological simulation where the dark matter component is described by a light scalar field, to show that SCALAR can be employed for cosmological simulations. In this case as well, the mass and the energy of the scalar field are conserved with a high level of accuracy. By computing the matter power-spectrum, we show that the code can capture the relevant dynamics of ULDM models.

4.2 Structure formation with ultra-light dark matter

A full cosmological simulation was performed with SCALAR, in order to investigate in detail the structure formation process in a Universe where the entire cosmic dark matter budget is described by one among several ULDM models, namely the FDM model. For this purpose, the dark matter component is modelled by means of a classic scalar field, describing the collective behaviour of a large collection of bosons with a mass of $m_{\mathrm{B}} = 2.5 \times 10^{-22}$ eV.

In Paper II, we present the results of the simulation and we analyse the formation and the evolution of FDM halos. First, we track the collapse of a single halo within the simulated FDM Universe. Then we study the properties of a representative sample of dark matter structures formed within the simulation, as well as the merging process between two FDM halos. We analyse the different behaviours of CDM and FDM on small scales, by comparing the structural properties of CDM and FDM halos. We show that the structure of each FDM

halo exhibits a central solitonic core, with nearly constant density. The solitonic core is found to leave its imprint on the rotation curves of dark halos, by generating an additional velocity peak at small radii. We also find that the formation of structures is heavily suppressed below the FDM Jeans wavelength, as opposed to the case of CDM, where dark matter clumps are expected at all resolved scales. Furthermore, we characterise each FDM halo by a single scale-free invariant. The solitonic core is found to be tightly linked to its core and to the total mass of the halo by a series of scaling relations resulting from the internal symmetries of the Schrödinger-Poisson system. We also compute the core surface density of the FDM halos and we show that the simulated halos follow a completely different scaling with the core radius compared to real dark matter halos hosting observed LSB galaxies.

4.3 Superbubbles at work

Small-scale challenges of the ΛCDM model can potentially find a solution within the baryonic physics. In order to study the impact of a gas component and small-scale astrophysical phenomena, a full hydrodynamic simulation was performed with GASOLINE2, where the superbubble model was implemented to describe the stellar feedback.

In Paper III, we present the results of the simulation. The formation process of a set of isolated dwarf galaxies is studied in detail. We compare the results of the simulation with those of a similar numerical study, previously carried out with the same code, but with the blastwave feedback model instead. In addition, the properties of the simulated dwarfs are compared with current available observations and with previous numerical studies. The dwarf galaxies simulated with the superbubble model are found to follow remarkably well the empirical scaling relations derived for observed galaxies. The superbubble feedback is able to reproduce the stellar mass and cold gas content, bursty star formation histories, stellar kinematics, and the metallicities of dwarf galaxies observed in the Local Volume. The superbubble feedback is also able to drive galactic outflows, which are believed today to be highly responsible for the metal enrichment of the CGM. These large-scale outflows affect the central gravitational potential of the galaxy. Strong oscillations of the gravitational potential field can also "heat" the dark matter component, which relaxes into shallower central densities forming central dark matter cores.

4.4 Future prospects

The study of ULDM models has mainly focused on the small-scale side of structure formation, simulating the dynamics of new forms of dark matter to better understand their behaviour. Numerical simulations are an essential tool to uncover new signatures of ULDM on the structure formation process, which can be used to test the models against observations.

The abundance of dark matter structures and substructures is generally a good probe for the nature of dark matter, as different dark matter models predict significantly different amounts of subhalos, and even a minimum halo mass in the case of ULDM. Thus, the observables probing substructures represent one of the most important tests for dark matter on small scales. Future experiments such as LSST and Euclid will conduct a more comprehensive search for ultra-faint galaxies and will allow to put strong constraints on any dark matter model predicting the suppression of structures below certain scales. Another way to directly probe the formation of substructures, even if they are not luminous, is gravitational lensing. The presence of substructures alters the lensed images of quasar, changing its morphology and flux ratios. Many observations of this kind are needed to map out the distribution of dark matter halos and subhalos and to provide strong constraints on ULDM models, which generally suppress the formation of substructures of a certain mass and size. In addition, known cosmological probes, such as CMB and large-scale structure experiments, cluster abundance, and Ly-α forest, can only marginally test the small-scale suppression of dark matter structures predicted by ULDM models. The new hydrogen 21-cm line technique has the potential to probe much smaller scales than before, tracing the underlying matter and dark matter distribution.

However, predictions that are a direct consequence of the wave nature of ULDM represent a real smocking gun in favour of these models. The formation of vortices and of interference patterns are unique and distinct signatures of this class of models on galactic scales, and their detection would be a clean and direct evidence in favour of ULDM. Many ULDM models predict the formation of vortices due to the self-interactions of the field describing the dark matter component. Depending on the parameters of the model, these vortices can result in oscillations in the rotation curve of galaxies. Macroscopic interference fringes are generally expected when the BEC forming due to the small mass of ULDM is described by a coherent wave-function. Even mergers between solitonic cores can result in the formation of interference patterns. If these interference fringes could be observed, it would be another strong evidence in favour of dark matter.

The study of ULDM models is today a very active research area and much work has still to be done. However, we are entering a new exciting era, where the future will allow us a wide range of experiment to test the theoretical predictions of alternative models of dark matter, and to better probe the nature of such a mysterious form of matter.

Bibliography

Abbott, B. P. et al. (2016a). "Improved Analysis of GW150914 Using a Fully Spin-Precessing Waveform Model". In: Phys. Rev. X vol. 6, no. 4, 041014, p. 041014. arXiv: 1606.01210 [gr-qc].

Abbott, B. P. et al. (2016b). "Observation of Gravitational Waves from a Binary Black Hole Merger". In: Phys. Rev. Lett. Vol. 116, no. 6, 061102, p. 061102. arXiv: 1602.03837 [gr-qc].

Abbott, L. and Sikivie, P. (1983). "A Cosmological Bound on the Invisible Axion". In: Phys. Rev. B vol. 120. Ed. by Srednicki, M., pp. 133–136.

Adams, J. J. et al. (2014). "Dwarf galaxy dark matter density profiles inferred from stellar and gas kinematics". In: The Astrophysical Journal vol. 789, no. 1, p. 63.

Agertz, O., Teyssier, R., and Moore, B. (2011). "The formation of disc galaxies in a ΛCDM universe". In: MNRAS vol. 410, no. 2, pp. 1391–1408. arXiv: 1004.0005 [astro-ph.CO].

Agnello, A. and Evans, N. W. (2012). "A virial core in the Sculptor dwarf spheroidal galaxy". In: The Astrophysical Journal vol. 754, no. 2, p. L39.

Amendola, L. et al. (2018). "Cosmology and fundamental physics with the Euclid satellite". In: Living Reviews in Relativity vol. 21, no. 1, 2, p. 2. arXiv: 1606.00180 [astro-ph.CO].

Amorisco, N. C. and Evans, N. W. (2011). "Dark matter cores and cusps: the case of multiple stellar populations in dwarf spheroidals". In: MNRAS vol. 419, no. 1, pp. 184–196. eprint: http://oup.prod.sis.lan/mnras/article-pdf/419/1/184/18696560/mnras0419-0184.pdf.

Battaglia, G. et al. (2008). "The Kinematic Status and Mass Content of the Sculptor Dwarf Spheroidal Galaxy". In: ApJ vol. 681, no. 1, p. L13. arXiv: 0802.4220 [astro-ph].

Bennett, C. L. et al. (1996). "Four-Year COBE DMR Cosmic Microwave Background Observations: Maps and Basic Results". In: ApJ vol. 464, p. L1. arXiv: astro-ph/9601067 [astro-ph].

Bennett, C. L. et al. (2003). "First-Year Wilkinson Microwave Anisotropy Probe (WMAP) Observations: Preliminary Maps and Basic Results". In: The Astrophysical Journal Supplement Series vol. 148, no. 1, pp. 1–27.

Berezhiani, L. and Khoury, J. (2015). "Theory of dark matter superfluidity". In: Phys. Rev. D vol. 92, p. 103510. arXiv: 1507.01019 [astro-ph.CO].

Bergström, L. (2009). "Dark matter candidates". In: New Journal of Physics vol. 11, no. 10, 105006, p. 105006. arXiv: 0903.4849 [hep-ph].

Bertone, G., Hooper, D., and Silk, J. (2005). "Particle dark matter: evidence, candidates and constraints". In: Phys. Rep. Vol. 405, no. 5-6, pp. 279–390. arXiv: hep-ph/0404175 [hep-ph].

Bertschinger, E. (2006). “Effects of cold dark matter decoupling and pair annihilation on cosmological perturbations”. In: Phys. Rev. D vol. 74 (6), p. 063509.

Boylan-Kolchin, M., Bullock, J. S., and Kaplinghat, M. (2011). “Too big to fail? The puzzling darkness of massive Milky Way subhaloes”. In: MNRAS vol. 415, no. 1, pp. L40–L44. arXiv: 1103.0007 [astro-ph.CO].

Boylan-Kolchin, M., Bullock, J. S., and Kaplinghat, M. (2012). “The Milky Way’s bright satellites as an apparent failure of ΛCDM”. In: MNRAS vol. 422, no. 2, pp. 1203–1218. eprint: http://oup.prod.sis.lan/mnras/article-pdf/422/2/1203/3464467/mnras0422-1203.pdf.

Copeland, E. J., Sami, M., and Tsujikawa, S. (2006). “Dynamics of Dark Energy”. In: International Journal of Modern Physics D vol. 15, no. 11, pp. 1753–1935. arXiv: hep-th/0603057 [hep-th].

Dalla Vecchia, C. and Schaye, J. (2008). “Simulating galactic outflows with kinetic supernova feedback”. In: MNRAS vol. 387, no. 4, pp. 1431–1444. arXiv: 0801.2770 [astro-ph].

Dark Energy Survey Collaboration et al. (2016). “The Dark Energy Survey: more than dark energy - an overview”. In: MNRAS vol. 460, no. 2, pp. 1270–1299. arXiv: 1601.00329 [astro-ph.CO].

Dine, M. and Fischler, W. (1983). “The Not So Harmless Axion”. In: Phys. Rev. B vol. 120. Ed. by Srednicki, M., pp. 137–141.

Dubinski, J. and Carlberg, R. G. (1991). “The Structure of Cold Dark Matter Halos”. In: ApJ vol. 378, p. 496.

Einstein, A (1917). “Sitzungsberichte Preussische Akademie der Wissenschaften Berlin”. In:

Faber, S. M. and Jackson, R. E. (1976). “Velocity dispersions and mass-to-light ratios for elliptical galaxies.” In: ApJ vol. 204, pp. 668–683.

Ferreira, E. G. M. (2020). “Ultra-Light Dark Matter”. In: arXiv e-prints, arXiv:2005.03254, arXiv:2005.03254. arXiv: 2005.03254 [astro-ph.CO].

Flores, R. A. and Primack, J. R. (1994). “Observational and Theoretical Constraints on Singular Dark Matter Halos”. In: ApJ vol. 427, p. L1. arXiv: astro-ph/9402004 [astro-ph].

Forman, W. et al. (1972). “Observations of the Extended X-Ray Sources in the Perseus and Coma Clusters from UHURU”. In: ApJ vol. 178, pp. 309–316.

Friedmann, A. (1922). “Über die Krümmung des Raumes”. In: Zeitschrift fur Physik vol. 10, pp. 377–386.

— (1924). “Über die Möglichkeit einer Welt mit konstanter negativer Krümmung des Raumes”. In: Zeitschrift fur Physik vol. 21, no. 1, pp. 326–332.

Garrison-Kimmel, S. et al. (2014). “ELVIS: Exploring the Local Volume in Simulations”. In: MNRAS vol. 438, no. 3, pp. 2578–2596. arXiv: 1310.6746 [astro-ph.CO].

Green, A. M., Hofmann, S., and Schwarz, D. J. (2004). “The power spectrum of SUSY-CDM on subgalactic scales”. In: MNRAS vol. 353, no. 3, pp. L23–L27. arXiv: astro-ph/0309621 [astro-ph].

Griffen, B. F. et al. (2016). “The Caterpillar Project: A Large Suite of Milky Way Sized Halos”. In: ApJ vol. 818, no. 1, 10, p. 10. arXiv: 1509.01255 [astro-ph.GA].

Gursky, H. et al. (1972). “X-Ray Emission from Rich Clusters of Galaxies”. In: ApJ vol. 173, p. L99.

Hinshaw, G. et al. (2009). “Five-Year Wilkinson Microwave Anisotropy Probe Observations: Data Processing, Sky Maps, and Basic Results”. In: ApJS vol. 180, no. 2, pp. 225–245. arXiv: 0803.0732 [astro-ph].

Hofmann, S., Schwarz, D. J., and Stöcker, H. (2001). “Damping scales of neutralino cold dark matter”. In: Phys. Rev. D vol. 64 (8), p. 083507.

Hopkins, P. F. et al. (2014). “Galaxies on FIRE (Feedback In Realistic Environments): stellar feedback explains cosmologically inefficient star formation”. In: MNRAS vol. 445, no. 1, pp. 581–603. arXiv: 1311.2073 [astro-ph.CO].

Hu, W., Barkana, R., and Gruzinov, A. (2000). “Fuzzy Cold Dark Matter: The Wave Properties of Ultralight Particles”. In: Phys. Rev. Lett. Vol. 85, no. 6, pp. 1158–1161. arXiv: astro-ph/0003365 [astro-ph].

Hubble, E. (1929). “A Relation between Distance and Radial Velocity among Extra-Galactic Nebulae”. In: Proceedings of the National Academy of Science vol. 15, no. 3, pp. 168–173.

Hui, L. et al. (2017). “Ultralight scalars as cosmological dark matter”. In: Phys. Rev. D vol. 95, no. 4, 043541, p. 043541. arXiv: 1610.08297 [astro-ph.CO].

Hunter, D. A. et al. (2012). “Little Things”. In: The Astrophysical Journal vol. 144, no. 5, 134, p. 134. arXiv: 1208.5834 [astro-ph.GA].

Jarosik, N. et al. (2007). “Three-Year Wilkinson Microwave Anisotropy Probe (WMAP) Observations: Beam Profiles, Data Processing, Radiometer Characterization, and Systematic Error Limits”. In: ApJS vol. 170, no. 2, pp. 263–287. arXiv: astro-ph/0603452 [astro-ph].

Jarosik, N. et al. (2011). “Seven-year Wilkinson Microwave Anisotropy Probe (WMAP) Observations: Sky Maps, Systematic Errors, and Basic Results”. In: ApJS vol. 192, no. 2, 14, p. 14. arXiv: 1001.4744 [astro-ph.CO].

Katz, N. (1992). “Dissipational Galaxy Formation. II. Effects of Star Formation”. In: ApJ vol. 391, p. 502.

Keller, B. W., Wadsley, J., and Couchman, H. M. P. (2015). “Cosmological galaxy evolution with superbubble feedback - I. Realistic galaxies with moderate feedback”. In: MNRAS vol. 453, no. 4, pp. 3499–3509. arXiv: 1505.06268 [astro-ph.GA].

Keller, B. W., Wadsley, J., and Couchman, H. M. P. (2016). “Cosmological galaxy evolution with superbubble feedback - II. The limits of supernovae”. In: MNRAS vol. 463, no. 2, pp. 1431–1445. eprint: https://academic.oup.com/mnras/article-pdf/463/2/1431/9685249/stw2029.pdf.

Keller, B. W. et al. (2014). “A superbubble feedback model for galaxy simulations”. In: MNRAS vol. 442, no. 4, pp. 3013–3025. arXiv: 1405.2625 [astro-ph.GA].

Kellogg, E. et al. (1973). “Clusters of Galaxies with a Wide Range of X-Ray Luminosities”. In: ApJ vol. 185, p. L13.

Kennicutt Robert C., J. (1998). “Star Formation in Galaxies Along the Hubble Sequence”. In: ARA&A vol. 36, pp. 189–232. arXiv: astro-ph/9807187 [astro-ph].

Kessler, R. et al. (2009). “First-Year Sloan Digital Sky Survey-II Supernova Results: Hubble Diagram and Cosmological Parameters”. In: ApJS vol. 185, no. 1, pp. 32–84. arXiv: 0908.4274 [astro-ph.CO].

Kimm, T. and Cen, R. (2014). “Escape fraction of ionizing photons during reionization: effects due to supernova feedback and runaway ob stars”. In: The Astrophysical Journal vol. 788, no. 2, p. 121.

Koopmans, L. V. E. and Treu, T. (2003). “The Structure and Dynamics of Luminous and Dark Matter in the Early-Type Lens Galaxy of 0047-281 at z = 0.485”. In: ApJ vol. 583, no. 2, pp. 606–615. arXiv: astro-ph/0205281 [astro-ph].

Kuhlen, M., Madau, P., and Silk, J. (2009). “Exploring Dark Matter with Milky Way Substructure”. In: Science vol. 325, no. 5943, p. 970. arXiv: 0907.0005 [astro-ph.GA].

Levi, M. et al. (2019). “The Dark Energy Spectroscopic Instrument (DESI)”. In: BAAS. Vol. 51, p. 57. arXiv: 1907.10688 [astro-ph.IM].

LSST Science Collaboration et al. (2009). “LSST Science Book, Version 2.0”. In: arXiv e-prints, arXiv:0912.0201, arXiv:0912.0201. arXiv: 0912.0201 [astro-ph.IM].

Maartens, R. et al. (2015). “Cosmology with the SKA – overview”. In: arXiv e-prints, arXiv:1501.04076, arXiv:1501.04076. arXiv: 1501.04076 [astro-ph.CO].

Marsh, D. J. E. (2016). “Axion cosmology”. In: Phys. Rep. Vol. 643, pp. 1–79. arXiv: 1510.07633 [astro-ph.CO].

Mather, J. C. et al. (1990). “A Preliminary Measurement of the Cosmic Microwave Background Spectrum by the Cosmic Background Explorer (COBE) Satellite”. In: ApJ vol. 354, p. L37.

Moore, B. (1994). “Evidence against dissipation-less dark matter from observations of galaxy haloes”. In: Nature vol. 370, no. 6491, pp. 629–631.

Navarro, J. F., Frenk, C. S., and White, S. D. M. (1996). “The Structure of Cold Dark Matter Halos”. In: ApJ vol. 462, p. 563. arXiv: astro-ph/9508025 [astro-ph].

Oh, S.-H. et al. (2015). “High-resolution mass models of dwarf galaxies from LITTLE THINGS”. In: The Astrophysical Journal vol. 149, no. 6, p. 180.

Oort, J. H. (1932). “The force exerted by the stellar system in the direction perpendicular to the galactic plane and some related problems”. In: Bull. Astron. Inst. Netherlands vol. 6, p. 249.

Oppenheimer, B. D. and Davé, R. (2006). “Cosmological simulations of intergalactic medium enrichment from galactic outflows”. In: MNRAS vol. 373, no. 4, pp. 1265–1292. arXiv: astro-ph/0605651 [astro-ph].

Penzias, A. A. and Wilson, R. W. (1965). “A Measurement of Excess Antenna Temperature at 4080 Mc/s.” In: ApJ vol. 142, pp. 419–421.

Percival, W. J. et al. (2010). “Baryon acoustic oscillations in the Sloan Digital Sky Survey Data Release 7 galaxy sample”. In: MNRAS vol. 401, no. 4, pp. 2148–2168. arXiv: 0907.1660 [astro-ph.CO].

Perlmutter, S. et al. (1999). “Measurements of Ω and Λ from 42 High-Redshift Supernovae”. In: ApJ vol. 517, no. 2, pp. 565–586. arXiv: astro-ph/9812133 [astro-ph].

Planck Collaboration et al. (2014). “Planck 2013 results. XVI. Cosmological parameters”. In: A&A vol. 571, A16, A16. arXiv: 1303.5076 [astro-ph.CO].

Planck Collaboration et al. (2016). “Planck 2015 results. XIII. Cosmological parameters”. In: A&A vol. 594, A13, A13. arXiv: 1502.01589 [astro-ph.CO].

Planck Collaboration et al. (2018). “Planck 2018 results. VI. Cosmological parameters”. In: arXiv e-prints, arXiv:1807.06209, arXiv:1807.06209. arXiv: 1807.06209 [astro-ph.CO].

Preskill, J., Wise, M. B., and Wilczek, F. (1983). “Cosmology of the Invisible Axion”. In: Phys. Rev. B vol. 120. Ed. by Srednicki, M., pp. 127–132.

Riess, A. G. et al. (1998). “Observational Evidence from Supernovae for an Accelerating Universe and a Cosmological Constant”. In: The Astrophysical Journal vol. 116, no. 3, pp. 1009–1038. arXiv: astro-ph/9805201 [astro-ph].

Riess, A. G. et al. (2009). “A Redetermination of the Hubble Constant with the Hubble Space Telescope from a Differential Distance Ladder”. In: ApJ vol. 699, no. 1, pp. 539–563. arXiv: 0905.0695 [astro-ph.CO].

Rubin, V. C., Ford W. K., J., and Thonnard, N. (1978). “Extended rotation curves of high-luminosity spiral galaxies. IV. Systematic dynamical properties, Sa -> Sc.” In: ApJ vol. 225, pp. L107–L111.

— (1980). “Rotational properties of 21 SC galaxies with a large range of luminosities and radii, from NGC 4605 (R=4kpc) to UGC 2885 (R=122kpc).” In: ApJ vol. 238, pp. 471–487.

Rubin, V. C. et al. (1985). “Rotation velocities of 16 SA galaxies and a comparison of Sa, SB and SC rotation properties.” In: ApJ vol. 289, pp. 81–104.

Rubin, V. C. and Ford W. Kent, J. (1970). “Rotation of the Andromeda Nebula from a Spectroscopic Survey of Emission Regions”. In: ApJ vol. 159, p. 379.

Schmidt, M. (1959). “The Rate of Star Formation.” In: ApJ vol. 129, p. 243.

Smith, B. D. et al. (2017). “GRACKLE: a chemistry and cooling library for astrophysics”. In: MNRAS vol. 466, no. 2, pp. 2217–2234. arXiv: 1610.09591 [astro-ph.CO].

Smith, M. C., Sijacki, D., and Shen, S. (2018). “Supernova feedback in numerical simulations of galaxy formation: separating physics from numerics”. In: MNRAS vol. 478, no. 1, pp. 302–331. arXiv: 1709.03515 [astro-ph.GA].

Smoot, G. F. et al. (1992). “Structure in the COBE Differential Microwave Radiometer First-Year Maps”. In: ApJ vol. 396, p. L1.

Springel, V. et al. (2008). “The Aquarius Project: the subhaloes of galactic haloes”. In: MNRAS vol. 391, no. 4, pp. 1685–1711. arXiv: 0809.0898 [astro-ph].

Springel, V. and Hernquist, L. (2003). “Cosmological smoothed particle hydrodynamics simulations: a hybrid multiphase model for star formation”. In: MNRAS vol. 339, no. 2, pp. 289–311. arXiv: astro-ph/0206393 [astro-ph].

Stadel, J. et al. (2009). “Quantifying the heart of darkness with GHALO - a multibillion particle simulation of a galactic halo”. In: MNRAS vol. 398, no. 1, pp. L21–L25. arXiv: 0808.2981 [astro-ph].

Steffen, F. D. (2009). “Dark-matter candidates. Axions, neutralinos, gravitinos, and axinos”. In: European Physical Journal C vol. 59, no. 2, pp. 557–588. arXiv: 0811.3347 [hep-ph].

Stinson, G. et al. (2006). “Star formation and feedback in smoothed particle hydrodynamic simulations - I. Isolated galaxies”. In: MNRAS vol. 373, no. 3, pp. 1074–1090. arXiv: astro-ph/0602350 [astro-ph].

Taoso, M., Bertone, G., and Masiero, A. (2008). “Dark matter candidates: a ten-point test”. In: J. Cosmology Astropart. Phys. Vol. 2008, no. 3, 022, p. 022. arXiv: 0711.4996 [astro-ph].

Teyssier, R. et al. (2013). “Cusp-core transformations in dwarf galaxies: observational predictions”. In: MNRAS vol. 429, no. 4, pp. 3068–3078. arXiv: 1206.4895 [astro-ph.CO].

Tyson, J. A., Valdes, F., and Wenk, R. A. (1990). “Detection of Systematic Gravitational Lens Galaxy Image Alignments: Mapping Dark Matter in Galaxy Clusters”. In: ApJ vol. 349, p. L1.

Vikhlinin, A. et al. (2006). “Chandra Sample of Nearby Relaxed Galaxy Clusters: Mass, Gas Fraction, and Mass-Temperature Relation”. In: ApJ vol. 640, no. 2, pp. 691–709. arXiv: astro-ph/0507092 [astro-ph].

Walker, M. G. and Peñarrubia, J. (2011). “A method for measuring (slopes of) the mass profiles of dwarf spheroidal galaxies”. In: The Astrophysical Journal vol. 742, no. 1, p. 20.

Walter, F. et al. (2008). “THINGS: The H I nearby galaxy survey”. In: The Astrophysical Journal vol. 136, no. 6, pp. 2563–2647.

Zwicky, F. (1937). “On the Masses of Nebulae and of Clusters of Nebulae”. In: ApJ vol. 86, p. 217.

Papers

Paper I

SCALAR: an AMR code to simulate axion-like dark matter models

Mattia Mina, David F. Mota, Hans A. Winther

Submitted for publication in *Astronomy & Astrophysics*, arXiv: 1906.12160.

I

Astronomy & Astrophysics manuscript no. main
June 26, 2020

SCALAR: an AMR code to simulate axion-like dark matter models

Mattia Mina[1], David F. Mota[1], and Hans A. Winther[1,2]

[1] Institute of Theoretical Astrophysics, University of Oslo, 0315 Oslo, Norway
e-mail: mattia.mina@astro.uio.no
[2] Institute of Cosmology & Gravitation, University of Portsmouth, Portsmouth, Hampshire, PO1 3FX, UK

Date

ABSTRACT

We present a new code, SCALAR, based on the high-resolution hydrodynamics and *N*-body code RAMSES, to solve the Schrödinger equation on adaptive refined meshes. The code is intended to be used to simulate axion or fuzzy dark matter models where the evolution of the dark matter component is determined by a coupled Schrödinger-Poisson equation, but it can also be used as a stand-alone solver for both linear and non-linear Schrödinger equations with any given external potential. This paper describes the numerical implementation of our solver and presents tests to demonstrate how accurately it operates.

Key words. methods: numerical, adaptive mesh refinement – cosmology: axion-like dark matter, structure formation

1. Introduction

The true nature of dark matter is not known. Weakly interacting massive particles (WIMP) are still considered one of the most likely candidates for cold dark matter (CDM), and several experiments are ongoing to try to detect such particles. These are, however, closing in on the neutrino floor where any signal would be drowned in the solar neutrino background (Monroe & Fisher 2007).

A promising alternative to WIMPs are ultra-light axions, fuzzy dark matter (Marsh 2016; Hui et al. 2017; Turner 1983; Press et al. 1990; Goodman 2000; Peebles 2000; Calabrese & Spergel 2016; Guzmán & Ureña-López 2003; Kim & Marsh 2016; Amendola & Barbieri 2006; Hu et al. 2000), and superfluid dark matter (Berezhiani & Khoury 2015; Khoury 2016, 2015; Sharma et al. 2019). These models have distinct and observable signatures on the small scales of structure formation, they are also are able to solve some of the discrepancies observed in CDM simulations, such as the missing satellites problem (Moore et al. 1999; Klypin et al. 1999), the cusp-core problem (de Blok 2010; Bar et al. 2018, 2019) and the too-big-to-fail problem (Boylan-Kolchin et al. 2011). These disparities could, however, have a solution within baryonic processes, which are usually not included in standard CDM simulations as shown in Macciò et al. (2012), Brooks et al. (2013), Governato et al. (2010), Madau et al. (2014), Teyssier et al. (2013), Governato et al. (2012), Pontzen & Governato (2012), Sawala et al. (2016), and Brooks et al. (2017). To understand this better, one should ideally perform simulations including both of these components.

In order to quantify the effects of axion-like dark matter models, one needs to either solve a Schrödinger-Poisson system or use the Mandelung formulation. The latter consists of a set of traditional hydrodynamics equations, with an additional pressure term which can be solved by using methods such as smoothed particle hydrodynamics (SPH), as proposed by Marsh (2015). However, it is known that numerical methods based on the Madelung formulation of quantum mechanics are troublesome in regions around voids. This formulation, indeed, breaks down where the density approaches zero and at interference nodes, as the quantum pressure term can easily become singular (Marsh 2015; Li et al. 2019).

The Schrödinger-Poisson system has several applications in cosmology. For instance, the six dimensional Vlasov equation describing collisionless self-gravitating matter is approximated by a Schrödinger-Poisson system for a complex wave-function in three dimensions. This was proposed as an alternative way for simulating CDM in Widrow & Kaiser (1993). It was later shown, by solving the Schrödinger-Poisson system and comparing it to the Vlasov solver ColDICE (Sousbie & Colombi 2016) in two dimensions, that one has excellent qualitative and quantitative agreement in the solution (Kopp et al. 2017). A similar study is given in Mocz et al. (2018), where the system was solved using a spectral method, demonstrating that one recovers the classical behaviour in the limit where $\hbar \to 0$.

Unfortunately, the methods employed in the above mentioned papers, despite being very accurate, are too expensive to perform high-resolution simulations in three dimensions. The first cosmological, high-resolution, simulation of fuzzy dark matter in three dimensions was performed in Schive et al. (2014) using the code GAMER (Schive et al. 2010, 2018). There, an explicit method, similar to the one we present in this paper, was used. In Veltmaat et al. (2018), they used the classical wave-function to perform zoom-in simulations to study the formation and evolution of ultralight bosonic dark matter halos from realistic cosmological initial conditions and in Mocz et al. (2017) they studied galaxy formation with Bose-Einstein condensate dark matter using a pseudo spectral method (see also Edwards et al. (2018)). There have also been a handful of papers that have performed simulations more in line with the hydrodynamical formulation. In Zhang et al. (2018), a new technique to discretise the quantum pressure is proposed and shown to reproduce the expected density profile of dark matter halos. In Nori & Baldi (2018), a module AX-GADGET for cosmological simulations using SPH inside the P-GADGET3 code is presented. These methods do not solve for the wave-function, but they have the advantage of being much less expensive to run than a full wave-

function solver like ours. There have also been simulations performed by using other numerical techniques in either two (Kopp et al. 2017) or three spatial dimensions (Woo & Chiueh 2009).

In this paper we present SCALAR (Simulation Code for ultrA Light Axions in RAMSES): a general adaptive mesh refinement (AMR) code to solve the Schrödinger-Poisson system. Our implementation is in the hydrodynamics and N-body code RAMSES (Teyssier 2002). The structure of the paper is as follows: in Section 2 we present the equations we are to solve, in Section 3 we present the numerical implementation, in Section 4 we present tests of the code and in Section 5 we discuss possible cosmological applications before concluding in Section 6.

2. Theoretical model

A Bose-Einstein condensate (BEC) is a system of identical bosons, where a large fraction of particles occupies the lowest quantum energy state, or the ground state. This phenomenon typically takes place in gases, at very low temperatures or very high densities and it was observed for the first time in Anderson et al. (1995) and Davis et al. (1995). In the condensate regime, these quantum systems behave as a macroscopic fluid and their peculiar features are a macroscopic manifestation of quantum effects.

In general, when Bose-Einstein condensation occurs, thermal de-Broglie wavelengths of particles start to overlap, as they become grater than the mean inter-particle distance. At this point, a coherent state develops and the system behaves as a macroscopic fluid, where only binary collisions are relevant. The dynamics of BECs is complicated, due to the difficulty in modelling particle self-interactions.

However, in the Hartree mean-field theory and in the limit of $T \to 0$, binary collisions are modelled via an effective potential and the whole quantum system can be described by a single-particle wave-function $\psi(\mathbf{x}, t)$ obeying the non-linear Schödinger equation:

$$i\hbar\frac{\partial\psi}{\partial t} = \left[-\frac{\hbar^2}{2m}\nabla^2 + g|\psi|^2 + mV_{\rm ext}\right]\psi, \tag{1}$$

where m is the mass of the boson and g is the self-interaction coupling constant. Often, the trapping potential $V_{\rm ext}(\mathbf{x}, t)$ is introduced by hand in order to model the presence of a trap, which is responsible for keeping particles confined.

The single-particle wave-function is normalised such that:

$$\int |\psi|^2 \, {\rm d}^3x = N, \tag{2}$$

where N is the total number of particles present in the system. As a consequence, the quantity $|\psi(\mathbf{x}, t)|^2$ represents the number density of particles.

An alternative description of the macroscopic fluid is provided by the so-called Madelung formulation of the Schrödinger equation. In this case, by expressing the single-particle wave-function in polar coordinates:

$$\psi = \sqrt{\frac{\rho}{m}}\exp\left(\frac{i}{\hbar}\theta\right), \tag{3}$$

the dynamics of the system is described in terms of mass density and velocity, which are macroscopic physical quantities and they are respectively defined as:

$$\rho(\mathbf{x}, t) = m|\psi(\mathbf{x}, t)|^2, \tag{4}$$

$$\mathbf{v}(\mathbf{x}, t) = \frac{1}{m}\nabla\theta(\mathbf{x}, t). \tag{5}$$

Thus, the Schrödinger equation can be cast into the following system of equations:

$$\frac{\partial\rho}{\partial t} + \nabla\cdot(\rho\mathbf{v}) = 0, \tag{6}$$

$$\frac{\partial\mathbf{v}}{\partial t} + (\mathbf{v}\cdot\nabla)\mathbf{v} = -\nabla\left(V_{\rm ext} + \frac{g}{m^2}\rho + Q\right), \tag{7}$$

which are known as the Madelung or quantum Euler equations. We recognise Eq. (6) as a continuity equation which expresses conservation of mass. Although the second Madelung equation, Eq. (7), expresses conservation of momentum, it is not the same as the classical momentum equation, as it contains an additional term Q, which is called quantum pressure and it is defined as:

$$Q \equiv -\frac{\hbar^2}{2m^2}\frac{\nabla^2\sqrt{\rho}}{\sqrt{\rho}}. \tag{8}$$

The quantum pressure is a macroscopic manifestation of quantum effects and it is characteristic of Bose-Einstein condensates.

In this formulation, by defining the velocity as in Eq. (5), we are intrinsically assuming that the fluid is irrotational, since:

$$\nabla\times\mathbf{v} = \nabla\times\nabla\theta = 0. \tag{9}$$

However, during the evolution of the wave-function, the phase can develop discontinuities of multiples of $2\pi\hbar$ and its gradient can subsequently generate vorticity in the field, as shown in Uhlemann et al. (2014, 2019).

In cosmology, these kinds of systems can be used to model the dark matter contribution to the energy budget of the Universe. In particular, in the last few decades, models where dark matter is a light boson, such as ultra-light axions or fuzzy dark matter, have received a lot of attention. Due to the small mass of these bosons, macroscopic quantum effects manifest at astronomically relevant scales. In these alternative dark matter models, new signatures are expected within the structure formation process at highly non-linear scales and, therefore, numerical simulations are required in order to explore these scenarios.

Here, the dynamics of dark matter is also described by a system of identical bosons gravitationally bounded. Therefore, the governing equation is a non-linear Schrödinger equation, Eq. (1), where the external potential is replaced by the gravitational potential. In this class of alternative dark matter models, self-interactions between bosons are often neglected, as the coupling constant g is usually parametrically small. The resulting system of equations describing the dynamics of the dark matter fluid is called Schrödinger-Poisson system and, for an expanding Universe, it reads:

$$i\hbar\left(\frac{\partial\psi}{\partial t} + \frac{3}{2}H\psi\right) = \left(-\frac{\hbar^2}{2ma^2}\nabla^2 + m_a\Phi\right)\psi, \tag{10}$$

$$\nabla^2\Phi = 4\pi G a^2\left(|\psi|^2 - |\psi(a)|^2\right), \tag{11}$$

where a is the scale-factor of the Universe, $H \equiv d\log(a)/dt$ is the Hubble rate of expansion, and Φ is the gravitational potential. With a change of variables $\psi \to a^{3/2}\psi$, the non-linear Schrödinger equation above takes on the form of Eq. (1).

3. Numerical methods

In this section we provide a brief overview of the code RAMSES and the AMR technique. Then, we discuss in details the numerical aspects of the algorithm we implemented in order to solve the non-linear Schrödinger equation. Throughout this section, the dimensionality of the problem is denoted by dim and it can be 1, 2 or 3.

3.1. Overview of RAMSES

The RAMSES code was originally designed for cosmological simulations of structure formation and subsequently extended to astrophysical applications. It consists of an *N*-body particle mesh (PM) code, which solves the gravitational dynamics of a set of macroparticles, sampling the phase space distribution of the dark matter component in the Universe. Through PM algorithms, the mass of each macroparticle is interpolated on a grid and the Poisson equation is solved in order to compute the gravitational potential. Thus, the gravitational force acting on each element of the system and the new phase space position of each macroparticle are computed by solving the corresponding *N*-body equation with a leapfrog scheme. In addition, RAMSES can solve the dynamics of the baryonic component present in the Universe. In this case, the grid is also used to sample gas parcels and the evolution of the system is described by the equations of hydrodynamics, which are solved by means of a Godunov scheme. For this purpose, Riemann solvers can be used for computing fluxes of conserved physical quantities among cells.

The RAMSES code implements an AMR strategy, where a hierarchy of nested grids is created in order to increase the local resolution according to a set of refinement criteria. In this way, RAMSES can solve accurately gas dynamics and gravitational potential only where more precision is actually needed. This approach reduces consistently the amount of memory needed in cosmological and hydrodynamical simulations, compared to the case where a uniform high-resolution grid is used.

In SCALAR, we rely on the efficient AMR implementation of RAMSES. In order to solve the dynamics of our theoretical model, the single-particle wave-function is sampled by using the original grid allocated by RAMSES for the Poisson and hydrodynamics equations. Also in this case, the AMR approach provides the opportunity to solve the Schrödinger equation with higher resolution only where features of the wave-function are more demanding.

3.2. Adaptive mesh refinement

The basic unit of the AMR hierarchy is an oct, which consists of a set of $2^{\rm dim}$ cells. At each level in the AMR hierarchy, a grid is a collection of octs with the same resolution. The grid with the coarsest resolution is called domain grid and it covers the whole computational domain. During the evolution of the physical system, when the solution starts to develop features and its tracking requires higher resolution, any cell at a given level can be split into a child oct, with double the resolution of the parent cell.

At each time-step, the AMR structure is modified according to a set of refinement criteria. First, for a generic level of refinement ℓ, a refinement map is created by marking all those cells satisfying at least one refinement criterion. Also cells violating the strict refinement rule are marked for refinement, in order to guarantee that each child oct at level $\ell + 1$ is surrounded by, at least, $3^{\rm dim} - 1$ neighbours at the coarser level. However, if a given cell at level ℓ does not satisfy any refinement criteria anymore, it is marked for de-refinement and subsequently its child octs are destroyed. Then, a new child oct is created at level $\ell + 1$ for each marked cell and all the relevant physical quantities are interpolated from level ℓ. Coarse-fine data interpolation, in an AMR context, is often called prolongation and it can be done by using any of the interpolation schemes which are described in the section below.

When computing the refinement map, physical quantities can fluctuate around the refinement threshold in subsequent time-steps. This means that, some cells at the boundary of a fine resolution region can be refined and de-refined many subsequent times. In this case, the refinement map tends to be quite noisy, since each interpolation operation where the solution is characterised by strong gradients introduces numerical noise in the solution of the non-linear Schrödinger equation. For this reason, once the refinement map is computed according to a given set of refinement criteria, a mesh smoothing operator is applied. For this purpose, a cubic buffer of $n_{\rm expand}$ cells around the computed map is additionally marked for refinement. In this way, even if cells octs are created and destroyed at coarse-fine boundaries, the interpolation procedure is applied in a regions where the wave-function is smoother and, thus, it introduces a lower level of numerical noise.

3.3. The Schrödinger equation

The SCALAR code evolves the solution of the non-linear Schrödinger equation by using a Taylor's method, similar to the one designed in GAMER. Given the wave-function $\psi(\mathbf{x}, t_0)$, the formal solution of the non-linear Schrödinger equation, Eq. (1), at time $t_1 = t_0 + \Delta t$ reads:

$$\psi(\mathbf{x}, t_1) = \hat{U}(t_1, t_0)\psi(\mathbf{x}, t_0), \tag{12}$$

where $\hat{U}(t_1, t_0)$ is the time evolution operator and it maps the solution of the Schrödinger equation at two different times. In the general case, the time evolution operator is defined as:

$$\hat{U}(t_1, t_0) = \exp\left(-\frac{i}{\hbar}\int_{t_0}^{t_1} \hat{H}(\mathbf{x}, t')\,\mathrm{d}t'\right), \tag{13}$$

where $\hat{H}(\mathbf{x}, t)$ denotes the Hamiltonian of the system. The operator $\hat{U}(t_1, t_0)$ has the main following properties:

- $\hat{U}(t, t) = 1$,
- $\hat{U}(t_1, t_2)\,\hat{U}(t_2, t_3) = \hat{U}(t_1, t_3)$,
- $\hat{U}(t_1, t_2) = \hat{U}^{\dagger}(t_2, t_1) = \hat{U}^{-1}(t_2, t_1)$.

In the limit of $\Delta t \ll 1$, then the following approximation holds:

$$\int_{t_0}^{t_1} \hat{H}(\mathbf{x}, t')\,\mathrm{d}t' \approx \hat{H}(\mathbf{x}, t_0)\,\Delta t, \tag{14}$$

and, therefore, Eq. (13) can be approximated as:

$$\hat{U}(t_1, t_0) \approx \exp\left(-\frac{i}{\hbar}\hat{H}(\mathbf{x}, t_0)\Delta t\right). \tag{15}$$

In the general case, the Hamiltonian $\hat{H}(\mathbf{x}, t)$ contains different contributions to the total energy of the system. In particular, we can express $\hat{H}(\mathbf{x}, t)$ as a sum of contributions describing kinetic and potential energies. Here, we denote these two operators respectively as $\hat{K}(\mathbf{x}, t)$ and $\hat{W}(\mathbf{x}, t)$, and they are defined as:

$$\hat{K}(\mathbf{x}, t) \equiv -\frac{\hbar^2}{2m}\nabla^2, \tag{16}$$

$$\hat{W}(\mathbf{x}, t) \equiv m\left(V(\mathbf{x}, t) + \frac{g}{m}|\psi(\mathbf{x}, t)|^2\right). \tag{17}$$

By means of the Lie-Trotter formula (Trotter 1959), the time evolution operator can be split as well:

$$\hat{U}(t_1, t_0) \approx \exp\left(-\frac{i}{\hbar}\hat{W}(\mathbf{x}, t_0)\Delta t\right)\exp\left(-\frac{i}{\hbar}\hat{K}(\mathbf{x}, t_0)\Delta t\right). \tag{18}$$

As a consequence, the formal solution of the Schrödinger equation can be written as:

$$\psi(\mathbf{x}, t_1) = \exp\left(-\frac{i}{\hbar}\hat{W}(\mathbf{x}, t_0)\Delta t\right)\exp\left(-\frac{i}{\hbar}\hat{K}(\mathbf{x}, t_0)\Delta t\right)\psi(\mathbf{x}, t_0). \quad (19)$$

In SCALAR , the two contributions to the time evolution operator are applied separately. First, the 'drift' due to the kinetic part of the Hamiltonian is approximated via Taylor expansion (here for dim = 3):

$$\begin{aligned}\bar{\psi}^{n+1}_{i,j,k} &= \exp\left(-\frac{i}{\hbar}\hat{K}(\mathbf{x}, t_0)\Delta t\right)\psi^n_{i,j,k} \\ &= \left[\sum_{N=0}^{\infty}\frac{1}{N!}\left(-\frac{i}{\hbar}\hat{K}(\mathbf{x}, t_0)\Delta t\right)^N\right]\psi^n_{i,j,k} \\ &= \left[1 + \left(\frac{i\hbar\Delta t}{2m}\nabla^2\right) + \frac{1}{2}\left(\frac{i\hbar\Delta t}{2m}\nabla^2\right)^2 + \dots\right]\psi^n_{i,j,k}, \end{aligned} \quad (20)$$

where, for a generic operator $\hat{O}$, the notation $\hat{O}^N$ denotes N consecutive applications of the same operator. In the SCALAR code, the Taylor expansion is performed up to $O(\Delta t^3)$, which is the minimum required by the stability analysis of the numerical scheme. Furthermore, the laplacian operator is discretised by a standard second-order finite difference formula:

$$\begin{aligned}\nabla^2\psi^n_{i,j,k} = &\frac{\psi^n_{i+1,j,k} + \psi^n_{i-1,j,k} - 2\psi^n_{i,j,k}}{\Delta x^2} + \\ &\frac{\psi^n_{i,j+1,k} + \psi^n_{i,j-1,k} - 2\psi^n_{i,j,k}}{\Delta x^2} + \\ &\frac{\psi^n_{i,j,k+1} + \psi^n_{i,j,k-1} - 2\psi^n_{i,j,k}}{\Delta x^2}. \end{aligned} \quad (21)$$

Then, the 'kick' due to the potential is computed and the wave-function at the new time-step reads:

$$\psi^{n+1}_{i,j,k} = \exp\left(-\frac{i}{\hbar}\hat{W}^n_{i,j,k}\Delta t\right)\bar{\psi}_{i,j,k}. \quad (22)$$

Here, the advantage of the Lie-Trotter splitting is clear: while the kinetic contribution to the time evolution operator needs Taylor expansion in order to be applied, the potential contribution only provides a phase rotation of the wave-function and it can be computed exactly.

Once the new wave-function is computed, the new mass density is computed according to:

$$\rho^{n+1}_{i,j,k}\big|_S = m\left|\psi^{n+1}_{i,j,k}\right|^2. \quad (23)$$

3.4. The continuity equation

In quantum mechanics, the time evolution operator is unitary, as expressed by its properties. This means that the mass density carried by the wave-function is conserved. This is true also if we consider separately the two contributions to the Hamiltonian. However, the Taylor expansion, Eq. (20), breaks the unitarity of the time evolution operator. Therefore, in order to improve the conservation properties of our main numerical scheme, we implement a secondary solver for the continuity equation associated to the non-linear Schrödinger equation.

Eq. (6) can be written in its conservative form:

$$\frac{\partial\rho}{\partial t} + \nabla\cdot\mathbf{j} = 0, \quad (24)$$

where $\rho(\mathbf{x}, t)$ represents the mass density. Here, the quantity $\mathbf{j}(\mathbf{x}, t)$ is the associated density current, or flux, and it is defined as:

$$\mathbf{j} \equiv -i\frac{\hbar}{2m}\left(\psi^*\nabla\psi - \psi\nabla\psi^*\right). \quad (25)$$

By explicitly considering real and imaginary part of the wave-function, the density current can also be expresses as:

$$\mathbf{j} = \frac{\hbar}{m}\left(\Re[\psi]\nabla\Im[\psi] - \Im[\psi]\nabla\Re[\psi]\right). \quad (26)$$

In SCALAR, Eq. (24) is discretised by using a first-order Godunov scheme:

$$\begin{aligned}\frac{\rho^{n+1}_{i,j,k} - \rho^n_{i,j,k}}{\Delta t} + &\frac{\left(J^{n+\frac{1}{2}}_{i+\frac{1}{2},j,k} - J^{n+\frac{1}{2}}_{i-\frac{1}{2},j,k}\right)}{\Delta x} \\ &+ \frac{\left(J^{n+\frac{1}{2}}_{i,j+\frac{1}{2},k} - J^{n+\frac{1}{2}}_{i,j-\frac{1}{2},k}\right)}{\Delta x} \\ &+ \frac{\left(J^{n+\frac{1}{2}}_{i,j,k+\frac{1}{2}} - J^{n+\frac{1}{2}}_{i,j,k-\frac{1}{2}}\right)}{\Delta x} = 0, \end{aligned} \quad (27)$$

where the time-centered fluxes are computed at cell interfaces. In order to compute the time-centered fluxes at cell interfaces, the wave-function is first computed at half time-step, by advancing the solution of $0.5\Delta t$. Then, the wave-function at cell interfaces is estimated in each dimension by linear interpolation:

$$\begin{aligned}\psi^{n+\frac{1}{2}}_{i+\frac{1}{2},j,k} &= \frac{\psi^{n+\frac{1}{2}}_{i,j,k} + \psi^{n+\frac{1}{2}}_{i+1,j,k}}{2}, \\ \psi^{n+\frac{1}{2}}_{i,j+\frac{1}{2},k} &= \frac{\psi^{n+\frac{1}{2}}_{i,j,k} + \psi^{n+\frac{1}{2}}_{i,j+1,k}}{2}, \\ \psi^{n+\frac{1}{2}}_{i,j,k+\frac{1}{2}} &= \frac{\psi^{n+\frac{1}{2}}_{i,j,k} + \psi^{n+\frac{1}{2}}_{i,j,k+1}}{2}. \end{aligned} \quad (28)$$

Its gradient, instead, is computed in each dimension by means of the first-order finite difference formula and it reads:

$$\begin{aligned}\nabla\psi^{n+\frac{1}{2}}_{i+\frac{1}{2},j,k} &= \frac{\psi^{n+\frac{1}{2}}_{i+1,j,k} - \psi^{n+\frac{1}{2}}_{i,j,k}}{\Delta x}, \\ \nabla\psi^{n+\frac{1}{2}}_{i,j+\frac{1}{2},k} &= \frac{\psi^{n+\frac{1}{2}}_{i,j+1,k} - \psi^{n+\frac{1}{2}}_{i,j,k}}{\Delta x}, \\ \nabla\psi^{n+\frac{1}{2}}_{i,j,k+\frac{1}{2}} &= \frac{\psi^{n+\frac{1}{2}}_{i,j,k+1} - \psi^{n+\frac{1}{2}}_{i,j,k}}{\Delta x}. \end{aligned} \quad (29)$$

Thus, the time-centered density current at cell interfaces is computed by means of Eq. (26).

However, this solver is not used to explicitly advance in time the mass density, but only to enforce the conservation of mass. Indeed, by denoting $\rho^{n+1}_{i,j,k}\big|_S$ and $\rho^{n+1}_{i,j,k}\big|_C$ the new mass densities computed by the main and the secondary solvers respectively, a correcting factor is computed as follows:

$$R = \frac{\rho^{n+1}_{i,j,k}\big|_C}{\rho^{n+1}_{i,j,k}\big|_S}, \quad (30)$$

which is used to rescale the wave-function.

Although by solving the continuity equation on top of the Schrödinger equation sensibly improves the conservation properties of the algorithm, this process does not ensure perfect conservation of mass. Since we truncate at the third order in time the Taylor expansion of the kinetic operator, Eq. (20), the kinetic solver introduces truncation errors in the solution of the Schrödinger equation. However, by rescaling the wave-function with the correct amplitude computed from the continuity equation, we are able to significantly reduce truncation errors, as shown by the improvement of several orders of magnitude on the conservation properties of SCALAR in the tests we present in Section 4. Unfortunately, the rescaling procedure is subject to accumulation of round-off errors, leading to an evolution of the error in the conservation of mass itself. However, the round-off errors are of the order of machine precision, in contrast to the much higher amplitude of the truncation errors introduced by the kinetic solver. This solution was already adopted in the GAMER code (Schive et al. 2014).

3.5. The solver

SCALAR solves the Schrödinger equation from the coarser to the finer level in the AMR hierarchy. For a generic refinement level ℓ, the optimal time-step is chosen as:

$$\Delta t = \min\left[C_K \cdot \frac{\sqrt{3}}{2\hbar} m(\Delta x)^2,\ \ C_W \cdot \frac{2\pi\hbar}{m|V_{\max}|}\right], \tag{31}$$

where $|V_{\max}|$ denotes the maximum absolute value of the effective potential $V + \frac{g}{m}|\psi|^2$. Here, C_K and C_W are Courant factors which are required to be smaller than one. The first term in the square brackets is determined by the Von Neumann stability analysis of the kinetic part of the solver. The second term, instead, requires that the phase of the wave-function does not rotate by a bigger angle than $2\pi C_W$ within a time-step. In general, the Courant factors C_K and C_W are chosen empirically, depending on the characteristics of the physical system that one aims to model. In our case, we set $C_K = C_W = 0.2$ since it provides a good accuracy on the solution of the non-linear Schrödinger equation, without sacrificing too much computation time. In Appendix A we provide a detailed discussion of the Von Neumann stability analysis of the numerical scheme.

In the original RAMSES code two different options are available regarding the choice of the time-step: a single or an adaptive time-step. While the former consists in using the same time-step for all refinement levels and it is determined by the finest level in the AMR hierarchy, the latter allows to use smaller time-steps for finer refinement levels. However, in case of adaptive time-step, for each coarse time-step at level ℓ it is possible to perform only two fine time-steps at level $\ell + 1$. In SCALAR, an additional option is available: a flexible time-step, where for each coarse time-step at level ℓ, the number of fine steps at level $\ell+1$ is flexible and it is determined by a level dependent Courant-Friedrichs-Lewy (CFL) condition. From Eq. (31), when the optimal time-step is chosen by the kinetic CFL condition, the time-step scales with the grid size as $\Delta t \propto \Delta x^2$, which represents a stricter condition than the usual case of hydrodynamics equations. Therefore, a flexible time-step can reduce significantly the total amount of coarse time-step in a simulation.

Within a generic level of refinement ℓ, SCALAR solves the non-linear Schrödinger equation for each oct separately. Thus, in order to advance the solution over a time-step, the solver proceeds as follows:

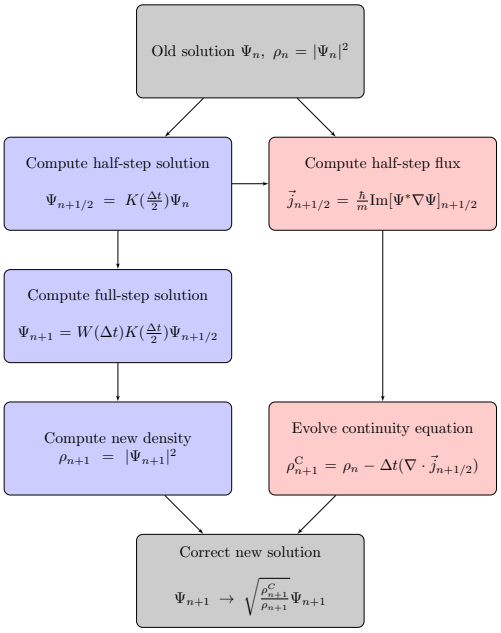

Fig. 1. Flowchart of the numerical algorithm implemented to solve the Schrödinger-Poisson system. The kinetic solver is shown in blue (left) and the continuity solver is shown in red (right).

1. For a given oct, a cubic buffer of neighbours cells is collected. The equations are actually solved only for the central oct, while the buffer cells are used to compute laplacians at each order of the Taylor expansion. If the central oct lies next to the coarse-fine boundary, the wave-function is interpolated into ghost cells from level $\ell - 1$.
2. The kinetic solver evolves the wave-function at the new time-step by means of Eq. (20). First, by advancing the solution by $0.5\Delta t$, the half time-step solution $\bar{\psi}^{n+1/2}_{i,j,k}$ is estimated from $\psi^n_{i,j,k}$ and it is used later in order to compute the mass density currents. Then, the full-step solution $\bar{\psi}^{n+1}_{i,j,k}$ and the new mass density $\rho^{n+1}_{i,j,k}\big|_S$ are computed.
3. The wave-function at half time-step $\bar{\psi}^{n+1/2}_{i,j,k}$ is interpolated at cell interfaces by using Eqs. (28)–(29) and the time-centered density currents are computed by means of Eq. (26).
4. The continuity equation is solved and the new mass density $\rho^{n+1}_{i,j,k}\big|_C$ is computed via Eq. (27).
5. The rescaling factor given by Eq. (30) is computed and $\bar{\psi}^{n+1}_{i,j,k}$ is rescaled in order to preserve mass conservation.
6. If the given oct lies next to the coarse-fine boundary, the estimated flux is stored for the subsequent reflux operation.
7. Finally, the phase rotation due to the potential is computed by applying Eq. (22) to $\bar{\psi}^{n+1}_{i,j,k}$, and $\psi^{n+1}_{i,j,k}$ is evaluated.

All steps, except the first and the last ones, are performed separately for each physical dimension. This procedure is called dimensional splitting and it reduces a N-dimensional problem into a system of N one dimensional problems. It has the advantage of relaxing the CFL condition of the solver and, therefore, it allows bigger time-steps. A flowchart of our solver is shown in Fig. (1).

3.6. Refinement strategy

In SCALAR, we implement the same 'quasi-Lagrangian' approach as RAMSES uses for hydrodynamics: when the total mass of a given cell exceeds a given threshold, the cell is marked for refinement. The level dependent density threshold is defined as:

$$\rho_\ell = \frac{M_c}{(\Delta x_\ell)^{\dim}}, \tag{32}$$

where M_c corresponds to the maximum mass allowed per cell.

In addition, following Schive et al. (2014) and the FLASH code (Fryxell et al. 2000), we implement support for the invariant version of the Löhner error estimator. It is based on the second derivative of a given physical quantity, normalised by the first derivative. Considering a generic physical quantity f, the error estimator E_L reads:

$$E_L = \left\{ \frac{\sum_{ij} \left(\frac{\partial^2 f}{\partial x_i \partial x_j} \right)^2}{\sum_{ij} \left[\frac{1}{2\Delta x_j} \left(\left| \frac{\partial f}{\partial x_i} \right|_{i+1} + \left| \frac{\partial f}{\partial x_i} \right|_{i-1} \right) + \xi \frac{|\bar{f}_{ij}|}{\Delta x_i \Delta x_j} \right]^2} \right\}^{1/2}, \tag{33}$$

where the indices i,j run over each physical dimensions. Small fluctuations of the physical quantity f are filtered out due to the presence of the second term at denominator. The quantity $|\bar{f}_{ij}|$ is an average of f over dimensions i,j and ξ is a small constant. This error estimator is dimensionless and therefore it can be applied to any physical quantity. Furthermore, in Eq. (33), E_L is bounded in the interval $[0,1]$. In SCALAR, we apply the Löhner error estimator separately to $\Re[\psi]$ and $\Im[\psi]$. Then, the final estimation of the error on the wave-function is given by:

$$E_L = \sqrt{\left(E_L^{\Re}\right)^2 + \left(E_L^{\Im}\right)^2}, \tag{34}$$

and if it exceeds a user-defined threshold, the cell is marked for refinement. This threshold can be chosen empirically, depending on the features one needs to resolve in the solution of the governing equations. Although it is currently implemented in SCALAR, we did not employed the Löhner error estimator in the test we present here, in Section 4. In general, while testing separately the implementation of the Löhner error estimator, we find that a value of $E_L = 0.7$ provides a good balance between computational cost and accuracy for the solution of the non-linear Schrödinger equation.

3.7. Spatial and temporal interpolation.

In SCALAR, interpolation is required when a generic level ℓ in the AMR hierarchy is refined and new child octs are created at level $\ell+1$, or when, during the solving process, boundary conditions need to be specified for a fine-grid patch and ghost cells are created. In both cases, the wave-function at the coarse level ℓ is interpolated down to level $\ell+1$. In order to solve the equations of motion, when the laplacian operator is applied, any discontinuity in the second derivative of the wave-function introduces an error, which propagates into the solution of the non-linear Schrödinger equation and it can destroy the wave-function. Therefore, high-order interpolation schemes are implemented in order to keep the wave-function as smooth as possible.

In particular, in SCALAR, we implement two high-order interpolation schemes. In both cases, the interpolating function is a fourth-order polynomial, but the coefficients of the polynomials are chosen in different ways. In one case, Lagrange basis polynomials are computed in order to set the coefficients, resulting in a fourth-order Lagrange interpolation scheme. In the second case, fourth-order conservative interpolation is performed and the coefficients of the interpolation are set by requiring that cell averages of the interpolated quantities are preserved. In case of adaptive time integration, linear temporal interpolation can also be applied when computing boundary conditions for a fine level patch, since coarse-grid and fine-grid wave-functions can be discretised at different times.

Furthermore, the interpolation can be performed on two different sets of variables: the original set of variables $\Re[\psi]$ and $\Im[\psi]$, or derived variables $m|\psi|^2$ and $\mathrm{Arg}[\psi]$, corresponding to mass density and phase of the wave-function. The interpolation schemes and the set of variables used for the interpolation process can be specified by the user in the parameter file.

Further details on the interpolation schemes can be found in Appendix B.

3.8. Artificial viscosity

In the tests shown in the upcoming sections, when they were done at the domain level only, the solution of the non-linear Schrödinger equation remains stable for as long as we could run SCALAR. However, when refinements were included, the solver had the tendency to develop spurious high-frequency waves at coarse-fine boundary, even after improving the order of accuracy of interpolation schemes. In order to artificially dump spurious oscillations, we introduced an empirical viscosity term in the non-linear Schrödinger equation. Thus, incorporating the viscosity term, the non-linear Schrödinger equation, Eq. (1), is replaced by:

$$i\hbar \frac{\partial \psi(\mathbf{x},t)}{\partial t} = \left[-\frac{\hbar}{2m}(1 - i\epsilon)\nabla^2 + g|\psi(\mathbf{x},t)|^2 + mV_{\mathrm{ext}}(\mathbf{x},t) \right] \psi(\mathbf{x},t), \tag{35}$$

where the constant $\epsilon > 0$ quantifies the strength of the damping term. For example, if we consider a single plane-wave:

$$\psi \propto \exp(i\omega t - ikx), \tag{36}$$

the viscosity term acts in a similar way as a Gaussian filter, by dumping the wave-function by a factor of:

$$\exp\left(-\frac{k^2 \epsilon t}{2m} \right). \tag{37}$$

This means that, including the artificial viscosity, the wave-function is simply replaced by:

$$\psi \rightarrow \psi \exp\left(-\frac{k^2 \epsilon t}{2m} \right), \tag{38}$$

In this way, the filter leaves untouched physical low frequency modes in the wave-function, while smoothing the spurious numerical oscillations. In general, an artificial viscosity term would affect mass conservation. However, by solving the continuity equation on top of the non-linear Schrödinger equation, mass conservation is enforced and the artificial viscosity simply acts as a viscous force. Indeed, if we consider the Madelung formulation of quantum mechanics instead, Eq. (6) and Eq. (7), the artificial viscosity term would be placed, together with the quantum force, in the momentum equation. Thus, Eq. (7) would read:

$$\frac{\partial v}{\partial t} + (\mathbf{v}\cdot\nabla)\mathbf{v} = -\nabla\left(V + \frac{g}{m^2}\rho + Q - \frac{\epsilon}{2m}\frac{\nabla(\rho \mathbf{v})}{\rho} \right). \tag{39}$$

The new viscous force term:

$$F_{\rm viscous} = -\frac{\epsilon}{2m}\nabla\left(\frac{\nabla(\rho\mathbf{v})}{\rho}\right),$$

helps preventing high-frequency waves to build up in time. With the addition of such a viscosity term, we are able to evolve without any issues the wave-function over hundreds of oscillation periods in our tests and, at the same time, preserving mass, energy and agreement with analytical solutions. There is no unique prescription for solving these issues we encountered and, in general, it is possible to design more elaborate artificial viscosity terms.

In an AMR context, when choosing the value of the dumping constant ϵ, one should keep in mind that spurious high-frequency oscillations appear on scales of the local grid resolution, which is not fixed, but it changes according to designed refinement criteria. Thus, the strength of the dumping term should be decided such that it does not over-suppress the wave-function in high-resolution regions, but rather slightly under-suppress spurious oscillations in low-resolution regions. Such a limitation of the artificial viscosity term we implemented motivates further investigations to develop a more accurate scheme for dumping high-frequency spurious oscillations. Empirically, we find that a value in the range $0.2 < \epsilon < 1$ ensures stability over a long time in all the test cases we present (except the soliton test case, were we set $\epsilon = 0$ and we do not use any artificial viscosity), by preventing the growth of spurious oscillations in the solution of the non-linear Schödinger equation.

3.9. Code units

We adopt the set of 'super-comoving coordinates' introduced in Martel & Shapiro (1998), and already used in RAMSES. Thus, the following change of variables is performed:

$$\begin{aligned} \tilde{x} &= \frac{x}{aL}, \quad d\tilde{\tau} = \frac{H_0 \mathrm{d}t}{a^2}, \quad \tilde{\psi} = \frac{\psi}{\overline{\psi}}, \\ \tilde{V} &= \frac{Va^2}{(H_0 L)^2}, \quad \tilde{m} = \frac{mH_0L^2}{\hbar}, \quad \tilde{g} = \frac{a^2 g}{H_0\hbar|\overline{\psi}|^2}, \end{aligned} \tag{40}$$

where H_0 is the Hubble constant, L is the box size, and $\overline{\psi}$ is chosen to ensure that $\int |\tilde{\psi}|^2 \, \mathrm{d}^{\rm dim}\tilde{x} = 1$. As a consequence, the resulting non-linear Schrödinger equation reads:

$$i\frac{d\tilde{\psi}}{d\tilde{\tau}} + \frac{1}{2\tilde{m}}\tilde{\nabla}^2\tilde{\psi} - \tilde{m}\tilde{V}\tilde{\psi} - \tilde{g}|\tilde{\psi}|^2\tilde{\psi} = 0. \tag{41}$$

This set of coordinates was specifically designed for cosmological applications. However, it can be used for any application by setting the scale factor a to unity and replacing H_0 by a general inverse time scale T^{-1}. In the remainder of the paper, all equations are in these code units.

For the particular case of axion dark matter in a cosmological setting (see Eq. (10)) we have $\tilde{g} = 0$, $\overline{\psi} \propto a^{-3/2}$, and the potential is determined via the Poisson equation:

$$\begin{aligned} \tilde{\nabla}^2\tilde{V} = \frac{3}{2}a\Big[&\Omega_{\rm axions}(|\tilde{\psi}|^2 - 1) + \Omega_{\rm CDM}(\tilde{\rho}_{\rm CDM} - 1) \\ &+ \Omega_{\rm baryons}(\tilde{\rho}_{\rm baryons} - 1) + \dots\Big], \end{aligned} \tag{42}$$

where Ω_i is the fraction of the energy budget of our Universe that is in matter component i (axions, baryons, CDM, etc.) and the mean value of $\tilde{\rho}_i$ over the box is set to unity.

4. Tests of the code

In this section we present the numerical experiments we performed in order to test the main features of SCALAR. When testing the accuracy of our numerical schemes, we rely on three main tests: conservation of mass, energy, and reproduction of analytical solutions. Given the total mass $M(t)$ in the simulation box and the total energy $E(t)$, the corresponding errors are respectively defined as:

$$\epsilon_{\rm mass} = \left|\frac{M(t) - M(0)}{M(0)}\right| \quad \text{and} \quad \epsilon_{\rm energy} = \left|\frac{E(t) - E(0)}{E(0)}\right|.$$

Instead, by denoting the analytical solution as $\psi_{\rm a}(x,t)$ and the numerical solution as $\psi_{\rm n}(x,t)$, at a given time, the error with respect to the analytical solution is computed according to the following formula:

$$\epsilon_{\rm solution} = \frac{\left\langle(\psi_{\rm a}(x,t) - \psi_{\rm n}(x,t))^2\right\rangle_x}{\left\langle\psi_{\rm a}^2(x,t)\right\rangle_x}.$$

where $\langle\ \rangle_x$ denotes the mean over the box. For the tests we present here, we always assume that each cell in the AMR grid has the same size in all dimensions: $\Delta x = \Delta y = \Delta z$. Furthermore, in all the tests, we only employ the refinement criterion based on density, as we found no need to use the Löhner error estimator in order to achieve an accurate and stable solution over time.

Accuracy and performances. While running the tests we discuss in this section, we measured the overall accuracy and performances of the numerical algorithms implemented in SCALAR.

The accuracy of a numerical method is often measured by comparing the analytical solution with the numerical solution. For this purpose, we compute the error with respect to the analytical solution as given above. The overall accuracy of SCALAR is obtained by measuring how the global error, computed at a given time, scales with the grid spacing. In Fig. 2, we show the sample of errors we obtained for one of the numerical experiments we performed, the soliton test. The data points are fitted by the formula:

$$\log_2(y) = \alpha\log_2(x) + \beta,$$

where x and y represents the grid size and the error with respect to the analytical solution, respectively. The parameters of the fit α and β are determined by means of the Linear Least Square (LLS) method and, in this case, we obtain $\alpha \sim 1.8$ and $\beta \sim 6.7$. While β is not relevant when measuring the convergence of a numerical scheme, the parameter α represents the slope of the fitting polynomial and it corresponds to the global accuracy of the solver. Thus, for SCALAR, we achieve an overall second-order accuracy.

We measured general performances of SCALAR on a small cluster. Every node of the cluster is equipped with two Intel E5-2670 processors, with 8 cores each, a clock frequency of $f_{\rm CPU} = 2.6$ GHz and a total memory of 128 GB. Nodes within the cluster are interconnected through a Mellanox 56 Gb FDR Inifniband. In application with gravity enabled, SCALAR can evolve the solution of the non-linear Schrödinger equation by updating a single cell in the AMR hierarchy in $\sim 11\ \mu$s. This means that, our code is able to reach a value of $\sim 10^5$ cell updated per second.

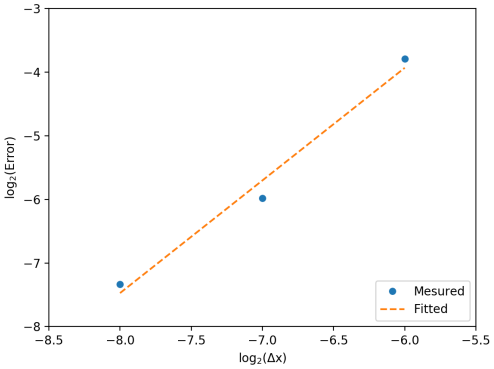

Fig. 2. Overall accuracy of the numerical scheme implemented to solve the Schrödinger-Poisson system. Blue points represent errors with respect to the analytical solution for the soliton test, computed at a given time for $\Delta x = 2^{-8}, 2^{-7}, 2^{-6}$. The orange dashed line corresponds to the polynomial fit.

Conservation of mass. The non-linear Schrödinger equation has the conserved quantity:

$$M = \int |\psi|^2 \, \mathrm{d}^{\mathrm{dim}}x,$$

which in the Mandelung formulation is just the total mass of the fluid. Mass and energy are not manifestly conserved by the main solver, therefore monitoring them is a useful test.

In simulations with no refinements and without enforcing mass conservation, we typically find the error on the conservation of mass of the order of (the prefactor is here for $\Delta x = 2^{-6}$):

$$\frac{\Delta M}{M} \sim 10^{-6}\left(\frac{t}{T}\right),$$

where T is the oscillation period. When we allow for refinements, the situation is typically worse and it is not good enough for cosmological simulations. However, by solving the continuity equation on top of the Schrödinger equation, we observe an improvement on the conservation of mass up to:

$$\frac{\Delta M}{M} \sim 10^{-13}\left(\frac{t}{T}\right).$$

This does not change when we allow refinements and, even though the error grows linearly in time, it is good enough in order to perform cosmological simulations. This is shown in Fig. (3), where we perform the sine wave test on the domain grid only, with a resolution of $N_{\mathrm{cell}} = 2^6$ cells, corresponding to $\ell = 6$ and $\Delta x = 2^{-6}$, in one dimension. Details regarding the sine wave test are described in Section 4.1.

Please, refer to Section 3 for an explanation of the temporal evolution of the error in the conservation of mass.

Conservation of energy. Since we enforce mass conservation by solving the continuity equation, energy conservation is a better accuracy test for our code. By defining kinetic and potential energy as:

$$K \equiv \frac{1}{2m^2}\int |\nabla\psi|^2 \, \mathrm{d}^{\mathrm{dim}}x, \tag{43}$$

$$W \equiv \frac{1}{2}\int V_{\mathrm{eff}}|\psi|^2 \, \mathrm{d}^{\mathrm{dim}}x, \tag{44}$$

the temporal change in the total energy of the system is expressed by:

$$\frac{d}{dt}(K+W) = \frac{1}{2}\int \frac{\partial V_{\mathrm{eff}}}{\partial t}|\psi|^2 \, \mathrm{d}^{\mathrm{dim}}x. \tag{45}$$

As we can see, in the case where the effective potential has no explicit time-derivatives, the energy $E = K + W$ is conserved under the evolution.

In a cosmological setting, the potential V depends on time via the scale-factor and this leads to a Lazyer-Irvine equation (Kopp et al. 2017):

$$\frac{d}{dt}(K+W) - HW = 0, \tag{46}$$

which can be monitored by integrating it up while performing the simulation.

Comparison to analytical solutions. The most stringent test we can perform is to directly compare the numerical solution with an analytical solution. However, the discretised version of the governing equations is a different problem than the theoretical continuous limit and, thus, it admits a different solution. Usually, the main difference between the solutions of the continuous and the discretised non-linear Schrödinger equations leads to the wave-function evolving with slightly different temporal phases. For this reason, we estimate the phase difference between the two solutions and, starting from the analytical solution of the continuous non-linear Schrödinger equation, we compute the theoretical solution of the discretised equation. Then, we compare the numerical solution with the proper solution of the discretised non-linear Schrödinger equation. This represents a way of comparing the numerical solution with the one of the physical problem we are actually modelling. In the limit of $\Delta x \to 0$, the solutions of the continuous and the discretised non-linear Schrödinger equations converge to the same solution. In this way, we show that the numerical solution is in excellent agreement with the theoretical solution of the discretised problem, even in the case when the resolution is not extremely high, where computation time would significantly increase.

In the plots below we show, for different choices of initial conditions and potential, the error on the conservation of mass, the error on the conservation of energy, and the error with respect to the analytical solution.

4.1. Sine wave

The sine wave test evolves a static one dimensional density profile, where the initial wave-function is set as:

$$\psi(x, 0) = \sin(2\pi n x). \tag{47}$$

It evolves in a constant potential, which is defined as:

$$V = 1 - \frac{2\pi^2 n^2}{m^2}, \tag{48}$$

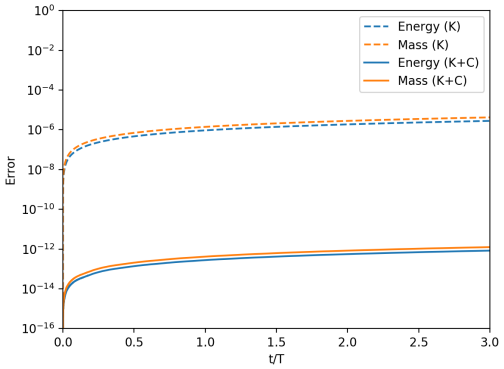

Fig. 3. Errors in conservation of mass and energy when solving the Schrödinger equation only (K) and when solving together the Schrödinger and the continuity equations (K+C). Solving the continuity equation together with the Schrödinger equation improves the conservation properties of the algorithm by ~ 6 orders of magnitude.

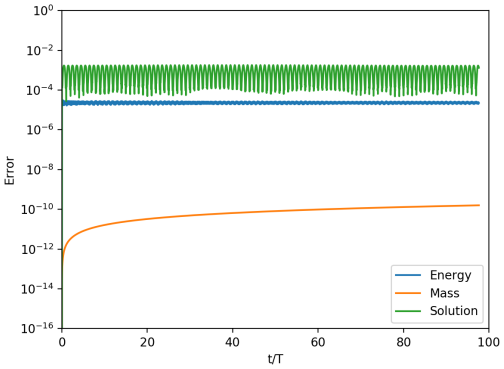

Fig. 4. Evolution of the three errors as a function of time for the cosine wave test. While the error on the conservation of mass (orange) evolves accordingly to $\Delta M/M \sim 10^{-13}(t/T)$, the error on the conservation of energy (blue) stays constant. Furthermore, the error with respect to the analytical solution (green) does not evolve over time.

where m is the mass carried by the wave-function and the period of oscillation is given by:

$$T = \frac{2\pi}{m}. \tag{49}$$

The full analytical solution reads:

$$\psi(x,t) = e^{-i\frac{2\pi t}{T}} \sin(2\pi n x). \tag{50}$$

This numerical experiment is designed to test the creation of ghost cells when computing fine levels boundary conditions. Here we only refine according to the mass criterion, Eq. (32) and, since the density profile does not evolve in time, there is no dynamical creation or destruction of grids: once the refinement map is computed at the beginning, it does not change. We evolve the solution of the Schrödinger equation over 100 periods of oscillation. It is possible to show that the solution of the discretised equation - the one we are solving - is the same as Eq. (50), up to second order in space, but with a slightly different period of oscillation. Therefore, to factor out the dependence of the period with resolution (which we test seperately), we correct the analytical solution by replacing T with $T_{\rm discrete}$, where:

$$\begin{aligned}\frac{T_{\rm discrete}}{T} &= \frac{1}{1 + T^2 n^2 \left(\frac{1-\cos(2\pi n \Delta x)}{(2\pi n \Delta x)^2} - \frac{1}{2}\right)} \\ &\approx \frac{1}{1 - \frac{\pi^2 T^2 n^2}{12}\Delta x^2}.\end{aligned} \tag{51}$$

This test was performed for dim $=$ 1. The non-linear Schrödinger equation is solved together with the continuity equation, in order to enforce conservation of mass. The domain grid resolution is $N_{\rm cell} = 64$, corresponding to $\ell = 6$ and $\Delta x = 2^{-6}$, and the maximum refinement level is set to $\ell_{\rm max} = 8$. When boundary conditions for fine levels are needed, phase and density are interpolated in ghost cells by means of fourth-order conservative interpolation. We used artificial viscosity with $\epsilon = 0.2$. The results from this test are shown in Fig. (4).

We have also performed a similar test using a quadratic potential leading to a Gaussian profile:

$$\psi \propto \exp\left(-\frac{x^2}{\sigma^2}\right),$$

with very similar results.

4.2. Travelling wave

This test simulates a one dimensional wave-packet travelling through a periodic box. Here, we test dynamical creation and destruction of grids, since the AMR hierarchy follows the density profile moving towards the direction of the wave. In this case, we have no potential and the initial conditions are defined as:

$$\psi(x,0) = \frac{1}{\sqrt{2}}\left[e^{ik_1 x} + e^{ik_2 x}\right], \tag{52}$$

where $k_1 = 2\pi n_1$, $k_2 = 2\pi n_2$ with $n_1 \neq n_2 \in \mathbb{N}$. The oscillation frequency of a single mode is:

$$\omega(k) = \frac{k^2}{2m},$$

and the analytical solution of the Schrödinger equation reads:

$$\psi(x,t) = \frac{1}{\sqrt{2}}\left[e^{i(k_1 x - \omega(k_1)t)} + e^{i(k_2 x - \omega(k_2)t)}\right]. \tag{53}$$

As a consequence, the density is given by:

$$|\psi(x,t)|^2 = 1 + \cos\left(2\pi x(n_2 - n_1) + \frac{2\pi t}{T}\right), \tag{54}$$

where the oscillation period is defined as:

$$T = \frac{m}{\pi(n_1^2 - n_2^2)}. \tag{55}$$

The wave-function is evolved in time over 100 oscillation periods. The non-linear Schrödinger equation is solved together with

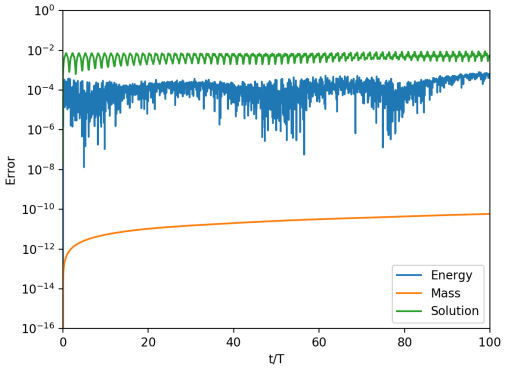

Fig. 5. Evolution of the three errors as a function of time for the travelling wave test. While the error on the conservation of mass (orange) evolves accordingly to $\Delta M/M \sim 10^{-13}(t/T)$, the error on the conservation of energy (blue) stays roughly constant. Furthermore, the error with respect to the analytical solution (green) does not evolve over time.

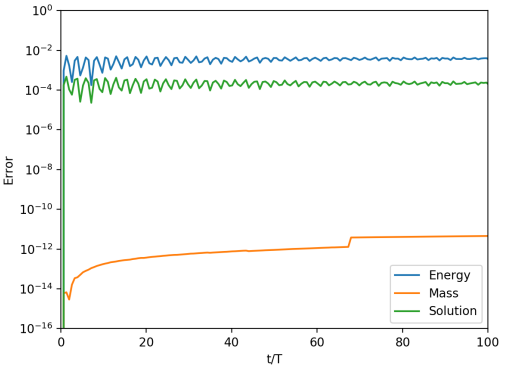

Fig. 6. Evolution of the three errors as a function of time, for a self-gravitating soliton. While the error on the conservation of mass (orange) evolves accordingly to $\Delta M/M \sim 10^{-13}(t/T)$, the error on the conservation of energy (blue) stays constant. Furthermore, the error with respect to the analytical solution (green) does not evolve over time.

the continuity equation, in order to enforce conservation of mass. Also in this case, the coarse-fine data interpolation is performed by means of fourth-order conservative interpolation. However, while density and phase are interpolated in ghost cells, new refinements are made by interpolating real and imaginary parts of the wave-function. The domain grid has the same resolution as in the previous test and refinements are allowed up to $\ell_{\max} = 8$. We used artificial viscosity with $\epsilon = 0.2$. The results from this test are shown in Fig. (5).

4.3. Soliton

In a cosmological context, SCALAR can be used to simulate the structure formation process with fuzzy dark matter. In this case, the density profiles of the dark matter halos differs from the case of the standard CDM. We can find a stationary solution which can be tested by taking:

$$\psi(x,t) = e^{-i\frac{2\pi t}{T}}\chi(x),$$

and solving the resulting ODE for $\chi(x)$. A numerical fit to the density profile of a soliton in three dimensions was first suggested in Schive et al. (2014) and then in Marsh & Pop (2015). Despite it is an approximated solution, it is useful when coupling the Poisson equation to the non-linear Schrödinger equation. In this works, the density profile of the soliton was found to be on the form:

$$\rho \propto \frac{1}{[1 + (r/r_{\rm core})^2]^8}, \tag{56}$$

where $r_{\rm core}$ can be chosen as a free parameter, see Appendix C for more details.

We set this density profile analytically and evolve the system. The density profile remains approximately stationary while the wave-function oscillates as:

$$\psi(x,t) \propto e^{-i\frac{2\pi t}{T}}.$$

This test was performed for dim $= 3$ and the non-linear Schrödinger equation is solved together with the continuity equation. The domain grid contains $N_{\rm cell} = 64^3$ cells, corresponding to $\ell = 6$ and $\Delta x = 2^{-6}$, and the maximum refinement level allowed is $\ell = 8$. In this case, both refinement and ghost cells are made by fourth-order conservative interpolation on density and phase. The artificial viscosity term is set to $\epsilon = 0$. We found that self-gravity is able to stabilise the wave-function against spurious numerical oscillations. We tested the same physical case with different values of artificial viscosity, but we did not find any improvement in terms of accuracy. In the other tests, where we set $\epsilon = 0.2$, the artificial viscosity term was introduced just in order to ensure stability and accuracy of the solution to the non-linear Schrödinger equation over a very large number of oscillation periods. The results for this test are shown in Fig. (6).

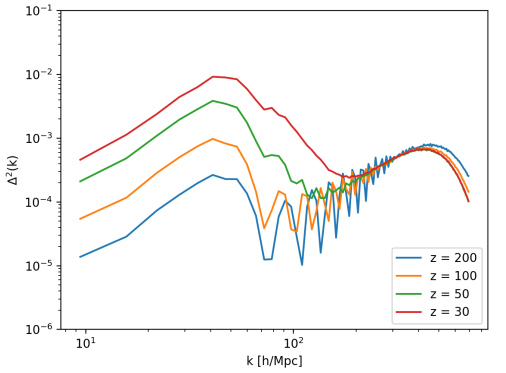

Fig. 7. Evolution of the dimensionless power spectrum $\Delta^2(k)$ with redshift.

5. Cosmological applications

The SCALAR code was originally developed in order to perform numerical simulations of structure formation with fuzzy

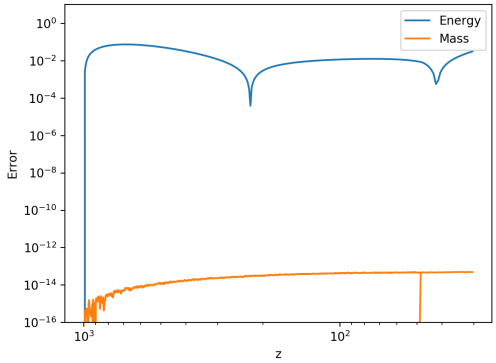

Fig. 8. Evolution of the errors on conservation of mass (orange) and energy (blue), as a function of redshift.

dark matter. To demonstrate the capabilities of our code, in this section we present a test involving a full 3D cosmological setup.

The simulation box models a $B_0 = 1$ Mpc/h portion of the Universe expanding over time, according to the Einstein-de Sitter model. We take $\Omega_\Lambda = 0.7$ and $\Omega_M = 0.3$, and the Hubble constant is set to $H_0 = 100\,h$ km s^{-1} Mpc^{-1}, where $h = 0.67$. The base resolution, which defines the domain level, is set to $N_{\rm cell} = 256^3$ and up to one level of refinement is allowed. This means that, in this test, we achieve a maximum resolution of $\Delta x \sim 4\ h^{-1}$kpc. The mass of the boson is set to $m = 10^{-21}$ eV and conservation of mass is enforced by solving the continuity equation on top of the non-linear Schrödinger equation. In order to better appreciate the differences between CDM and fuzzy dark matter, the initial conditions are computed for the case of CDM. The initial density and velocity fields are computed by using the Zel'dovich approximation. Then, following Kopp et al. (2017), we convert them into an initial wave-function.

The evolution starts at redshift $z = 1000$ and we run the simulation as long as we are able to resolve the quantum force with at least two cells, meaning until redshift $z = 30$. We did not run this simple test further because, due to lack of resolution, we cannot resolve the inner part of collapsed objects. This will be the subject of an upcoming paper.

In Fig. 9, Fig. 10 and Fig. 11 we show the dark matter density field, the real and the imaginary parts of the wave-function for a selection of redshifts, $z = 200, 100, 50, 30$. As the field clusters under the effect of gravity, the wave-function develops the wave patterns which are characteristic of this class of models.

By taking the density contrast $\delta(\mathbf{x})$ inside the simulation box, we expand it in Fourier modes as follows:

$$\delta(\mathbf{x}) = \int d^3k\, \delta(\mathbf{k}) \exp(-i\mathbf{k}\cdot\mathbf{x}). \tag{57}$$

The matter power spectrum is defined by means of the autocorrelation function, which can be expressed as:

$$\langle \delta(\mathbf{x})\, \delta(\mathbf{x}) \rangle = \int_0^\infty \frac{dk}{k} \frac{k^3 |\delta(k)|^2}{2\pi^2} \tag{58}$$

$$= \int_0^\infty \frac{dk}{k} \frac{k^3 P(k)}{2\pi^2}. \tag{59}$$

In Fig. 7, we plot the dimensionless power spectrum, defined as:

$$\Delta^2(k) = \frac{k^3 P(k)}{2\pi^2}, \tag{60}$$

for $z = 200, 100, 50, 30$. The results here show the same quantitative behaviour as seen in Woo & Chiueh (2009, see Fig. 2), that performed the same kind of simulation as we do here. As the field gravitationally collapses, the quantum pressure leaves immediately its imprints on $\Delta(k)$ by producing the characteristic suppression of power at small scales, above $k \sim 300\ h^{-1}$Mpc. Given the mass of the boson, the suppression scale is expected to be around the redshift dependent Jeans wave-number, which can be defined as:

$$k_J = \left(\frac{16\pi G \rho_a}{1+z} m^2\right)^{1/4}$$

$$= 66.5 \left(\frac{\Omega_a}{0.12 h^2}\right)^{1/4} \left(\frac{m}{10^{-22}\ \mathrm{eV}}\right)^{1/2} (1+z)^{-1/4} \frac{h}{\mathrm{Mpc}}, \tag{61}$$

where Ω_a is the dimensionless density parameter of axions and h is the dimensionless Hubble constant. Between $k = 10\ h^{-1}$Mpc and $k = 100\ h^{-1}$Mpc, the power spectrum describes modes in the density field still in the linear regime and, therefore, $\Delta^2(k)$ evolves with redshift according to linear theory:

$$\Delta^2 \propto (1+z)^{-2},$$

in a similar way to the CDM case.

In Fig. 8, the evolution of errors in conservation of mass and energy are plotted against redshift. The error in the conservation of mass slowly evolves in time, as described in Section 4. Furthermore, we track the evolution of the error in the conservation of energy, by integrating the Lazyer-Irvine equation along the simulation and checking at which level of accuracy Eq. (46) is satisfied. As shown in the same figure, in the conservation of energy does not grow significantly, thus ensuring that no energy is numerically dissipated by the solver or the artificial viscosity term.

6. Conclusions

In SCALAR, we implemented a set of numerical algorithms developed in order to solve the non-linear Schrödinger equation in an AMR framework. Eq. (1) can be used to describe the dynamics of a Bose-Einstein condensate, a system of identical bosons in the ground energy state, by means of a single-particle wave-function in a mean field approach. Here, the non-linearity arises from an effective potential, which can contain both a self-interaction term and a generic external potential. Bose-Einstein condensates find their application in several fields. As an example, alternative dark matter models involving Bose-Einstein condensates have been recently developed, such as ultra-light axion dark matter, fuzzy dark matter and superfluid dark matter. The Schrödinger equation is solved with a Taylor method, similar to the algorithm developed in GAMER. In order to improve the conservation properties of the numerical scheme, the continuity equation is solved on top of the non-linear Schrödinger equation and mass conservation is enforced by construction. Empirically, by running several tests, we found that our numerical method is second-order accurate.

In order to test the main components of SCALAR, a test suite was designed. In particular, we tested the performances of the solver with and without solving the continuity equation on top

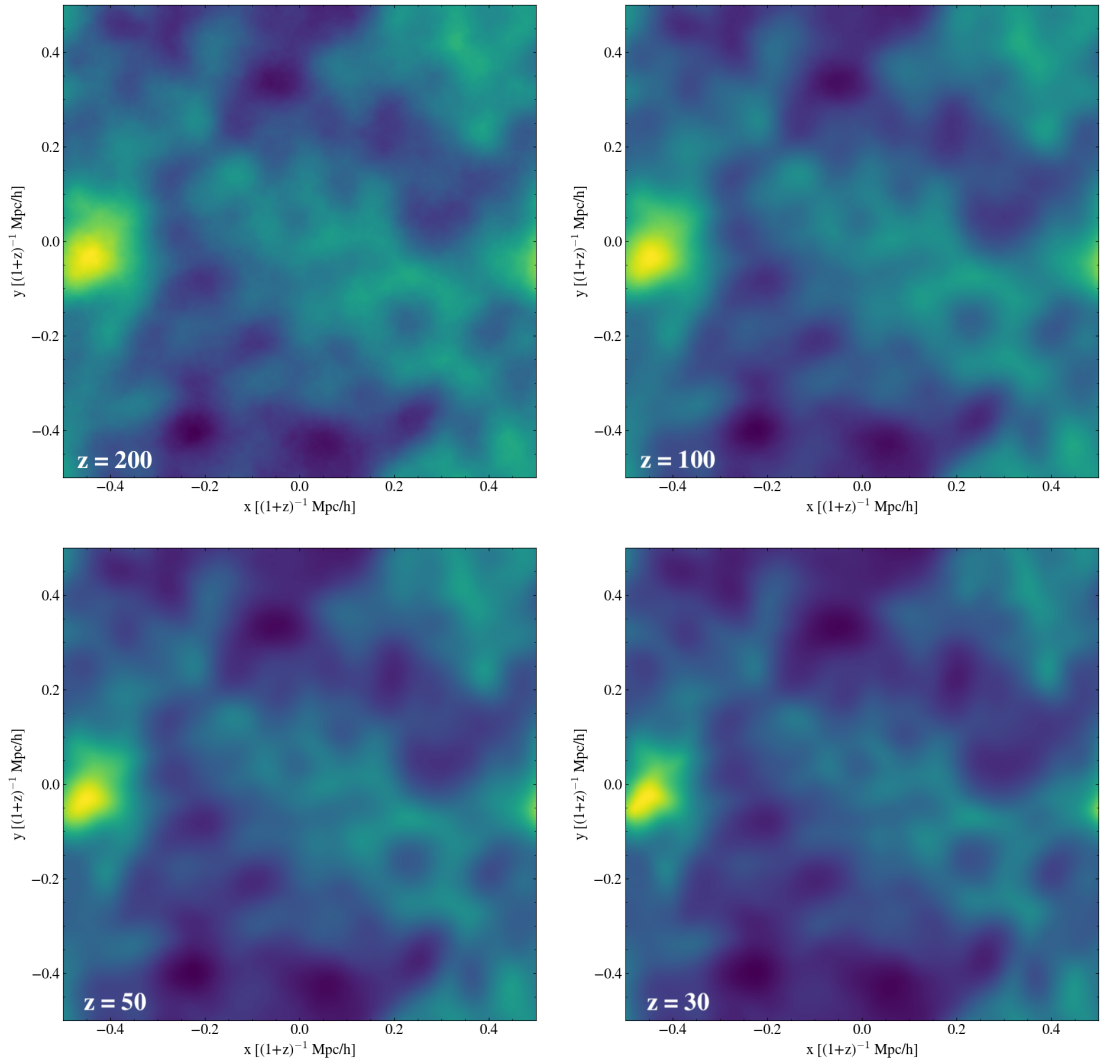

Fig. 9. Projection along the z axes of the dark matter density field, normalised by the critical density of the Universe. The box is 1 Mpc/h in comoving units and it represents the entire simulation box.

of the non-linear Schrödinger equation, the creation of ghost cells when boundary conditions need to be specified for levels with fine resolution and the dynamical creation and destruction of grids during the process of mesh refinement. For this purpose, we tracked mass and energy conservation properties of our numerical schemes during the evolution of the system. The result is that both mass and energy are well conserved. While the latter remains roughly constant in all the different cases, the former evolves in time. Indeed, the error on the conservation of mass grows according to:

$$\frac{\Delta M}{M} \sim 10^{-6}\left(\frac{t}{T}\right),$$

for all our test-cases as we advance the solution in time. However, by solving the continuity equation on top of the non-linear Schrödinger equation, the error on the conservation of mass improves of several orders of magnitude, growing as:

$$\frac{\Delta M}{M} \sim 10^{-13}\left(\frac{t}{T}\right),$$

and it remains significantly small even for cosmological simulations. Furthermore, we compared the numerical solutions found by `SCALAR` with the analytical solutions of all the test cases. We show that the numerical solution tracks very well the analytical one over a long evolution time. In this case also, the error with respect to the analytical solution remains roughly constant over time. We showed that high-frequency spurious oscillations

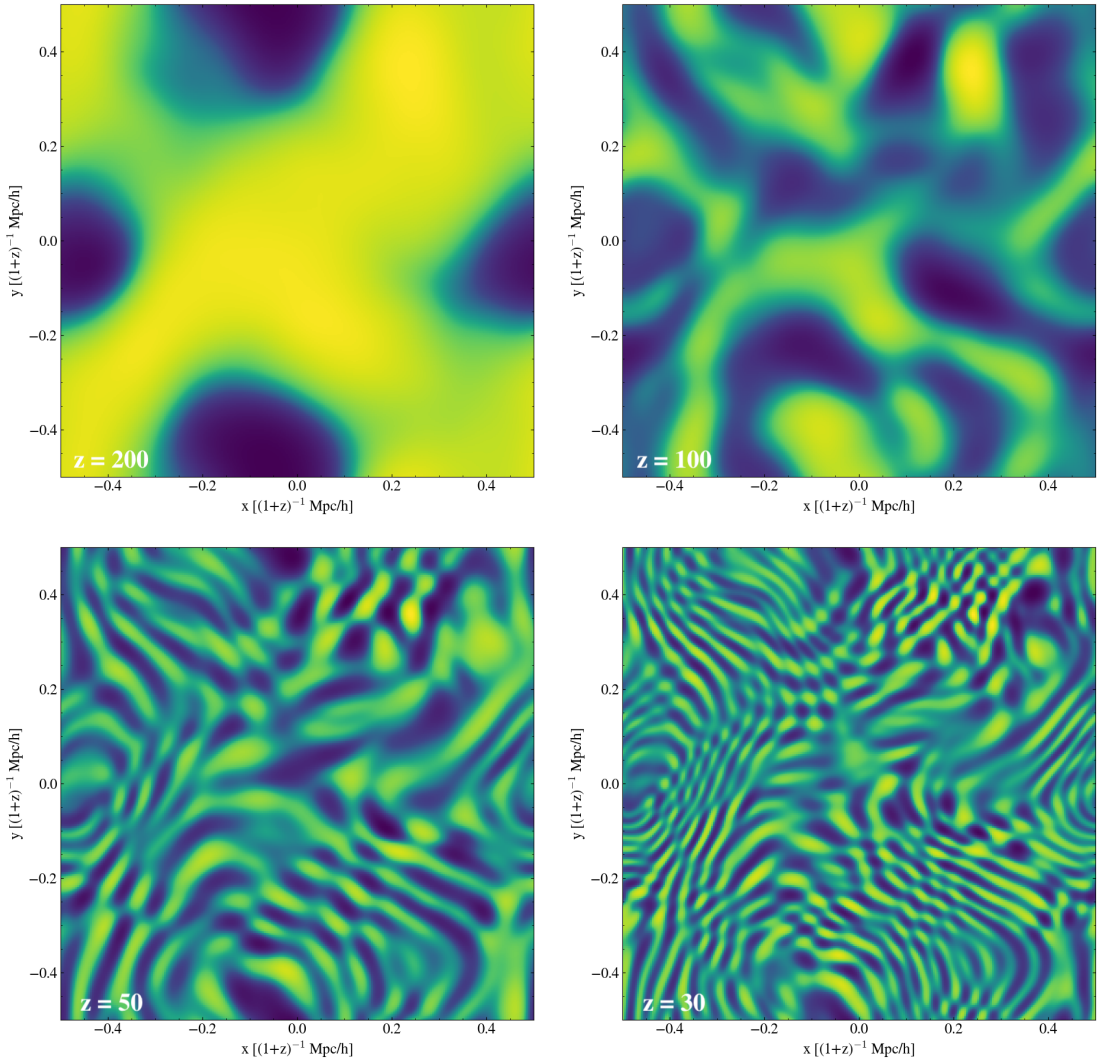

Fig. 10. Projection along the z axes of the real part of the dark matter field. The box is 1 Mpc$/h$ in comoving units and it represents the entire simulation box.

created at coarse-fine boundaries by interpolation schemes are efficiently dumped by an artificial viscosity term. However, the long term evolution of the single-particle wave-function still represents a challenge in case the artificial viscosity term is not included. We also run a small cosmological simulation where we show that SCALAR is able to capture the relevant features of models like fuzzy dark matter on cosmological scales.

Future work will aim at developing new high-order interpolation schemes which will not require the inclusion of an artificial viscosity term. Furthermore, we plan to compare the performance and accuracy of SCALAR with similar codes. In a following paper, we plan to exploit SCALAR to explore the non-linear regime of the structure formation with alternative dark matter models. In particular, we want to run a set of high-resolution cosmological simulation in order to verify and provide further predictions of fuzzy dark matter.

The code will be soon publicly available through our GitHub repository[1].

Acknowledgements. We thank the Research Council of Norway for their support. Computations were performed on resources provided by UNINETT Sigma2 – the National Infrastructure for High Performance Computing and Data Storage in Norway. HAW was supported by the European Research Council through 646702 (CosTesGrav). We also thank the anonymous referee for several suggestions that helped improve the paper.

[1] http://github.com/mattiamina

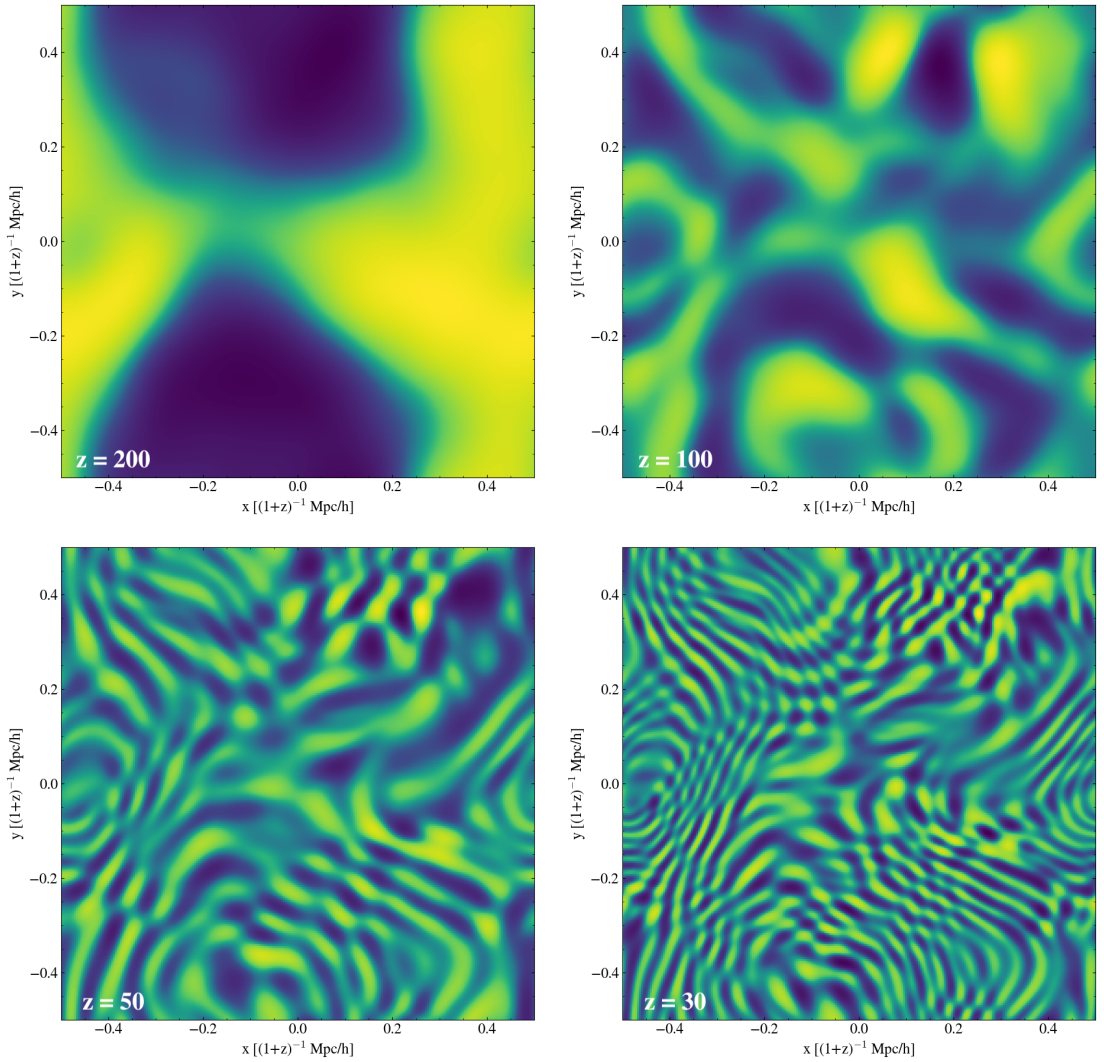

Fig. 11. Projection along the z axes of the imaginary part of the dark matter field. The box is 1 Mpc/h in comoving units and it represents the entire simulation box.

References

Amendola, L. & Barbieri, R. 2006, Physics Letters B, 642, 192
Anderson, M. H., Ensher, J. R., Matthews, M. R., Wieman, C. E., & Cornell, E. A. 1995, Science, 269, 198
Bar, N., Blas, D., Blum, K., & Sibiryakov, S. 2018, PRD, 98, 083027
Bar, N., Blum, K., Eby, J., & Sato, R. 2019, PRD, 99, 103020
Berezhiani, L. & Khoury, J. 2015, Phys. Rev. D, 92, 103510
Boylan-Kolchin, M., Bullock, J. S., & Kaplinghat, M. 2011, MNRAS, 415, L40
Brooks, A. M., Kuhlen, M., Zolotov, A., & Hooper, D. 2013, Astrophys. J., 765, 22
Brooks, A. M., Papastergis, E., Christensen, C. R., et al. 2017, ApJ, 850, 97
Calabrese, E. & Spergel, D. 2016, Monthly Notices of the Royal Astronomical Society, 460, 4397
Charney, J. G., Fjörtoft, R., & Von Neumann, J. 1950, Tellus, 2, 237
Davis, K. B., Mewes, M. O., Andrews, M. R., et al. 1995, Phys. Rev. Lett., 75, 3969
de Blok, W. J. G. 2010, Advances in Astronomy, 2010, 789293
Edwards, F., Kendall, E., Hotchkiss, S., & Easther, R. 2018, JCAP, 2018, 027
Fryxell, B., Olson, K., Ricker, P., et al. 2000, Astrophysical Journal, Supplement, 131, 273
Goodman, J. 2000, New Astronomy, 5, 103
Governato, F., Brook, C., Mayer, L., et al. 2010, Nature, 463, 203
Governato, F., Zolotov, A., Pontzen, A., et al. 2012, MNRAS, 422, 1231
Guzmán, F. & Ureña-López, L. 2003, Phys. Rev. D, 68, 024023
Hu, W., Barkana, R., & Gruzinov, A. 2000, Phys. Rev. Lett., 85, 1158
Hui, L., Ostriker, J. P., Tremaine, S., & Witten, E. 2017, Phys. Rev. D, 95, 043541
Khoury, J. 2015, arXiv e-prints, arXiv:1507.03013
Khoury, J. 2016, arXiv e-prints, arXiv:1605.08443
Kim, J. E. & Marsh, D. J. E. 2016, Phys. Rev. D, 93, 025027
Klypin, A., Kravtsov, A. V., Valenzuela, O., & Prada, F. 1999, ApJ, 522, 82
Kopp, M., Vattis, K., & Skordis, C. 2017, Phys. Rev. D, 96, 123532
Li, X., Hui, L., & Bryan, G. L. 2019, Phys. Rev. D, 99, 063509
Macciò, A. V., Stinson, G., Brook, C. B., et al. 2012, ApJ, 744, L9
Madau, P., Shen, S., & Governato, F. 2014, ApJL, 789, L17

Marsh, D. J. E. 2015, Phys. Rev. D, 91, 123520
Marsh, D. J. E. 2016, PhysRep, 643, 1
Marsh, D. J. E. & Pop, A.-R. 2015, MNRAS, 451, 2479
Martel, H. & Shapiro, P. R. 1998, MNRAS, 297, 467
Mocz, P., Lancaster, L., Fialkov, A., Becerra, F., & Chavanis, P.-H. 2018, Phys. Rev. D, 97, 083519
Mocz, P., Vogelsberger, M., Robles, V. H., et al. 2017, MNRAS, 471, 4559
Monroe, J. & Fisher, P. 2007, Phys. Rev. D, 76, 033007
Moore, B., Ghigna, S., Governato, F., et al. 1999, ApJ, 524, L19
Nori, M. & Baldi, M. 2018, ArXiv e-prints [arXiv:1801.08144]
Peebles, P. J. E. 2000, The Astrophysical Journal, 534, L127
Pontzen, A. & Governato, F. 2012, MNRAS, 421, 3464
Press, W. H., Ryden, B. S., & Spergel, D. N. 1990, Phys. Rev. Lett., 64, 1084
Sawala, T., Frenk, C. S., Fattahi, A., et al. 2016, MNRAS, 457, 1931
Schive, H.-Y., Chiueh, T., & Broadhurst, T. 2014, Nature Physics, 10, 496
Schive, H.-Y., Tsai, Y.-C., & Chiueh, T. 2010, ApJS, 186, 457
Schive, H.-Y., ZuHone, J. A., Goldbaum, N. J., et al. 2018, MNRAS, 481, 4815
Sharma, A., Khoury, J., & Lubensky, T. 2019, Journal of Cosmology and Astro-Particle Physics, 2019, 054
Sousbie, T. & Colombi, S. 2016, Journal of Computational Physics, 321, 644
Teyssier, R. 2002, AAP, 385, 337
Teyssier, R., Pontzen, A., Dubois, Y., & Read, J. I. 2013, MNRAS, 429, 3068
Trotter, H. F. 1959, Proceedings of the American Mathematical Society, 10, 545
Turner, M. S. 1983, Phys. Rev. D, 28, 1243
Uhlemann, C., Kopp, M., & Haugg, T. 2014, Phys. Rev. D, 90, 023517
Uhlemann, C., Rampf, C., Gosenca, M., & Hahn, O. 2019, Phys. Rev. D, 99, 083524
Veltmaat, J., Niemeyer, J. C., & Schwabe, B. 2018, Phys. Rev. D, 98, 043509
Widrow, L. M. & Kaiser, N. 1993, ApJL, 416, L71
Woo, T.-P. & Chiueh, T. 2009, ApJ, 697, 850
Zhang, J., Sming Tsai, Y.-L., Kuo, J.-L., Cheung, K., & Chu, M.-C. 2018, ApJ, 853, 51

Appendix A: Stability analysis

The stability condition of a generic PDE solver can be easily found by means of the Von Neumann stability analysis (Charney et al. 1950). For this purpose, the numerical error is decomposed in Fourier modes and a condition on time-step is computed in order to propagate each mode accurately.

We start by considering a generic mode in the Fourier decomposition of the numerical error:

$$\epsilon_m = e^{at} e^{ik_m x}. \tag{A.1}$$

As mentioned in the previous sections, in SCALAR we use a second-order finite difference formula in order to approximate the laplacian of the wave-function. Thus, for a generic quantity, in one physical dimension we have:

$$\nabla^2 f = \frac{f_{i+1} + f_{i-1} - 2f_i}{\Delta x^2}. \tag{A.2}$$

As a consequence, the second derivative of the error can be written as:

$$\nabla^2 \epsilon = -\frac{4}{(\Delta x)^2} \sin^2\left(\frac{k\Delta x}{2}\right)\epsilon, \tag{A.3}$$

and the amplification factor can be computed as:

$$\xi = \frac{\epsilon(t+\Delta t)}{\epsilon(t)} \tag{A.4}$$

$$= e^{-imV\Delta t}\left[1 + i\beta - \frac{\beta^2}{2!} - \ldots + \frac{(i\beta)^n}{n!}\right], \tag{A.5}$$

where β corresponds to:

$$\beta = -\frac{2\hbar\Delta t}{m(\Delta x)^2} \sin^2\left(\frac{k\Delta x}{2}\right). \tag{A.6}$$

In order to avoid exponential growth, we require that $|\xi| < 1$. Therefore, the stability condition reads:

$$|\xi|^2 = \cos_n^2(\beta) + \sin_n^2(\beta) < 1, \tag{A.7}$$

where $\cos_n$ and $\sin_n$ denote to n^{th} order Taylor polynomials of $\cos(x)$ and $\sin(x)$, respectively. Furthermore, n corresponds to the order of the Taylor expansion of the kinetic contribution to the time evolution operator, Eq.(20).

In particular, we find that for $n < 3$ the numerical scheme is unconditionally unstable. For $n = 3$, instead, the stability condition is satisfied as long as:

$$|\beta| < \sqrt{3} \implies \Delta t < C_K \frac{\sqrt{3}}{2\hbar} m(\Delta x)^2. \tag{A.8}$$

The generalisation to D can be done by replacing $(\Delta x)^2 \to (\Delta x)^2/D$ in the formula above.

We also require that the phase angle does not rotate more than $2\pi C_W$ within a time-step. Thus, for the kinetic term we require that:

$$\Delta t < C_K \cdot \frac{\pi m(\Delta x)^2}{\hbar}. \tag{A.9}$$

while for the potential term:

$$\Delta t < C_W \cdot \frac{2\pi\hbar}{m|V_{\max}|}. \tag{A.10}$$

Combining the three conditions above, the optimal time-step is chosen as:

$$\Delta t < \min\left[C_K \cdot \frac{\sqrt{3}}{2\hbar} m\,(\Delta x)^2,\ \ C_W \cdot \frac{2\pi\hbar}{m|V_{\max}|}\right], \tag{A.11}$$

where we require the safety factors to be $C_W, C_K < 1$.

Appendix B: Prolongation operators

The details related to the interpolation schemes we implement in SCALAR are given for the one dimensional case. In case of multidimensional interpolation, the same formulas derived in this section are applied sequentially in each direction.

For simplicity, in order to derive the interpolation formulas we use in SCALAR, we assume that there is an odd number $2N+1$ of coarse data points $\{x_i, y_i\}$ with $-N \le i \le N$ and the interpolation is always done for children of the central cell, as shown in Fig. (B.1).

In this way, we can construct an interpolating polynomial of order $2N$ starting from its general definition:

$$P(x) = \sum_{n=-N}^{N} a_n x^n. \tag{B.1}$$

In order to find an explicit expression for $P(x)$, the coefficients $\{a_n\}$ have to be computed and, depending on the constraints imposed on the interpolating polynomial, different schemes can be implemented.

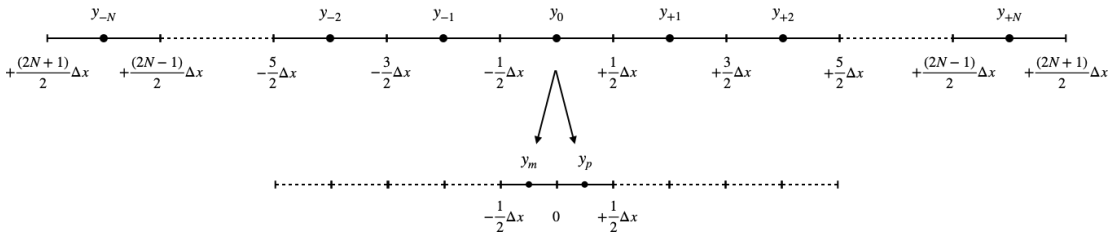

Fig. B.1. Coarse-fine grid interpolation.

Lagrange polynomial interpolation

For this interpolation scheme, instead of explicitly computing the coefficients a_n, the interpolating polynomial is expressed as a linear combination of Lagrange basis functions $l_j(x)$, with $j = -N, -N+1, \ldots, N-1, N$, which are defined as:

$$l_j(x) = \prod_{\substack{m=-N \\ m\neq j}}^{N} \frac{x - x_m}{x_j - x_m}. \tag{B.2}$$

Thus, coarse data points y_i weight the Lagrange basis functions and the interpolating polynomial is constructed as follows:

$$P(x) = \sum_{n=-N}^{N} y_n \, l_n(x). \tag{B.3}$$

In this way, the interpolating polynomial is forced to pass through the data points in the sample. In order to find an explicit formula for a fourth-order Lagrange interpolating polynomial, we directly compute the Lagrange basis functions by means of Eq. (B.2). Here, we express the differences between cell positions in Eq. (B.2) as a function of Δx. Then, the interpolating polynomial is computed at children cell positions, leading to the following interpolation formulas:

$$y_m = \frac{-45\, y_{-2} + 420\, y_{-1} + 1890\, y_0 - 252\, y_{+1} + 35\, y_{+2}}{2048}, \tag{B.4}$$

$$y_p = \frac{+35\, y_{-2} - 252\, y_{-1} + 1890\, y_0 + 420\, y_{+1} - 45\, y_{+2}}{2048}. \tag{B.5}$$

Conservative polynomial interpolation

In this case, constraints on the coefficients of the interpolating polynomial are set by imposing that the mean of the interpolated data on fine cells is equal to the data stored in the coarse cell.

By using Eq. (B.3), the coarse data points are redefined by means of their cell average:

$$\tilde{y}_i = \frac{1}{\Delta x} \int_{\frac{2i-1}{2}\Delta x}^{\frac{2i+1}{2}\Delta x} P(x)\, \mathrm{d}x, \tag{B.6}$$

and the corresponding linear system is solved in order to derive an explicit expression for the coefficients $\{a_n\}$ of the interpolating polynomial. Thus, assuming that the parent cell is split into two children cells, the fine data is obtained by solving the following integrals:

$$\tilde{y}_m = \frac{1}{\Delta x} \int_{-\frac{\Delta x}{4}}^{0} P(x)\, \mathrm{d}x, \tag{B.7}$$

$$\tilde{y}_p = \frac{1}{\Delta x} \int_{0}^{+\frac{\Delta x}{4}} P(x)\, \mathrm{d}x, \tag{B.8}$$

where $\tilde{y}_m$ and $\tilde{y}_p$ denote the left and right childern cells respectively.

For a fourth-order polynomial, the solution of the linear system reads:

$$a = \frac{1}{(\Delta x)^4}\left[\frac{\tilde{y}_{-2} - 4\,\tilde{y}_{-1} + 6\,\tilde{y}_0 - 4\,\tilde{y}_{+1} + \tilde{y}_{+2}}{24}\right], \tag{B.9}$$

$$b = \frac{1}{(\Delta x)^3}\left[\frac{-\tilde{y}_{-2} + 2\,\tilde{y}_{-1} - 2\,\tilde{y}_{+1} + \tilde{y}_{+2}}{12}\right], \tag{B.10}$$

$$c = \frac{1}{(\Delta x)^2}\left[\frac{-\tilde{y}_{-2} + 12\,\tilde{y}_{-1} - 22\,\tilde{y}_0 + 12\,\tilde{y}_{+1} - \tilde{y}_{+2}}{16}\right], \tag{B.11}$$

$$d = \frac{1}{(\Delta x)}\left[\frac{5\,\tilde{y}_{-2} - 34\,\tilde{y}_{-1} + 34\,\tilde{y}_{+1} - 5\,\tilde{y}_{+2}}{48}\right], \tag{B.12}$$

$$e = \frac{9\,\tilde{y}_{-2} - 116\,\tilde{y}_{-1} + 2134\,\tilde{y}_0 - 116\,\tilde{y}_{+1} + 9\,\tilde{y}_{+2}}{1920}. \tag{B.13}$$

Thus, the corresponding interpolation formulas are:

$$y_m = \tilde{y}_0 - \frac{3\,\tilde{y}_{-2} - 22\,\tilde{y}_{-1} + 22\,\tilde{y}_{+1} - 3\,\tilde{y}_{+2}}{128}, \tag{B.14}$$

$$y_p = \tilde{y}_0 + \frac{3\,\tilde{y}_{-2} - 22\,\tilde{y}_{-1} + 22\,\tilde{y}_{+1} - 3\,\tilde{y}_{+2}}{128}. \tag{B.15}$$

It is trivial to check the arithmetic average of y over the children cells corresponds exactly to the value stored in the parent cell.

Appendix C: Soliton solutions

Self-gravitating bosonic fields can support stable and localised field configurations, where the density profile is static. Such configurations, called solitons, are ubiquitous in models of axion dark matter and exist for dim > 1. Starting with the Schrödinger-Poisson system (in code units):

$$i\frac{\partial \psi}{\partial t} = -\frac{1}{2m}\nabla^2\psi + mV, \tag{C.1}$$

$$\nabla^2 V = \kappa|\psi|^2, \tag{C.2}$$

we take the spherically symmetric ansatz:

$$\psi(r,t) = \chi(r)e^{-2\pi i \frac{t}{T}}. \tag{C.3}$$

The ODE describing the static configuration of the field can be derived by replacing Eq. (C.3) into the Schrödinger-Poisson system:

$$\nabla^2\left[\frac{\nabla^2\chi}{\chi}\right] = 2\kappa m^2\chi^2, \tag{C.4}$$

where the laplacian is now expressed in polar coordinates:

$$\nabla^2 = \frac{d^2}{dr^2} + \frac{2}{r}\frac{d}{dr},$$

and κ represents a free parameter (in our code units κ equals $\frac{3}{2}\Omega_m a$ for a cosmological simulation with axion-like dark matter). Thus, the system can be solved by considering the initial conditions:

$$\chi(0) = 1,$$
$$\chi'(0) = 0,$$
$$\chi'''(0) = 0,$$

where $\chi''(0)$ is a free parameter, which is set by requiring asymptotic vanishing solution $\chi(\pm\infty) = 0$. The oscillation period T can then be computed from the resulting solution, for more details see Schive et al. (2014) and Marsh & Pop (2015).

The soliton profile, normalised such that the total mass is unity, is given by:

$$\chi(r) = \frac{32}{\sqrt{33 r_{\rm core}^3 \pi}} \frac{1}{\left[1 + (r/r_{\rm core})^2\right]^4}, \tag{C.5}$$

where r is the distance from the center of the box and:

$$m = \sqrt{\frac{33}{r_{\rm core}\kappa}} \frac{32}{\alpha^2}, \quad T = \sqrt{\frac{33 r_{\rm core}^3}{\kappa}} \frac{\pi^2}{16\gamma^2}, \tag{C.6}$$

with $\alpha = 0.230$ and $\gamma = -0.692$. In our tests, even if this derivation assumes an infinite box, we use either fixed or periodic boundary conditions. As long as the core radius of the soliton is small enough compared to the simulation box, this solution represents a good approximation.